

# IRRADIATION INDUCED EFFECTS ON 6H-SiC

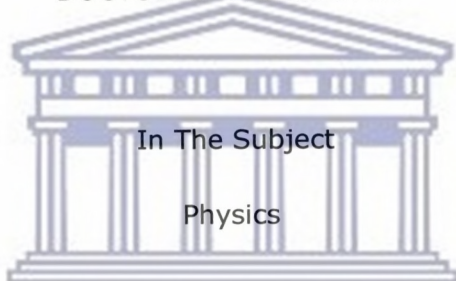
by

**PRAISE SIBUYI**

Dissertation Submitted In Part Fulfilment Of The Requirements

For The Degree Of

DOCTOR OF PHILOSOPHY



In The Subject

Physics

UNIVERSITY *of the*  
At The  
WESTERN CAPE  
UNIVERSITY OF WESTERN CAPE

SUPERVISOR:

Prof M. Maaza (iThemba LABS)

CO-SUPERVISORS:

Prof. R. Madjoe (UWC)

Dr B. D. Ngom (Nanoafnet-iThemba LABS)

**November 2012**



UNIVERSITY *of the*  
WESTERN CAPE

**UNIVERSITEIT VAN WES-KAAPLAND  
BIBLIOTEK**

**LIBRARY  
UNIVERSITY OF THE WESTERN CAPE**



UNIVERSITY *of the*  
WESTERN CAPE

I **PRAISE SIBUYI** declare that this is my work. It is being submitted in part fulfilment of the requirement for the degree of Doctor of Philosophy at the University of Western Cape. It has not been submitted before for any degree or examination, at any other university.

Signature: .....

Date: .....

## ACKNOWLEDGEMENTS

First of all I would like to thank God for everything in my life including, the serenity and commitment to finish this work. Several people have assisted me in getting this Ph.D work done. I would like to express my deep gratitude to Professor M. Maaza and Professor R. Madjoe, for their enduring guidance, enthusiastic encouragement and expedient critiques of this research work. I am indeed thankful to them again for agreeing to supervise this research work to completion.

I would like to express my very countless appreciation to Dr. Balla Diop Ngom for his valuable and constructive submissions during this research work. His willingness to give his time so generously has been very much appreciated, for giving extra attention to this work, organizing and scientific contribution to the entire work. I am indeed very grateful to you.

I wish to thank my Ph.D fellows: Mr. Joseph Sithole, Mr. Saleh Khalimlich, Jean Bosco Kana Kana, Miss Mpho Mokgale, Mr. Lebogang Kotsedi, Miss Nametso Mongwaketsi, Mr. Chris Mtshali, and Mr. Cebo Ndlangamandla for the great ideas we shared through out the years, may the spirit continue. I wish again to extend my word of thanks to Lusanda Nyusani for her will to always assist all of us with all our administrative requests. Thank you!!!

My sincere thanks to all the technical support I received from all my colleagues at iThemba LABS, Material Research Department, NRF.  
A special thanks is extended to the following colleagues:

Mr. Phillip Sechogela for his assistance with the RBS beam line.  
The XRD team, Dr. R. Butcher and Z. Khumalo for the assistance with the XRD facility.  
Dr. M. Nkosi, for his assistance with the AFM imaging facility.  
Dr. R. Nemetudi, the head of MRD, for his continued support, assistance and encouragement.

My sincere thanks to all the staff of iThemba LABS, for the human spirit and warmth, it was indeed a home away from home.

I wish to acknowledge with gratitude the financial support I received throughout this project from SANHARP, Department of Science and technology and iTHEMBA LABS, National Research Foundation. I extend my word of thanks greatly to the staff of SANHARP, Zikhona Lose and Tsibiso Mohlomi for their undying support and forever available for my our financial request, you really made the seafaring smooth.

My grateful thanks are also extended to the director of Centre for Nuclear Reasearch of Dradia (CRND) and COMENA, DR. MESSAOUD.BAALIOUAMER, for giving me an opportunity to perform my experimental work using the Nuclear reactor facility, I wish to send my sincerest thanks to the entire technical team, and everybody, I really enjoyed my stay at Algiers, Algeria.

Lastly, wish to thank my entire family for their support and encouragement of which all contributed in various ways. Without forgetting, a special thanks to those who are nanometers away from my heart, Palesa and two daughters, Mikateko & Ndzalo, for their understanding of my long stays in various parts of the country and outside, my deepest love to you all.

I thank you all.



UNIVERSITY *of the*  
WESTERN CAPE

**I dedicate this thesis to my wife and kids for their undying support and love.**

iii

## ABSTRACT

*The framework agreement in the year 2000 by the international community to launch Generation IV program with 10 nations, to develop safe and reliable nuclear reactors gave rise to the increased interest in the studies of SiC and the effect of different irradiations on solids. Silicon carbide is a preferred candidate used in harsh environments due to its excellent properties such as high chemical stability and strong mechanical strength. The PBMR technology promises to be the safest of all nuclear technology that have been developed before. SiC has been considered one candidate material being used in the fabrication of pebble bed fuel cell. Its outstanding physical and chemical properties even at high temperatures render it a material of choice for the future nuclear industry as whole and PBMR in particular. Due to the hostile environment created during the normal reactor operation, some of these excellent properties are compromised. In order to use this material in such conditions, it should have at least a near perfect crystal lattice to prevent defects that could compromise its strength and performance. A proper knowledge of the behavior of radiation-induced defects in SiC is vital.*

*During irradiation, a disordered crystal lattice occurs, resulting in the production of defects in the lattice. These defects lead to the degradation of these excellent properties of a particular material. This thesis investigates the effects of various radiation effects to 6H-SiC. We have investigated the effects of radiation induced damages to SiC, with a description of the beds and the importance of the stability of the SiC-C interface upon the effects of radiations ( $\gamma$ -rays, hot neutrons). The irradiated samples of 6H-SiC have been studied with various spectroscopic and structural characterization methods. The surface sensitive techniques such as Raman spectroscopy, UV-Vis, Photoluminescence and Atomic Force Microscopy will be employed in several complimentary ways to probe the effect of irradiation on SiC. The obtained results are discussed in details.*

## TABLE OF CONTENT

Acknowledgments	ii
TABLE OF CONTENTS	V
LIST OF TABLES	IX
LIST OF FIGURES	X

---

### **1 INTRODUCTION.....1**

---

<b>1.1. Background</b>	
<b>1.2. South Africa's Primary Energy Supply</b>	
<b>1.3. Pebble Bed Modular Reactor Technology</b>	
<b>1.4. PBMR TRISO Fuel Integrity</b>	
<b>1.5. The Pebble Bed Modular Reactor TRI-ISOTROPIC Fuel Particle</b>	
<b>1.6. Study Motivation</b>	
<b>1.7. Statement Of The Problem</b>	
<b>1.8. Objective Of The Study</b>	
<b>1.9. Outline Of The Thesis</b>	
<b>1.10 References</b>	

---

### **2 SURVEY ON THE TYPES OF NUCLEAR REACTORS AND THEIR RELATED TECHNOLOGY.....17**

---

<b>2.1 Background</b>	
2.1.1 Gas cooled and graphite moderated: Magnox and AGR	
2.1.2 Heavy H <sub>2</sub> O cooled and moderated	
2.1.3 H <sub>2</sub> O cooled and moderated: PWR and BWR	
2.1.4 Water cooled and graphite moderated: RBMK	
<b>2.2 Modern Nuclear Reactor Developments</b>	

- 2.2.1 The Next-Generation CANDU
- 2.2.2 Advanced pressurized H<sub>2</sub>O Reactor AP1000

**2.3 THE PROTOTYPE NUCLEAR REACTOR DESIGNS**

- 2.3.1 International Reactor, Innovative, Secure: IRIS
- 2.3.2 Pebble Bed Modular Reactor: PBMR

**2.4 Fast Nuclear Reactors**

**2.5 Fusion Nuclear Reactors**

**2.6 References:**

**3 LITERATURE SURVEY ON THE PROPERTIES AND SYNTHESIS OF SILICON CARBIDE (SiC).....27**

---

**BACKGROUND OF SiC**

**3.1 PHYSICAL PROPERTIES OF SiC**

- 3.1.1 The crystal structure
- 3.1.2 Thermal properties
- 3.1.3 Thermal expansion
- 3.1.4 Electrical properties

**3.2 Survey on Silicon Carbide Bulk Synthesis**

- 3.2.1 Acheson process
- 3.2.2 Lely process
- 3.2.3 Modified Lely process
- 3.2.4 Chemical Vapor Deposition (CVD)
- 3.2.5 Growth from liquid phase

**3.4 References**





**4 LITERATURE SURVEY ON THE RADIATION INTERACTIONS AND EFFECTS ON SiC.....43**

---

**4.1. INTERACTIONS OF RADIATIONS WITH MATTER**

**4.1.1 Interactions with protons**

- 4.1.1.1 Proton interaction with electrons
- 4.1.1.2 Proton interaction with nuclei: scattering

**4.1.2 Interactions with neutrons**

- 4.1.2.1 Microscopic interactions
  - 4.1.2.1.1 The Cross-Section Concept
  - 4.1.2.1.2 Types of Interactions
- 4.1.2.2 Macroscopic interactions
  - 4.1.2.2.1 Macroscopic cross sections
  - 4.1.2.2.2 Mean Free Path and Reaction Rate
- 4.1.2.3 Effects of moderation in bulk matter
- 4.1.2.4 Effects of multiplication in bulk matter

**4.1.3 Interactions with  $\gamma$ -ray**

- 4.1.3.1 Photoelectric Absorption
- 4.1.3.2 Compton Scattering
- 4.1.3.3 Pair Production
- 4.1.3.4 Interactions with electrons

**4.2 Irradiation effects on SiC**

- 4.2.1 Irradiation with protons**
- 4.2.2 Irradiation with Neutrons**
- 4.2.3 Irradiation with  $\gamma$ -rays**
- 4.2.4 Irradiation with Laser**

**4.3 References:**

**5 CHARACTERIZATION TECHNIQUES.....110**

---

**5.1 X-ray diffraction**

- 5.1.1 Generation of X-ray

<b>5.2</b>	<b>Atomic Force microscopy</b>	
<b>5.3</b>	<b>Raman Spectroscopy</b>	
5.3.1	Introduction	
5.3.2	Origins of Raman	
5.3.3	Instrumentation	
<b>5.4</b>	<b>Photoluminescence</b>	
5.4.1	Radiative recombination mechanisms observed in PL.	
5.4.2	Experimental setup	
5.4.3	Excitation source	
5.4.4	Cryostat	
5.4.5	Microscope Objectives	
5.4.6	Monochromator	
5.4.7	Video camera	
<b>5.5</b>	<b>References</b>	
<b>6</b>	<b>RESULTS AND DISCUSSIONS</b>	<b>132</b>
<b>6.1</b>	<b>Samples</b>	
<b>6.2</b>	<b>Irradiation</b>	
<b>6.2.1</b>	<b><i>Reactor neutrons irradiation</i></b>	
<b>6.2.2</b>	<b><i>γ-rays irradiation</i></b>	
<b>6.2.3</b>	<b><i>Protons irradiation</i></b>	
<b>6.3</b>	<b>RESULTS AND DISCUSSIONS</b>	
<b>6.3.1</b>	<b><i>Effect of Neutrons and γ-rays irradiation</i></b>	
6.3.1.1	Raman spectroscopy	
6.3.1.2	Morphological properties	
6.3.1.3	Optical properties: Photoluminescence data analysis	
<b>6.3.2</b>	<b><i>Effect of Protons irradiation</i></b>	
6.3.2.1	Raman Spectroscopy	
6.3.2.2	Atomic Force Microscopy	
<b>6.4</b>	<b>References:</b>	
<b>7</b>	<b>SUMMARY AND CONCLUSION</b>	<b>169</b>



## LISTES OF TABLES

<b>Table 1.1:</b>	Properties of SiC [7].....	<b>12</b>
<b>Table 3.1:</b>	Bandgap of different polytypes of SiC [10].....	<b>31</b>
<b>Table 3.2:</b>	Lattice parameters and density of SiC polytypes at room temperature [14].....	<b>32</b>
<b>Table 3.3:</b>	Summary of physical properties of some SiC polytypes [15-16].....	<b>34</b>
<b>Table 4.1:</b>	Average number of collisions required to reduce a neutron's energy from 2 MeV to 0.025 eV by elastic scattering [2].....	<b>61</b>
<b>Table 4.2:</b>	Nuclear data for <sup>nat</sup> UO <sub>2</sub> [17].....	<b>71</b>
<b>Table 4.3:</b>	Neutron cross sections of common materials.....	<b>75</b>
<b>Table 4.4:</b>	Moderating powers and ratios of selected materials [19].....	<b>78</b>
<b>Table 4.5:</b>	Example of neutron population decline [2].....	<b>81</b>
<b>Table 6.1:</b>	The irradiation experimental details.....	<b>134</b>

## LISTES OF FIGURES

<b>Figure 1.1:</b>	Physical layout of the proposed PBMR main power system.....	<b>7</b>
<b>Figure 1.2:</b>	Fuel element design for PBMR.....	<b>10</b>
<b>Figure 3.1:</b>	The tetragonal bonding of carbon atom with four nearest silicon neighbours. The distances a and C-Si are approximately 3.08 Å and 1.89 Å respectively.....	<b>29</b>
<b>Figure 3.2:</b>	The stacking sequence of double layers of the three most common SiC polytypes. ....	<b>30</b>
<b>Figure 4.1:</b>	Number of $\delta$ -electrons produced per incident proton per cm H <sub>2</sub> O calculated using equation (4.7) [1].....	<b>48</b>
<b>Figure 4.2:</b>	Solid line (scale on right axis): ratio between total elastic cross section of 180 MeV protons incident on <sup>16</sup> O (using DWUCK4) and Coulomb contribution (using equation (4.9) ) as a function of deflection angle. Dotted line: ratio=1. Dashed line (scale on left axis): Coulomb contribution [1].....	<b>50</b>
<b>Figure 4.3:</b>	Total nonelastic nuclear cross section for protons incident on <sup>16</sup> O. The line represents a fit using the GNASH- code [15] to the experimental data [1].....	<b>54</b>
<b>Figure 4.4:</b>	Proton flux reduction due to inelastic nuclear reactions for a 80 and a 180 MeV beam in a water medium calculated using equation (4.13) and the cross sections in figure 4.3 [1].....	<b>55</b>
<b>Figure 4.5:</b>	various categories of neutron interactions. The letters separated by commas in the parentheses show the incoming and outgoing particles [2].....	<b>59</b>
<b>Figure 4.5:</b>	Total neutron cross section of <sup>239</sup> Pu [2].....	<b>64</b>

<b>Figure 4.6:</b>	Low-energy total neutron cross section of boron [16].....	<b>65</b>
<b>Figure 4.7:</b>	Low-energy total neutron cross section of cadmium [16].....	<b>66</b>
<b>Figure 4.8:</b>	Fission cross sections for some important fissile ( $^{235}\text{U}$ , $^{239}\text{Pu}$ ) And fertile ( $^{238}\text{U}$ , $^{240}\text{Pu}$ ) isotopes [16].....	<b>67</b>
<b>Figure 4.9:</b>	The intensity of a parallel beam of uncollided neutrons decreases exponentially as it passes through a thick layer of matter [2].....	<b>70</b>
<b>Figure 4.10:</b>	Neutrons with 1 MeV of kinetic energy are shown Entering cylinders of material from the bottom and then being scattering or absorbed. The paths were calculated using a Monte Carlo technique.....	<b>73</b>
<b>Figure 4.11:</b>	The multiplication M is shown as a function of the multiplication factor $K_{\text{eff}}$ . Only subcritical values ( $K_{\text{eff}}$ less than one) are included here [2].....	<b>82</b>
<b>Figure 4.12:</b>	A representation of the photoelectric absorption process. ....	<b>85</b>
<b>Figure 4.13:</b>	Photoelectric mass attenuation coefficient of lead [3].....	<b>86</b>
<b>Figure 4.14:</b>	A schematic representation of Compton scattering.....	<b>87</b>
<b>Figure 4.15:</b>	Energy of Compton-scattered electrons as a function of scattering angle and incident gamma-ray energy ( $E_{\gamma}$ ). The sharp discontinuity corresponds to the maximum energy that can be transferred in a single scattering [3].....	<b>89</b>
<b>Figure 4.16:</b>	High-resolution spectrum of $^{137}\text{Cs}$ showing full-energy photo peak, Compton edge, and backscatter peak from the 662 keV gamma ray. Events below the photo peak are caused by Compton scattering in the detector and surrounding materials [3]. ....	<b>91</b>

<b>Figure 4.17:</b> Energy of the Compton edge versus the energy of the incident gamma ray [3].....	<b>92</b>
<b>Figure 4.18:</b> A schematic representation of pair production.....	<b>94</b>
<b>Figure 4.19:</b> Gamma-ray spectrum of the fission-product <sup>144</sup> Pr showing single-escape (SE) and double-escape (DE) peaks (1674 and 1163) that arise from pair-production interactions of 2186 keV gamma rays in a germanium detector [3].....	<b>94</b>
<b>Figure 4.20:</b> gives a schematic picture of a simple binary elastic collision.....	<b>97</b>
<b>Figure 4.21:</b> Schematic representations of positions of the energy levels for silicon vacancies in the SiC band gap. DL stand for donor level and AL stands for acceptor level.....	<b>97</b>
<b>Figure 5.1:</b> Bragg's law.....	<b>111</b>
<b>Figure 5.2:</b> XRD facility at iThemba LABS used for the crystallographic study of the samples.....	<b>115</b>
<b>Figure 5.3:</b> Scheme of generation of X-rays.....	<b>116</b>
<b>Figure 5.4:</b> Schematic diagram of the major components of the AFM showing the feedback loop for Tapping Mode operation.....	<b>119</b>
<b>Figure 5.5:</b> AFM unit at iThemba LABS used for the imaging of the surface morphology and roughness of the samples.....	<b>120</b>
<b>Figure 5.6:</b> Raman virtual states.....	<b>123</b>
<b>Figure 5.7:</b> Electronic energy levels and transitions.....	<b>127</b>
<b>Figure 5.8:</b> Electronic orbitals and transitions.....	<b>128</b>

<b>Figure 5.9:</b> Schematic illustration of common recombination processes.....	<b>129</b>
<b>Figure 6.1.a:</b> XRD patterns in BB configuration of the non-irradiated samples of 6H-SiC.....	<b>137</b>
<b>Figure 6.1b:</b> (0012) XRD pattern in BB configuration evolution with the neutrons irradiation dose.....	<b>138</b>
<b>Figure 6.1c:</b> peak position for irradiated and non-irradiated samples of SiC.....	<b>139</b>
<b>Figure 6.2a:</b> Raman spectra from 750 $\text{cm}^{-1}$ to 1200 $\text{cm}^{-1}$ for irradiated and non-irradiated samples.....	<b>141</b>
<b>Figure 6.2b:</b> Raman spectra from 750 $\text{cm}^{-1}$ to 820 $\text{cm}^{-1}$ and non-irradiated samples.....	<b>142</b>
<b>Figure 6.2c:</b> The relative Intensity (RI) of the Folded irradiated Transversal Optical (FTO) mode versus irradiation dose.....	<b>142</b>
<b>Figure 6.2d:</b> Ram peak position for the Folded Transversal Optical (FTO) mode versus irradiation dose on 6h- SiC.....	<b>143</b>
<b>Figure 6.2e:</b> Raman spectra from 100 $\text{cm}^{-1}$ to 2200 $\text{cm}^{-1}$ for irradiated and non-irradiated samples of SiC.....	<b>146</b>
<b>Figure 6.2f:</b> Raman spectra from 750 $\text{cm}^{-1}$ to 820 $\text{cm}^{-1}$ for irradiated and non-irradiated samples of SiC.....	<b>146</b>
<b>Figure 6.2g:</b> The peak position of the Folded Transversal Optical (FTO) mode versus irradiation dose.....	<b>147</b>
<b>Figure 6.2h:</b> The relative Intensity (RI) of the Folded Transversal Optical (FTO) mode versus irradiation dose. ....	<b>147</b>

<b>Figure 6.3a:</b> AFM micrographs of non-irradiated and fast neutron-irradiated 6H-SiC samples.....	<b>150</b>
<b>Figure 6.3b:</b> Plot of the AFM surface roughness versus neutron dose.....	<b>151</b>
<b>Figure 6.3c:</b> AFM micrographs as a function of thermal gamma fluence.....	<b>152</b>
<b>Figure 6.3d:</b> AFM surface roughness as a function of the thermal gamma fluence. ....	<b>153</b>
<b>Figure 6.4a:</b> Room temperature PL of the non-irradiated sample of 6H-SiC with a Lorentzian fitting.....	<b>155</b>
<b>Figure 6.4b:</b> Room temperature PL of neutron irradiated samples of 6H-SiC.....	<b>156</b>
<b>Figure 6.4b:</b> Room temperature PL of $\gamma$ -ray irradiated samples of 6H-SiC.....	<b>157</b>
<b>Figure 6.5a:</b> Raman spectra from $100\text{ cm}^{-1}$ to $2500\text{ cm}^{-1}$ for protons irradiated and non irradiated samples of SiC.....	<b>161</b>
<b>Figure 6.5b:</b> The peak intensity evolution of the different observed mode versus protons irradiation dose.....	<b>162</b>
<b>Figure 6.6a:</b> AFM micrographs of non-irradiated and protons-irradiated 6H-SiC samples.....	<b>165</b>
<b>Figure 6.6b:</b> AFM surface roughness as a function of protons dose.....	<b>166</b>



# CHAPTER-1

## INTRODUCTION

---

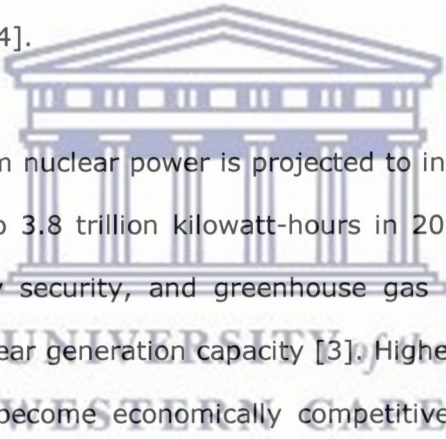
### **1.1. Background**

According to recent statistical review on world energy consumption, the global demand for energy continues to grow. In 2007 alone, global energy consumption grew by 2.4% and predictions are that a further 50% increase can be expected from 2005 to 2030 [1-2]. In 2008, the world primary energy consumption, including oil, natural gas, coal, nuclear and hydropower grew by 1.4%. One factor contributing to energy demand is the world population growth. With both population growth and economic growth comes increased energy demand [1-2].

Based on this energy demands assumptions and predictions, scientist around the world are working on the clock to find new technologies to generate energy other than usage of coal. Petroleum is the world's number one source of energy, with oil accounting for more than 33% of the total energy consumed. Coal is the second, providing more than 25% of the world's energy, for three consecutive years, coal accounted for the majority of primary energy consumption and the fastest growing fuel consumed resulting in high global CO<sub>2</sub> emissions. This is despite global investment in renewable energy facilities, in 2007; there was a 30% increase in spending on construction of renewable energy facilities, for a total of \$71 billion [3].

Nevertheless, renewable currently provides less than 10% of the world's energy. The high level of CO<sub>2</sub> emissions from coal combustion is a great concern for the environment as it contributes extensively to the crisis of global warming. These emissions should be

halved as quickly as possible to reduce their disruption to the world ecosystem by global climatic change. Nuclear power is an alternative source of CO<sub>2</sub>-free energy generation. If we really are facing a global emergency on the climate front, building new reactors is the best option to get the world through the crisis of the next generation, for example renewable like solar, wind and biomass can help fill the gap, but only nuclear power offers clean, environmentally friendly source of energy on a massive scale. Moreover, compared to the huge atmospheric emissions from fossil-fuel energy, nuclear wastes exist in small, highly manageable amounts that can be stored without harm to people or the environment. A major advantage of radioactive waste from a nuclear power station is that it is so small in volume compared to the equivalent waste from, for example, a coal-fired power station [4].



Electricity generation from nuclear power is projected to increase from about 2.7 trillion kilowatt-hours in 2006 to 3.8 trillion kilowatt-hours in 2030, as concerns about rising fossil fuel prices, energy security, and greenhouse gas emissions support more the development of new nuclear generation capacity [3]. Higher fossil fuel generation prices allow nuclear power to become economically competitive with generation from coal, natural gas, and liquids despite the relatively high capital and maintenance costs associated with nuclear power plants [3].

## **1.2. South Africa's primary energy supply**

South Africa's main energy source has always been coal, which the country has had in abundance. The country also has large reserves of uranium and small reserves of oil and gas. As such, South Africa continues its dependence on coal for the production of electricity. This means that the country's economy is highly dependent on fossil fuels, and South Africa is one of the highest emitters of greenhouse gas per capita in the world [3]. The second biggest energy carrier is imported crude oil, needed for the

supply of liquid fuels for transportation. Moderate amounts of nuclear, gas and hydro also contribute to the energy mix.

The current mix of electricity generation capacity continues to be dominated by coal (91%), with nuclear electricity from Koeberg's two nuclear reactors in the Cape making up an additional 5%. Other smaller stations to meet peak requirements are open cycle gas turbines (0.1%) and pumped storage and hydro stations (2%) [5].

South Africa's Integrated Electricity Resource Plan (IRP) for 2010-2030 outlines the country's electricity demand, how this demand would be supplied, and what it is likely to cost. Its balanced scenario represents the best trade-off between least-investment cost, climate change mitigation, diversity of supply, localization, and regional development. The IRP requires 52 GWe of new capacity by 2030, assuming 3.4 GWe of demand-side savings. According to this scenario, South Africa's generation mix by 2030 should include: 48% coal; 13.4% nuclear; 6.5% hydro, 14.5% other renewable sources; and 11% peaking open cycle gas turbine. At least 9.6 MWe new nuclear capacity is anticipated by 2030 [6].

Within the framework of this research work at the start, the Pebble Bed Reactor Technology is one nuclear reactor technology that was considered by the South African government as a key solution to the South African electricity crisis and contributes to the world vision of reducing CO<sub>2</sub> emissions. Although we acknowledge that the South African government has stopped the building of the demonstration plant in 2010, we had however based our research work and defined the scope based on the technology. Pebble Bed Modular Nuclear Reactor (PBMR) technology is one of the most advanced modern nuclear technologies and promises to be highly competitive with almost all other forms of energy generation. The PBMR technology promised to be the safest of all

nuclear technology that have been developed before. The following section will describe in details the technology itself and its fundamental features.

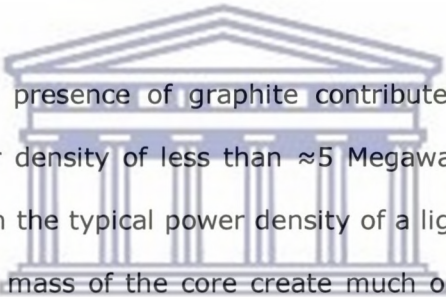
### **1.3. Pebble Bed Modular reactor technology**

ESKOM has been working on the Pebble Bed Modular Reactor project since early 1990's. The pebble-bed concept itself goes back to the 1950's and German helium cooled high temperature reactor pioneer Professor Dr. Rudolf Schulten. In particular he had the idea of a fuel consisting of coated uranium dioxide particles compacted into tennis-ball-sized graphite spheres, the pebbles of the pebble-bed reactor. The particle coatings include silicon carbon and pyrolytic carbon, which are capable of maintaining integrity at very high temperatures.

This concept was first employed, with great success, in the 15 MWe (40 MWth) AVR (Arbeitsgemeinschaft Versuchsreaktor) research reactor at Jülich, which started up in 1966 and shut down in 1988, after the Chernobyl accident. AVR successfully demonstrated many of the inherent safety features being attributed to PBMR. The pebble-bed concept was also employed, at much larger scale than both the AVR and the planned PBMR, in the unfortunate 300 MWe (750 MWth) THTR-300 plant, at Hamm-Uentrop, Germany, which used a concrete rather than steel pressure vessel. This started up in 1985, but also shut down, posts Chernobyl, in 1988 for a variety of political and economical reasons, compounded by technical problems. The technical issues included difficulties with insulating the concrete against the high temperatures and early damage to fuel caused by overly forceful insertion of in-core control rods during initial testing.

The most outstanding feature of the PBMR type of a reactor is that it uses attributes inherent in and natural to the processes of nuclear energy generation to enhance safety features. It is safe, clean, cost-competitive, versatile and adaptable. The reactor core of

a PBMR contains 452,000 pebbles packed in a vessel that is less than 2 meters in internal diameter and 11 meters tall. Seventy five percent are fuel pebbles; the remaining pebbles are pure graphite. Each fuel pebble contains 15,000 micro-spheres of uranium fuel that are fabricated in a unique way. The internal 0.5 mm microsphere is uranium (enriched to 9.6 %  $^{235}\text{U}$ ). This fuel is coated with a dense layer of pyrolytic carbon, a layer of silicon carbide (SiC) and an outer carbon layer. With coatings, each TRISO (Tri-Isotropic layers) sphere is slightly less than 1 mm in diameter. The 15,000 spheres are then mixed in a graphite matrix and pressed and sintered into a pebble about 6 cm in diameter. A single core load requires high quality fabrication of nearly 5 billion microspheres.

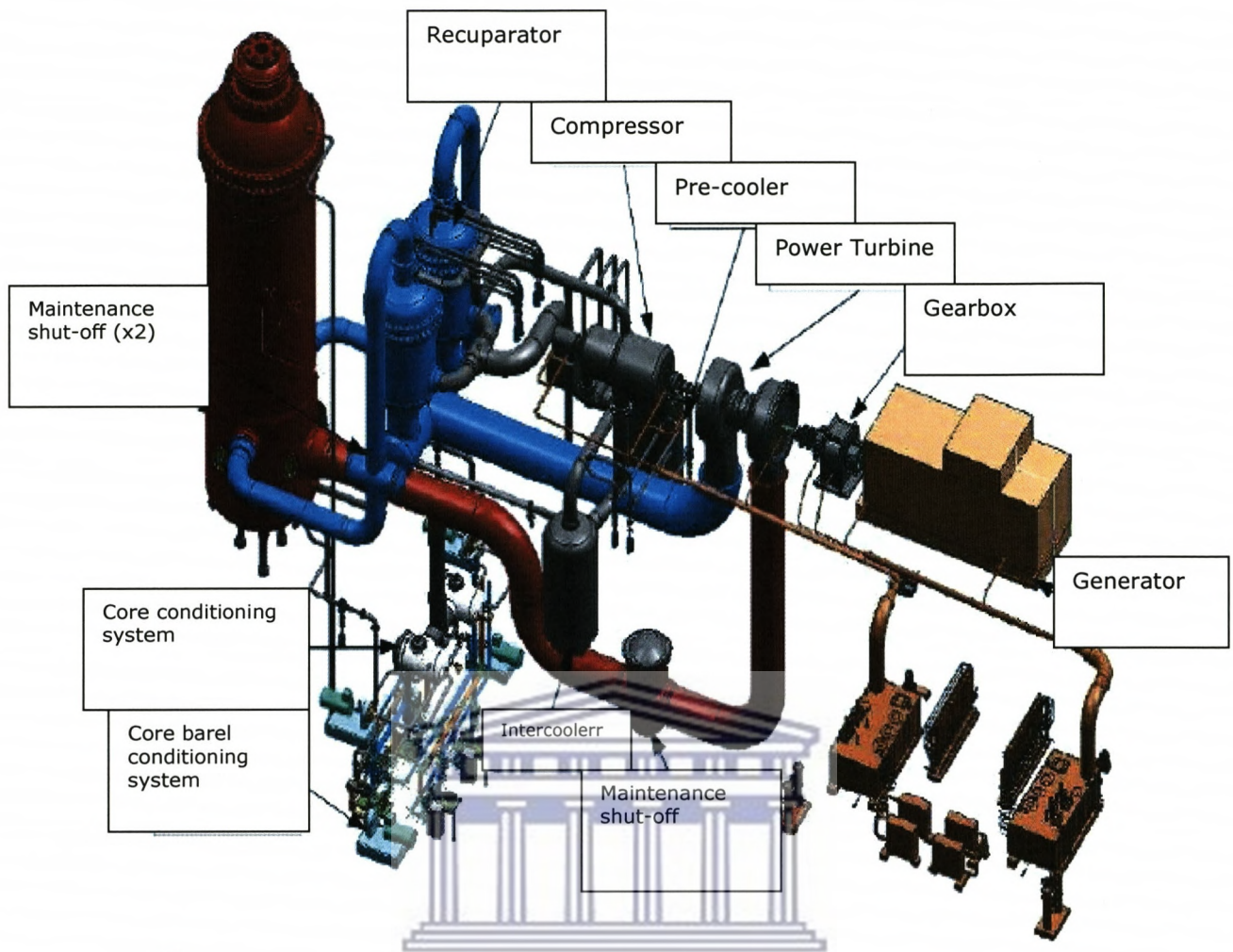


The core geometry and presence of graphite contributes in three ways to inherent safety. It yields a power density of less than  $\approx 5$  Megawatts thermal per cubic meter, about ten times less than the typical power density of a light water reactor. The surface area of the pebbles and mass of the core create much opportunity to dissipate decay heat. With this feature, these forms of heat loss overcome the potential for the core to heat up, and potentially melt down, after a loss of coolant accident. The enduring presence of the moderator also improves safety. In a light water reactor, water is used both to cool the core and to moderate the reaction. When the coolant is lost, the moderator is lost as well. In a gas-graphite reactor, the graphite remains after the possible loss of helium coolant. As the fuel heats, graphite yields a strongly negative coefficient of reactivity, resulting in the slowing down of the fission process.

The PMBR reactor design has a more negative fuel temperature coefficient of reactivity than light Water Reactors (LWRs), as the Doppler feedback is greater for the less-thermal neutron spectrum associated with a graphite moderator which reduces the risk of reactivity accidents for most scenarios, but increases the risk for accidents involving

core overcooling. Pebbles are loaded continuously at top of the core, flow downward, and are discharged at bottom. The removed spheres are measured to determine the level of burn up and integrity, and are either sent to storage or returned to the core. The average sphere will pass through the core about 6 times before being discharged. This process reduces the core inventory of two very troublesome short-lived radionuclides, including xenon-133 which contributes to core instabilities and iodine-131, which is a major contributor to offsite doses in accidents. Helium gas enters the core at 482 °C and leaves the core at 900 °C.

The helium flows directly through a Brayton cycle turbine, which then drives the generator. The direct coupling to a gas turbine without heat exchange to steam would be the first of its kind. Because of the high temperature, direct coupling, and use of a gas turbine, Eskom estimates that the thermal efficiency of the unit would be 43%, significantly better than the 33% efficiency achieved by light water reactors. The helium is cooled through a series of water-cooled heat exchangers. Inherent safety allows the pebble bed to operate without the extensive and expensive active safety systems required in regular reactors. These characteristics, along with high thermal efficiency, high fuel utilization, and modular construction, make the pebble bed an economically modern attractive reactor. The figure 1.1 below shows a PBMR design layout as proposed.



UNIVERSITY of the  
WESTERN CAPE

**Figure 1.1:** Physical layout of the proposed PBMR main power system

#### **1.4. PBMR TRISO fuel integrity**

The safety mechanism for the PBMR places great emphasis on the ability of the fuel pebbles to contain radionuclides under design basis accident conditions. In order to provide assurance that the fuel will perform as expected, several levels of scientific confirmation are required. The fundamental fuel behavior at varying levels of nuclear hostility must be sufficiently well understood so that a complete set of technical specifications for the fuel can be derived. It appears that this is not yet the case.

There are numerous instances in which TRISO microspheres manufactured to identical specifications and irradiated under identical conditions exhibited drastically different fission products release behavior that could not be attributed to observed physical defects like cracking of the SiC layer. This indicates that there are technical factors affecting TRISO performance that have not yet been identified. When a complete set of technical specifications is finally at hand, the PBMR fuel manufacturing process will have to be reliable enough to ensure that the specifications are met. Because PBMR fuel is credited to a greater degree than Light Water Reactor (LWR) fuel for maintaining safety under accident conditions, and is less tolerant than Light Water Reactor fuel to defects, PBMR fuel will have to be subjected to more stringent quality control. However, even if the requirements were no more stringent for PBMR fuel than for Light Water Reactor fuel, inspecting the enormous microsphere flow with a high enough sampling rate to ensure an adequately low defect level is a considerable challenge.

The number of TRISO microspheres manufactured annually to support ten PBMR modules (1150 MWe total) would be on the order of ten billion, three orders of magnitude greater than the number of uranium fuel pellets needed to supply an Light Water Reactors of the same capacity.



Still, if the above two criteria are satisfied, there must be assurance that the behavior of the fuel will not be significantly worse than expected if conditions in the core deviate from predictions.

### **1.5. The Pebble Bed Modular Reactor TRI-ISOTROPIC fuel particle.**

The PBMR fuel particle consists of low enriched uranium tripled-coated isotropic (TRISO) particles contained in a molded graphite sphere.

The coated particle consists of a kernel of uranium dioxide surrounded by four coating layers. The first layer deposited on the kernels is porous carbon. This is followed by an inner layer of dense pyrolytic carbon (IPyC), a layer of Silicon carbide (SiC) and finally the outer layer of pyrolytic carbon as shown in figure 1.2, each of the coated layers has a particular function.

The porous carbon accommodates any mechanical deformation that may arise from the uranium dioxide kernel during the life time of the fuel as well as gaseous fission products diffusing out of the kernel. The inner pyrolytic carbon coating acts as containment to gases during the SiC coating process. The SiC coating layer provides mechanical strength and acts as a barrier to the diffusion of any metallic fission products. The last outer pyrolytic carbon layer coating protects the silicon carbide coating mechanically [3].

15 000 of these coated particles, about a millimeter in diameter, are then mixed with graphite powder and a phenolic resin and pressed into 50 mm diameter spheres.

A 5 mm thick layer of pure carbon is then added to form a 'non-fuel' zone and the resulting spheres are sintered followed by annealing to make them hard and durable. The spherical fuel pebbles are machined to a uniform diameter of 60 mm. Each fuel pebble contains about 9 g of uranium and the total uranium in one fuel load is 4.1 metric tons. The total mass of a fuel is about 210 g [4]. The figure 1.2 below shows a schematic diagram of the pebble fuel element design for the PBMR.

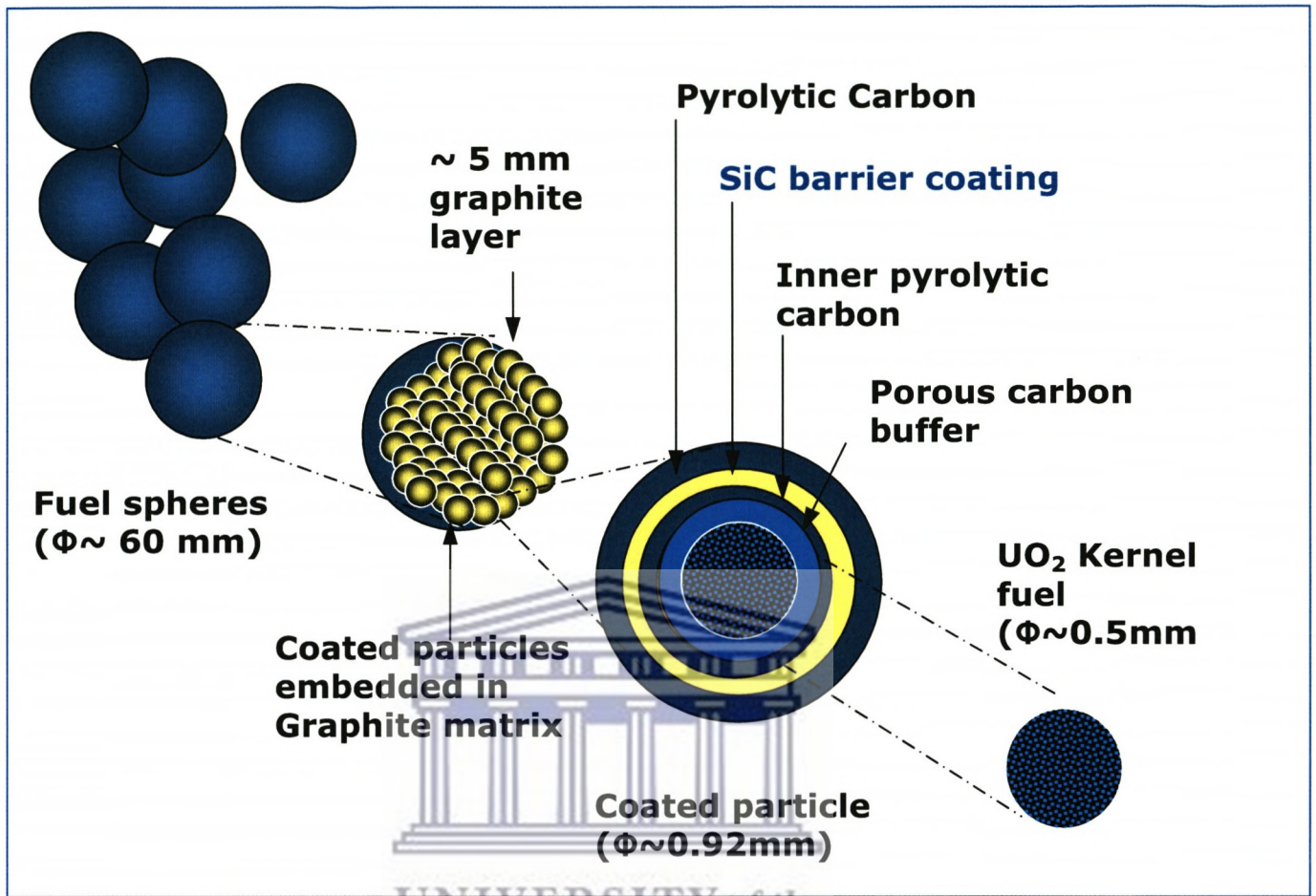


**Figure 1.2:** Fuel element design for PBMR.

## 1.6. Study motivation

The motivation for the study of SiC in this work is due to its superior properties and applications in the nuclear industry. SiC and SiC-based ceramic composites have both superior properties to survive in severe nuclear environments. The discovery of SiC came as a response to technological challenges faced by the Si based devices. In the case of Pebble Bed Modular Reactor design, silicon carbide is used as the primary barrier for the TRISO (Tri-Isotropic) coated fuel as described above. Silicon Carbide has excellent high temperature properties, good corrosion resistance, low neutron absorption cross-section and stability under harsh irradiation environment.

SiC belongs to a class of semiconductors commonly known as wide band gap materials. This class of materials is less sensitive to increased temperatures. Due to these properties, SiC and SiC-based ceramic composites can operate in extremely high temperatures. SiC has a higher thermal conductivity; this means that it dissipates heat quickly. Again, this material is chemically inert which implies that it can survive even in the most acidic environments. It is extremely hard (hardness in Mohs scale  $\approx$  9-10 which compares favorably with values for other hard materials such as diamond  $\approx$  10 and topaz  $\approx$  8), SiC is probably most familiar to people as the grit coating on sandpaper, this hardness again implies that SiC based devices can operate under conditions of extreme pressure. Of importance to our study is the fact that SiC is extremely radiation hard and is used in the coating of pebble. SiC has high electric field strength and high saturation drift velocity. Table 1-1 gives some of the properties of SiC, it is a material with which it is possible to stretch the limits of conventional technology to its extremes.

Due to the hostile environment created in the reactor operation, some of these properties are compromised. The success of the application of this material in nuclear environment is reliant on the integrity of SiC and requires a good knowledge of all the effects of different types of radiation on silicon carbide.

**Table 1-1:** Properties of SiC [7]

Direct Bandgap [eV]	3.03
Breakdown Electric Field [MV/cm] (for 1000 V operation)	$2.4 \times 10^6$
Thermal Conductivity at Room Temperature [W/cm · K]	3.0-3.8 4.9
Saturated Electron Drift Velocity @ $E \geq 2 \times 10^5$ V/cm) [cm/sec]	$2.0 \times 10^7$



**1.7. Statement of the problem**

As outlined above Pebble Bed Modular Reactor (PBMR) technology is designed with a dramatically higher level of safety and efficiency. Instead of water (H<sub>2</sub>O), it uses Pyrolytic graphite as the neutron moderator, and an inert or semi-inert gas such as helium, nitrogen or carbon dioxide as the coolant, at very high temperature, to drive a turbine directly. This eliminates the complex steam management system from the design and increases the transfer efficiency (ratio of electrical output to thermal output) to about 50%. Also, the gases do not dissolve contaminants or absorb neutrons as

water does, so the core has less in the way of radioactive fluids and is more economical than a light water reactor.

PBMR technology uses a TRISO (Tri-Isotropic) type of a micro fuel particle which consists of Fuel kernel  $UO_2$  (sometimes UC or UCO) in the center, coated with four layers of three isotropic materials. The four layers are a porous buffer layer made of carbon, dense inner layer of Pyrolytic Carbon (PyC), ceramic layer of SiC to retain fission products at elevated temperatures and to give the TRISO particle more structural integrity and dense outer layer of PyC.

The three layer system, IPyC-SiC-OPyC, forms the primary barrier to fission product release with SiC being the main pressure boundary for the fuel particle. The evolution of stress in the three layer system during irradiation consists of slow increase in pressure induced stress, due to irradiation behavior of pyrocarbon layers.

The effect of increased temperature and irradiation should be better understood. Studying of irradiation effect in SiC is viewed as essential. Thermal stability is a major parameter of the coated fuels particles and is important from the safety point of view.

The failure mechanism of the coated fuel particle during nuclear reactor operation was previously discussed by Bing et al. [8]. During reactor operation the effect of fuel fission and irradiation damage causes internal pressurization of the fuel as well as an increase in tensile stresses in the pyrocarbon layers. Cracking of the pyrocarbon layers can cause stress concentration at the interface between the pyrocarbon and the SiC. The failure mechanism can be summarized as follows:

- Over-pressurization - fission gases generated from the fuel kernel impose pressure on the layers and induce tensile stresses.

- PyC crack induced failure- stress concentration in the SiC layer created by a through-thickness crack in the IPyC or OPyC. SiC will be failed by high stress concentration.
- Peel-off particle outer coating- Irradiation-induced shrinkage of matrix material, which then imposes tearing stress on the particle outer coating. If the binding between the matrix and PyC coating is strong, the coating may be damaged.
- Kernel-coating interaction. This is called amiba effect, corrosion failure of the SiC layer, caused by high temperature level and oxygen pressure in the PyC layer.
- SiC degradation by fission products and irradiation. Fission products like palladium,  $\text{Ag}^+$  and rare earth elements reach SiC and chemically interact with it, resulting in degradation and failure. It can be chemically attacked by HCL during the SiC deposition.
- SiC decomposition at high temperatures. Thermal decomposition of SiC becomes significant at 2000-2200°C, which leads to increasing porosity of SiC.

Based on this outlined failure mechanisms, it can be clearly seen that more scientific knowledge is still required in order to understand the micro-structural evolution in particular the SiC on the four layers of the pebble fuel and more accurately simulating the behavior of this material under various irradiation sources.

### **1.8. Objective of the study**

The primary objective of this project is to investigate the effects of various radiation types to 6H-SiC. The study will focus more precisely on the effects of irradiation

induced damages to the crystal structure. The considered irradiation types are  $\gamma$ -rays, reactor neutrons and protons. The irradiated samples of 6H-SiC will be studied with various spectroscopic and structural characterization methods. The surface sensitive techniques such as Raman spectroscopy, UV-Vis, Photoluminescence and Atomic Force Microscopy will be employed in several complimentary ways.

We will primarily use Raman spectroscopy, Atomic Force Microscopy and X-Ray diffraction methods to characterize the irradiated samples. Raman spectroscopy has an advantage of providing useful information on the vibration of molecules of SiC-C as a result of irradiation effects. It will enable us to study any slight changes in chemical bonding of molecules as a result of irradiation effects.

While on the other side, X-ray diffraction technique, type D8 will help us track and confirm any phase evolution as a result of radiation damage on the structural integrity of the material SiC. The UV-Vis and photoluminescence will enable us to study the optical properties of the non-irradiated and irradiated samples. A comparison will be drawn from both results, to determine if there exists any noticeable change in the optical band gap of 6H-SiC in the case of UV-Vis.

### 1.9. Outline of the thesis

The content of this thesis will be presented as follows:

**Chapter 2** will give account of the various types of nuclear reactors, giving insight to each type its related technology. This chapter will again as our main focal point, describe the PBMR technology and the usage of SiC as a candidate shielding material in the context of safety.

**Chapter 3** will present the literature survey on the properties and synthesis of various irradiations to Silicon Carbide.

**Chapter 4** will present the literature survey on the interactions and effects of various irradiations to Silicon Carbide.

**Chapter 5** will describe the analytical techniques used in the thesis.

**Chapter 6** will present and discusses the experimental results of the study.

**Chapter 6** will give the summary of the study and conclusions.

### 1.10. References

- [1] International Energy Outlook report (2009).
- [2] Sigma Xi, the Scientific Research Society, Overview of World Energy April 20, (2009).
- [3] British Petroleum Statistical Review Of World Energy June (2009).
- [4] Kadak, A.C. (2005). "A future for nuclear energy: pebble bed reactors, Int. J. Critical Infrastructures, Vol. 1, No. 4, pp.330–345".
- [5] Report: Nuclear Power in South Africa. World Nuclear Association, December (2011).
- [6] South African National Department of Energy: Integrated Resource Plan, March (2010).
- [7] www.cree.com
- [8] Liu Bing, Liang Tongxiang, and Tang Chunhe, Rare Metals, 25 (2006) 337.



## CHAPTER-2

### SURVEY ON THE TYPES OF NUCLEAR REACTORS AND THEIR RELATED TECHNOLOGY

---

#### 2.1 Background

Many different reactor systems have been proposed and some of these have been developed to prototype and to full commercial scale. Six types of reactors namely: Magnox (Magnesium Non Oxidising) reactor type, AGR (Advanced Gas-Cooled Reactor), PWR (Pressurized Water Reactor), BWR (Boiling Water Reactors), CANDU (Canadian Deuterium-Uranium) and RBMK (Reaktor Bolshoy Boshchnosti Kanalniy) have emerged as the designs used to produce commercial electricity around the world. A further reactor type, the so-called fast reactor, has been developed to full-scale demonstration stage. These various reactor types will now be described, together with current developments and some prototype designs, namely the International Reactor, Innovative Secure (IRS) and Pebble Bed Modular Reactor (PBMR). This chapter discusses in details each type of nuclear reactor with its related technology.

#### 2.1.1 Gas cooled and graphite moderated: Magnox and AGR

Magnox and AGR are graphite moderated and gas-cooled nuclear reactors. These types of reactors are the early reactor designs built in the United Kingdom from 1956 to 1971. The Magnox reactor is named after the magnesium alloy used to encase the fuel, which is natural uranium metal. Fuel elements consisting of fuel rods encased in Magnox cans are loaded into vertical channels in a core constructed of graphite blocks. Further vertical channels contain control rods (strong neutron absorbers) which can be inserted or withdrawn from the core to adjust the rate of the fission process and, therefore, the heat output. The whole assembly is cooled by blowing carbon dioxide gas past the fuel cans, which are specially designed to enhance heat transfer. The hot gas then converts

water to steam in a steam generator. Early designs used a steel pressure vessel, which was surrounded by a thick concrete radiation shield. In later designs, a dual-purpose concrete pressure vessel and radiation shield was used [1].

In order to improve the cost effectiveness of this type of reactor, it was necessary to go to higher temperatures to achieve higher thermal efficiencies and higher power densities to reduce capital costs. This entailed increases in cooling gas pressure and changing from Magnox to stainless steel cladding and from uranium metal to uranium dioxide fuel. This in turn led to the need for an increase in the proportion of  $^{235}\text{U}$  in the fuel. The resulting design, known as the AGR still uses graphite as the moderator and as in the later Magnox designs, the steam generators and gas circulators are placed within a combined concrete pressure-vessel or radiation-shield.

### **2.1.2 Heavy H<sub>2</sub>O cooled and moderated**

CANDU was designed in Canada and is the only design of heavy water moderated reactor. In the CANDU reactor, un-enriched uranium dioxide is held in zirconium alloy cans loaded into horizontal zirconium alloy tubes. The fuel is cooled by pumping heavy H<sub>2</sub>O through the tubes (under high pressure to prevent boiling) and then to a steam generator to raise steam from ordinary water (also known as natural or light H<sub>2</sub>O) in the normal way. The necessary additional moderation is achieved by immersing the zirconium alloy tubes in an unpressurised container (called a callandria) containing more heavy H<sub>2</sub>O. Control is affected by inserting or withdrawing cadmium rods from the callandria. The whole assembly is contained inside the concrete shield and containment vessels [2-3].

### **2.1.3 H<sub>2</sub>O cooled and moderated: PWR and BWR**

By moving to greater levels of enrichment of <sup>235</sup>U, it is possible to tolerate a greater level of neutron absorption in the core (that is, absorption by non-fissile, non-fertile materials) and thus use ordinary H<sub>2</sub>O as both a moderator and a coolant. The two commercial reactor types based on this principle of H<sub>2</sub>O as a moderator and coolant are both American designs, but are widely used in over 20 countries. The most widely used reactor type in the world is the Pressurized Water Reactor (PWR) which uses enriched (about 3.2% <sup>235</sup>U) uranium dioxide as a fuel in zirconium alloy cans. The fuel, which is arranged in arrays of fuel "pins" and combined with the movable control rods, is held in a steel vessel through which H<sub>2</sub>O at high pressure (to suppress boiling) is pumped to act as both a coolant and a moderator. The high-pressure water is then passed through a steam generator, which raises steam in the usual way. As in the CANDU design, the whole assembly is contained inside the concrete shield and containment vessel. The second type of water cooled and moderated reactor does away with the steam generator and, by allowing the water within the reactor circuit to boil, it raises steam directly for electrical power generation. This, however, leads to some radioactive contamination of the steam circuit and turbine, which then requires shielding of these components in addition to that surrounding the reactor. Such reactors, known as Boiling Water Reactors (BWRs), are in use in some ten countries throughout the world [4-6].

### **2.1.4 Water cooled and graphite moderated: RBMK**

The design known as the RBMK (Reaktor Bolshoy Boshchnosti Kanalniy) reactor has been developed and many reactors of this type have been constructed in the USSR (Union of Socialist Soviet Republic), including the unfortunate Chernobyl plant. The layout consists of a large graphite core containing some 1700 vertical channels, each containing enriched uranium dioxide fuel (1.8% <sup>235</sup>U). Heat is removed from the fuel by pumping water under pressure up through the channels where it is allowed to boil, to

steam drums, thence driving electrical turbo-generators. Many of the major components, including pumps and steam drums, are located within a concrete shield to protect operators against the radioactivity of the steam.

## **2.2 Modern Nuclear Reactor Developments**

### **2.2.1 The Next-Generation CANDU**

The next generation Canadian Deuterium Uranium reactor (CANDU) is based on the standard proven CANDU design but it introduces new features which include:

- Light water reactor coolant system instead of heavy water.
- Use of slightly enriched Uranium Oxide fuel in bundles rather than natural Uranium fuel.
- Compact reactor core design: core size is reduced by half for same power output.
- Extended fuel life with reduced volume of irradiated fuel.
- Improved thermal efficiency through higher steam pressure steam turbines.

The next generation CANDU reactor retains the standard CANDU reactor features of on-power fuelling, simple fuel design and flexible fuel cycles. The steam and turbine generator systems are similar to those in advanced pressurized water reactor systems. For safety, generation CANDU reactor design includes two totally independent safety shutdown systems and an inherent passive emergency fuel cooling capability in which the moderator absorbs excess heat. The whole of the primary system and the steam generators are housed in a robust containment to withstand all internal and external events [7-8].

### **2.2.2 Advanced pressurized H<sub>2</sub>O Reactor AP1000**

The Westinghouse Company, which is owned by British Nuclear Fuel Limited (BNFL), has developed an Advanced PWR with predominantly passive safety systems. Termed the

AP600 (600MWe), it is the most up-to-date design licensed in the United States. BNFL have also developed the AP1000 (1000MWe) with similar safety features to the smaller version but gaining in economies of scale.

Key design features of the AP designs are:

- Simplification of standard Pressurized Water Reactor designs with less piping, fewer valves, less control cabling and reduced seismic building volumes.
- Modular manufacturing techniques giving a shorter construction schedule, it was estimated that for the AP600 plant 36 months from first concrete to fuel loading.
- Passive safety systems using only natural forces such as gravity, natural circulation and compressed gas. Fans, pumps, diesels and chillers are not required for safety, nor are operator intervention. A few simple valves are used to align the passive safety systems when required, in most instances the valves are 'fail safe' in that on loss of power they move to the safety position.
- The passive cooling systems include core cooling, providing residual heat removal, reactor coolant make-up and safety-injection, and containment cooling which provides the safety related ultimate heat sink for the plant.
- Estimated operating lifetime of 60 years with a design plant availability of 90%+ [9-10].

## **2.3 THE PROTOTYPE NUCLEAR REACTOR DESIGNS**

### **2.3.1 International Reactor, Innovative, Secure: IRIS**

International Reactor Innovative and Secure (IRIS) is an advanced, modular, medium-size (335 MWe) LWR reactor with integral primary circuit configuration. It is being developed by an international team of about 20 organizations from 10 countries, targeting near-term deployment, in the next decade. IRIS characteristics are especially tailored for smaller countries. This is based on a small LWR concept with secure safety

aspects built in. The design will be modular and flexible and achieve economic competitiveness.

### **2.3.2 Pebble Bed Modular Reactor: PBMR**

This cutting nuclear reactor technology as described in chapter 1 is the motivation for this research work. It is a helium-cooled graphite moderated unit of 100MWe which drives a gas turbine linked to a generator giving up to 50% efficiency. Key design features:

- Fuel elements are spherical 'pebbles' 60mm in diameter of graphite containing tiny spheres of Uranium Dioxide coated with carbon and silicon carbide. This coating retains the gaseous and volatile fission products generated in operation.
- The reactor consists of a vertical steel pressure vessel, 6m in diameter and about 20m high. It is lined with graphite bricks drilled with vertical holes to house the control rods.
- Helium is used as the coolant and transfers heat to a closed cycle gas turbine and generator.
- When fully loaded, the core contains 450,000 fuel spheres; re-fuelling is done on-line with irradiated spheres being withdrawn at the base of the reactor and fresh fuel elements being added at the top.
- The PBMR has inherent passive safety features that require no operator intervention.

Removal of decay heat is achieved by radiation, conduction and convection. The combination of very low power density of the core and temperature resistance of the fuel in millions of independent particles underpins the safety assurance of the design.

The PBMR design takes forward the approach originally developed in Germany (AVR 15MW experimental pebble bed reactor and Thorium High-Temperature Reactor (THTR)

300MWe) and is being developed by Eskom, the South African electrical utility, for application in South Africa initially through a demonstration plant.

#### **2.4 FAST NUCLEAR REACTORS**

All of today's commercially successful reactor systems are "thermal" reactors, using slow or thermal neutrons to maintain the fission chain reaction in the  $^{238}\text{U}$  fuel. Even with the enrichment levels used in the fuel for such reactors, however, by far the largest numbers of atoms present are  $^{238}\text{U}$ , which are not fissile [11].

Consequently, when these atoms absorb an extra neutron, their nuclei do not split but are converted into another element, Plutonium. Plutonium is fissile and some of it is consumed in situ, while some remains in the spent fuel together with unused  $^{238}\text{U}$ . These fissile components can be separated from the fission product wastes and recycled to reduce the consumption of uranium in thermal reactors by up to 40%, although clearly thermal reactors still require a substantial net feed of natural uranium.

It is possible, however, to design a reactor which overall produces more fissile material in the form of Plutonium than it consumes. This is the fast reactor in which the neutrons are un-moderated, hence the term "fast". The physics of this type of reactor dictates a core with a high fissile concentration, typically around 20%, and made of Plutonium. In order to make it breed, the active core is surrounded by material (largely  $^{238}\text{U}$ ) left over from the thermal reactor enrichment process. This material is referred to as fertile, because it converts to fissile material when irradiated during operation of the reactor.

Due to the absence of a moderator, and the high fissile content of the core, heat removal requires the use of a high conductivity coolant, such as liquid sodium. Sodium circulated through the core heats a secondary loop of sodium coolant, which then heats water in a steam generator to raise steam. Otherwise, design practice follows established lines, with fuel assemblies clad in cans and arranged together in the core, interspersed with movable control rods. The core is either immersed in a pool of

coolant, or coolant is pumped through the core and thence to a heat exchanger. The reactor is largely unpressurised since sodium does not boil at the temperatures experienced, and is contained within steel and concrete shields.

The successful development of fast reactors has considerable appeal in principle. This is because they have the potential to increase the energy available from a given quantity of uranium by a factor of fifty or more, and can utilize the existing stocks of depleted uranium, which would otherwise have no value. Fast reactors, however, are still currently at the prototype or demonstration stage. They would be more expensive to build than other types of nuclear power station and will therefore become commercial only if uranium or other energy prices substantially increase.

## **2.5 Fusion nuclear reactors**

All the reactors outlined above are fission reactors. Energy can also be produced by fusing together the nuclei of light elements. This is the process which provides the energy source in the sun and other stars. The idea of releasing large amounts of energy by the controlled fusion of the nuclei of atoms such as deuterium and tritium is very attractive because deuterium occurs naturally in seawater.

Unfortunately, controlled fusion has turned out to be an extraordinarily difficult process to achieve. For the reaction to proceed temperatures in excess of one hundred million degrees must be obtained and high densities of deuterium and tritium must be achieved and retained for a sufficient length of time.

So far, it has not proved possible to sustain these requirements simultaneously in a controlled way. A large number of major projects, including a European collaboration which has built the Joint European Torus (JET) at Culham in Oxfordshire, have gradually got closer to reaching the combination of temperature, density and containment time required for success. Even if this can be achieved eventually, the process must be



capable of being developed in a form which will allow power to be generated cost effectively and continuously over a long period. It is very unlikely that this could be achieved until well into the twenty-first century.

## 2.6 References:

- [1] The Magnox Story. Springfields Fuels Limited. July 2008. Retrieved 2010-03-21B.
- [2] Rouben, "Basic CANDU Design", University Network for Excellence in Nuclear Engineering, 2005
- [3] S H Wearne and R H Bird (2009, updated February 2010). UK Experience of Consortia Engineering for Nuclear Power Stations (Report). School of Mechanical, Aerospace & Civil Engineering, University of Manchester. Retrieved 19 September 2010.
- [4] Mosey 1990, pp.69-71
- [5] (<http://www.iaea.org>): "50 Years of Nuclear Energy". IAEA. Retrieved 2008-12-29.
- [6] Technical details and features of Advanced BWRs at the Wayback Machine (archived June 16, 2008) (<http://web.archive.org/web/20080616103454/http://www.nuc.berkeley.edu/designs/abwr/abwr.html>).
- [7] The Need for Nuclear Power. Viewpoint on the World's Challenging Energy Future, R. Rhodes and D. Beller, IAEA Bulletin, Vol. 42, No. 2, 2000 (International Atomic Energy Agency).
- [8] Success in the Changing Electricity Market-What will it take? R.B. Duffey, D.F. Torgerson. W.T. Hancox, and K.R. Hedges, Pacific Basin Nuclear Conference, Seoul, Korea, 29 October - November 02, 2000.
- [9] M.C. Edlund "High Conversion. Ratio Plutonium . Precycle . in Pressurized Water Reactors", Annals of Nuclear Energy, Vol. 2, pp. 801 to 807, Pergamon Press 1975
- [10] H.-H. Hennies, H. Mark1 "Überlegungen zur Modifizierbarkeit eines LWR im Hinblick auf eine bessere Uranausnutzung", Proc. Jahrestagung Kerntechnik '80, pp. 953-956, Berlin, March 1980

- [11] Fast Reactor Knowledge Preservation System: Taxonomy and Basic Requirements".  
[[http://www.pub.iaea.org/MTCD/publications/PDF/Pub1320\\_web.pdf](http://www.pub.iaea.org/MTCD/publications/PDF/Pub1320_web.pdf)]
- [12] Hans A. Bethe, "The Hydrogen Bomb", Bulletin of the Atomic Scientists, April 1950, page 99. Fetched from [books.google.com](http://books.google.com) on 18 April 2011.



## CHAPTER-3

### LITERATURE SURVEY ON THE PROPERTIES AND SYNTHESIS OF Silicon Carbide (SiC)

---

#### BACKGROUND OF SiC.

Silicon carbide was first observed in 1824 by the Swedish scientist, Jöns Jacob Berzelius [1] while he was attempting to synthesize diamond, while the naturally occurring SiC has been discovered by Henri Moissan in 1905, who found small hexagonal platelets in a meteorite [2]. The mineral is now called Moissanite in his honour, and this has also become the name of commercial gemstones made from SiC. However, SiC is very rare in nature and has not been found freely yet, this is probably one cause of its relatively late discovery.

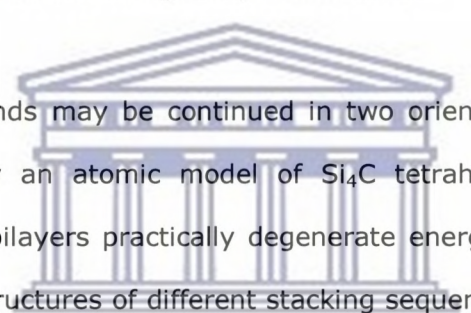
The history of man-made SiC started in 1891, when Acheson produced SiC in an electric melting furnace, mainly for grinding and polishing purposes [3]. Later, in the 1950s, when research on solid state electronic devices started, SiC was one of the semiconductor materials studied. In 1955 Lely [4] introduced a crystal growth technique to produce high quality bulk SiC, but the problem of producing large-area defect-free single crystals has not been solved, making high quality device fabrication impossible.

Later, in 1978 the so-called seeded sublimation epitaxy or modified Lely method was developed by Tairov and Tsvetkov [5], advancing the research field. Recently the most commonly used technique for epitaxial growth of SiC is the vapor-phase epitaxy (VPE) method usually realized in a chemical vapor deposition (CVD) reactor.

### 3.1 PHYSICAL PROPERTIES OF SiC

#### 3.1.1 The crystal structure

SiC has a complex crystal structure in combination with the different polytypes, it has serious implications on the structure and the properties of its surfaces. All polytypes have a hexagonal frame with a carbon atom situated above the center of a triangle of Si atoms and underneath a Si atom belonging to the next layer figure 3.1. The distance,  $a$ , between neighboring silicon atoms is approximately 3.08 Å for all polytypes [6]. The carbon atom is positioned at the center of mass of the tetragonal structure outlined by the four neighboring Si atoms so that the distance between the C atoms to each of the Si atoms (clearly marked as C-Si in fig. 3.1) is the same.



The tetrahedral Si-C bonds may be continued in two orientations different by 60° as shown in figure 3.1 by an atomic model of Si<sub>4</sub>C tetrahedral or SiC<sub>4</sub>. In SiC the orientation of adjacent bilayers practically degenerate energetically [7] which leads to many different crystal structures of different stacking sequence, and is called polytypes. The difference between the polytypes of SiC is the stacking order between succeeding double layers of carbon and silicon atoms. Figure 3.2 shows the stacking sequence for the most common polytypes, namely 3C, 4H and 6H. The 3C-SiC (zinc blende) and 2H-SiC (Wurtzite) modifications have pure cubic and hexagonal staking, respectively, see figure 3.2.

Generally, the different polytypes have broadly ranging physical properties [8], therefore, silicon carbide can be viewed as a family of materials. For example, all of the more than 200 known polytypes have an indirect bandgap, but it varies in a wide range from 2.3 (3C) to 3.33 eV (2H) as the hexagonality increases from 0 to 100 %. The well-known Choyke-Hamilton-Patrick rule [9] predicts a linear relationship between the bandgap and the degree of hexagonality up to 50 %.

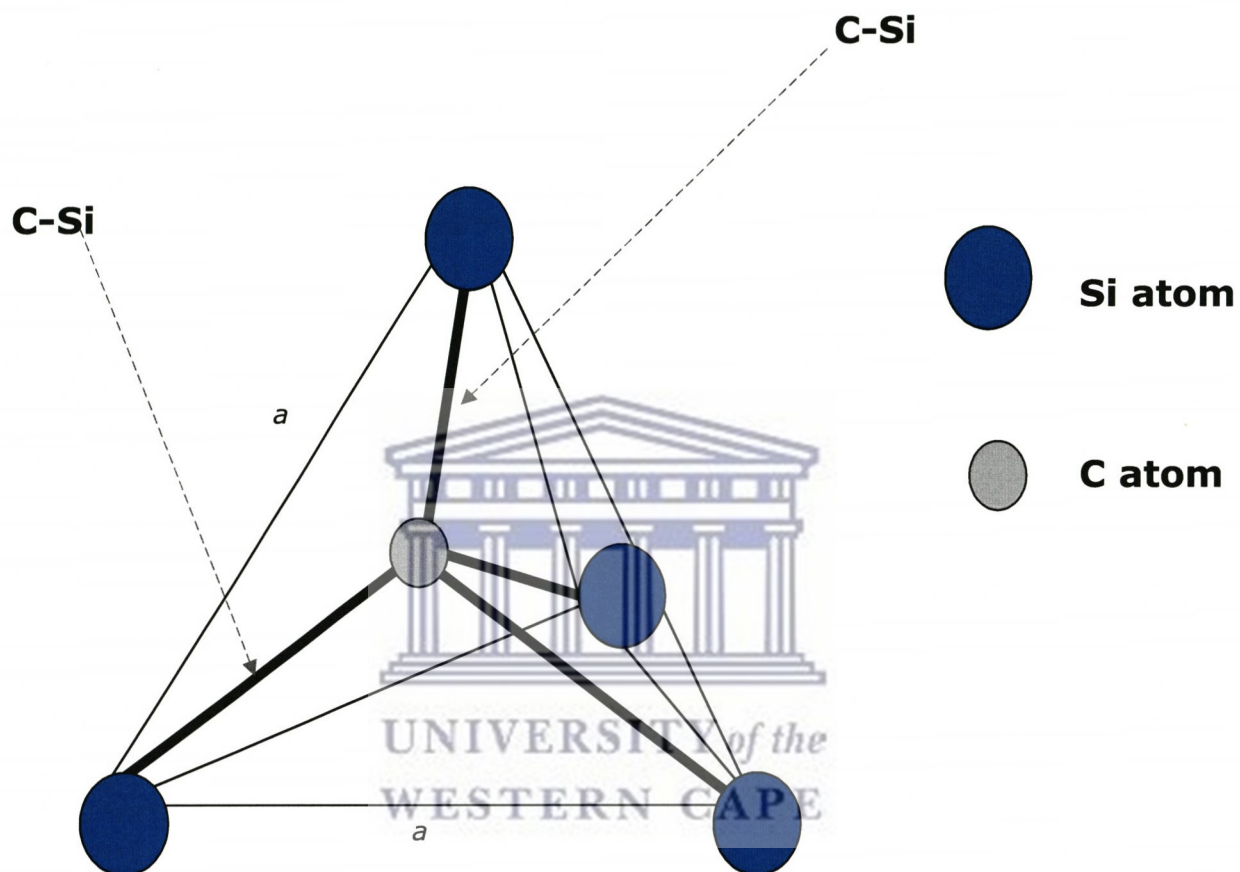


**Figure 3.1:** The tetragonal bonding of carbon atom with four nearest silicon neighbours. The distances  $a$  and C-Si are approximately  $3.08 \text{ \AA}$  and  $1.89 \text{ \AA}$  respectively.

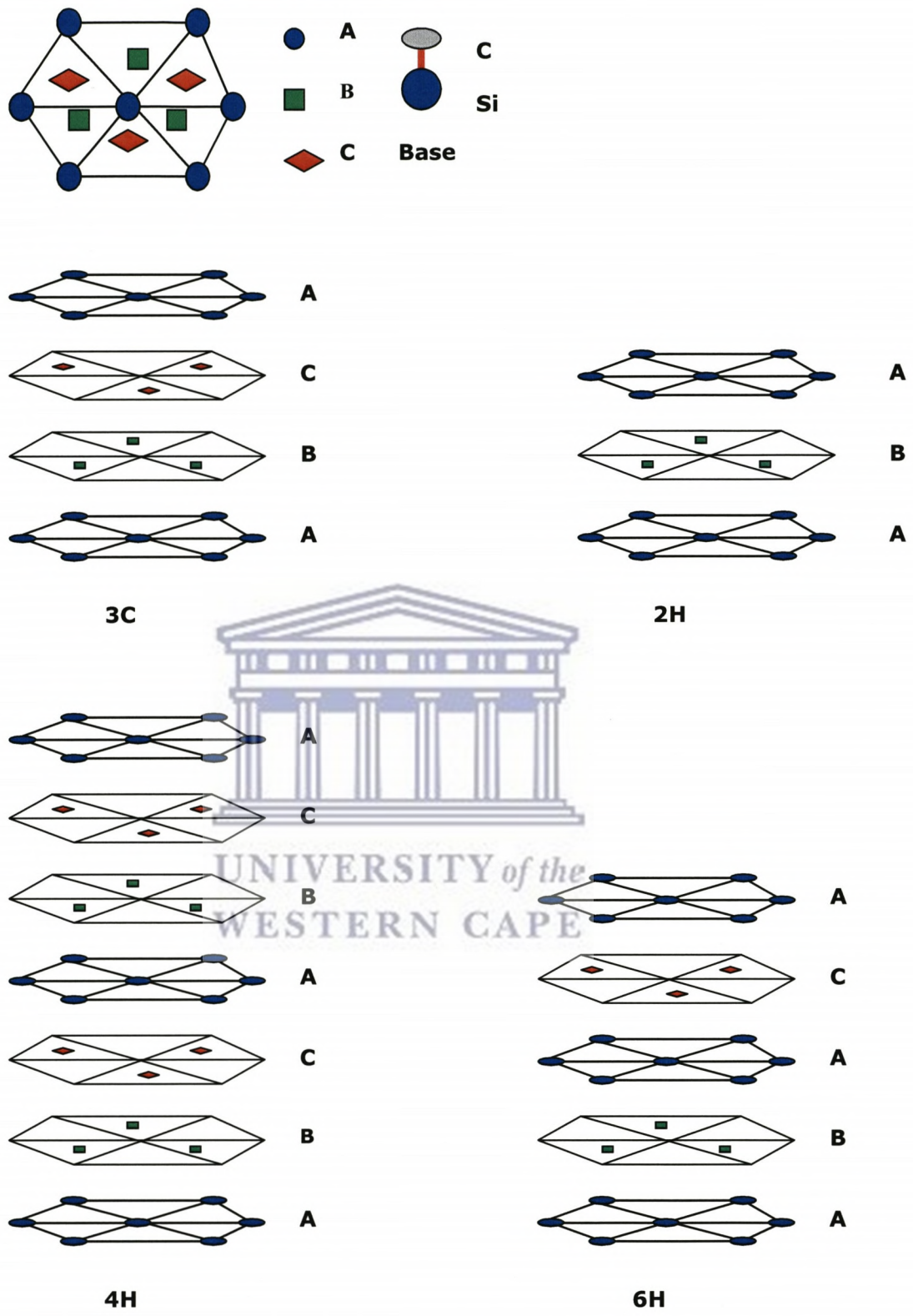


**Figure 3.2:** The stacking sequence of double layers of the three most common SiC polytypes.

### 3.1.2 Band structure

SiC is known for its different polytypes, each with a different band structure and a peculiar bandgap value. However all polytypes of SiC have an indirect bandgap. The values of the indirect bandgap for different polytypes are shown in the table 3-1 below.

**Table 3.1:** Bandgap of different polytypes of SiC [10].

SiC Polytype	Indirect band gap (eV)
3C-SiC	2.39
2H-SiC	3.33
4H-SiC	3.26
6H-SiC	3.02
8H-SiC	2.73
15R-SiC	2.99
21R-SiC	2.85
33R-SiC	3.01

### 3.1.3 Lattice parameters and density

Table 3-2 lists lattice parameters and density for various structural types of SiC at room-temperature [11]. The lattice parameter and density of SiC can be determined from the masses of its atoms that compose this material.

**Table 3.2:** Lattice parameters and density of SiC polytypes at room temperature [14].

Polytype	Density (g/cm <sup>3</sup> )	Lattice Parameter (nm)
2H-SiC	3.219	a=0.308, c = 0.503
3C-SiC	3.215	a=0.436
4H-SiC	3.215	a=0.308, c = 1.006
6H-SiC	3.215	a=0.308, c = 1.509
15R-SiC	-	a=0.307, c = 3.770
21R-SiC	-	a=0.307, c = 5.278

The density of any solid can be determined from the unit cell using the following:

$$\rho = \frac{\text{Weight of ions within unit cell}}{\text{Volume of the unit cell}}$$

$$= \frac{n(\sum M_C + \sum M_A)}{V_C N_{AV}} \quad (3-1)$$

Where  $n$  = number of formula unit cell.

$\sum M_C$  = sum of atomic weights of all cations within the unit cell.

$\sum M_A$  = sum of atomic weights of all anions within the unit cell.

$V_C$  = Unit cell volume.

$N_{AV}$  = Avogadro's constant.

The lattice parameter  $a$  of SiC can be calculated from the fact that the atoms in SiC are arranged in a manner that they touch along the body diagonal with length  $\sqrt{3}a$ . The Si-C distance is thus equal to one-fourth the length of the body diagonal. The atomic radius of Si is 0.118 nm, while that of C is 0.071 nm, it follows that

$$\frac{\sqrt{3}}{4}a = 0.118 + 0.072 \quad a = 0.436 \text{ nm}$$

Given that each unit cell has four C and four Si atoms with molecular weight of 12 and 28.09, respectively Applying equation 3.1 gives



$$\rho = \frac{4(12 + 28.09)}{\left(6.022 \times 10^{23}\right)\left(0.436 \times 10^{-9}\right)^3} = 3.21 \text{ g/cm}^3 \quad (3-2)$$

The lattice parameter and density of 3C-SiC at room temperature is 0.4358 nm and 3.21 g/cm<sup>3</sup>, respectively. At high temperatures, the lattice parameter of SiC is reported to slightly increase with the increase in temperature [1]. This reported change in lattice parameter at high temperatures thus gives thermal expansion but an insignificant change (~0.5% at 1000 °C).

### 3.1.4 Thermal properties

In light of the scope of this work, it is important to review the thermal properties of Silicon Carbide as this material plays an important role in the heat transport during nuclear plant operation. Silicon carbide is one of a few crystals that can be classified as high thermal conductivity solids. According to Slack's estimation [7], pure SiC single crystal has a thermal conductivity of 490 W/(mK) at room temperature. Collins et al. [12] have investigated the thermal conductivity of Chemical Vapor Deposited (CVD) SiC. This material manufactured using CVD has been reported to exhibit almost the same conductivity as the single crystalline material.

The thermal conductivity,  $K$ , of SiC can be determined by the thermal diffusivity,  $\alpha_d$ , the density,  $d$ , and the specific heat,  $c_p$ , using the following relationship

$$K = \alpha_d c_p d \quad (3.3).$$

The thermal diffusivity is experimentally measured by several techniques. The thermal flash method is currently the most prevalent technique for measuring the thermal diffusivity.

The thermal conductivity of SiC varies depending on the polytype of the material (see table 3-3).

### 3.1.5 Thermal expansion

Thermal expansion of  $\beta$ -SiC has been reported in several papers measured over a wide temperature range using X-ray diffraction method [1]. Dilatometry [4] and interferometry [13] were also used to determine the thermal expansion coefficient.

### 3.1.6 Electrical properties

SiC shows a high breakdown field and high drift velocity, a summary of the physical properties of some SiC polytypes is shown in table 3-3.

**Table 3-3:** Summary of physical properties of some SiC polytypes [15-16].

	3C-SiC	4H-SiC	6H-SiC
Lattice parameter [nm]	0.436	0.307	0.308
Band Gap [eV]	2.4	3.3	3.0
Satur. El. Velocity x $10^6$ [ $cm.s^{-1}$ ]	22	20	20
El. Mobility [ $cm^2V^{-1}s^{-1}$ ]	1000		1140
Hole mobility [ $cm^2V^{-1}s^{-1}$ ]	50	120	850
Breakdown field [ $MV cm^{-1}$ ]	2	3	
Thermal conductivity [ $Wcm^{-1}s^{-1}$ ]	3.2	3.7	4.9

## 3.2 Chemical properties of SiC

The chemical properties of SiC has been previously reviewed by L. Snead et. al [11] in their paper titled "handbook of SiC properties for fuel performance modeling". We give a brief description based on this review paper. Silicon Carbide is described as the only compound of Silicon and Carbon. This compound was originally produced at high

temperature via eletro-chemical reaction of high purity silica sand and carbon in an electric furnace. The general reaction for the production of SiC is:



Acheson [3] suggested that  $\alpha$ -SiC formed above 2100 °C and  $\beta$ -SiC at 1000-1600 °C. This compound is a non-oxide and the oxidation at high-temperatures is highly possible. Oxidation can compromise the quality of the material therefore it becomes a critical issue. Many studies on the oxidation behavior of SiC have been conducted [17–31]. The oxidation of SiC is generally divided into two regions: passive and active oxidations, with a broad transition band. At high oxygen partial pressures and high temperatures, SiC reacts with oxygen to form a SiO<sub>2</sub> surface scale, accompanied with significant mass gain (passive oxidation).



The structure of the resultant SiO<sub>2</sub> scale is amorphous at the temperatures below 1400 °C. In contrast, the crystallization rate from amorphous SiO<sub>2</sub> to cristobalite has a maximum value around 1677 °C, and the cristobalite is therefore more stable at higher temperatures. The Pilling–Bedworth ratio, which is defined as the ratio of the volume of the resultant oxide to the consumed substrate volume, i.e., the volume ratio between the SiO<sub>2</sub> scale and the SiC substrate, is  $\sim 1$  (forming a good bond at the interface with a very small strain gap). In contrast, the diffusion rate of oxygen in the SiO<sub>2</sub> scale is very low compared with other oxides. The SiO<sub>2</sub> therefore effectively acts as a protective layer to prevent further oxidation.

The oxidation kinetics of SiC is dependent on many factors: atmosphere, temperature, oxygen partial pressure, microstructure, etc. The oxidation mechanism in a dry atmosphere can be classified into linear-parabolic or parabolic behavior below the melting point of cristobalite ( $T_m = 1728\text{ }^\circ\text{C}$ ) [21]. Luthra et al. [24] suggested that the passive oxidation of SiC is a mixed control mechanism, influenced both by an interface reaction and diffusion. However, the primary rate-controlling process for passive oxidation is still considered to be diffusion of oxygen through the growing oxide scale. Oxygen can diffuse through  $\text{SiO}_2$  via two mechanisms: (1) interstitial (nominally molecular) oxygen diffusion through the free volume of the silicate structure and (2) network oxygen ion diffusion through the  $\text{SiO}_4$  tetrahedral network [27, 28].

A study by Ramberg et al. [26] identified that the high-temperature transition from interstitial-dominant ( $<1400\text{ }^\circ\text{C}$ ) to network dominant ( $>1400\text{ }^\circ\text{C}$ ) oxygen transport is only observed for amorphous  $\text{SiO}_2$  scales, while the cristobalite scale did not show such a transition. This fact can explain a comparatively lower oxidation rate obtained below  $1400\text{ }^\circ\text{C}$ . It was also identified that there is no significant difference between the rates of molecular oxygen diffusion in cristobalite and in amorphous  $\text{SiO}_2$ , although the possible mechanism is believed to be the change of the diffusion rate of oxygen in the  $\text{SiO}_2$  scale due to the crystallization from amorphous  $\text{SiO}_2$  to  $\beta$ -cristobalite [32-34].

The oxidation process is accelerated by the presence of impurities and residual sintering additives which affect the microstructure of the protective  $\text{SiO}_2$  scale [34]. In contrast, significant differences have been observed in the interaction of oxygen with different polytypes and different surface orientations of single crystal SiC [22, 26]. The oxidation kinetics also depends on the type and size of the SiC form, e.g., sintered body or powder. The SiC powder can be oxidized in air at  $700\text{ }^\circ\text{C}$  [31].

Moreover, the formation of  $\text{SiO}_2$  bubbles at extremely high temperatures can be closely related to the oxidation mechanism of SiC [21, 29]. The transition from passive

oxidation to bubble formation depends on the oxygen partial pressure and test temperature. The linear and parabolic oxidation rates were accelerated by the bubble formation. Water vapor can further accelerate the oxidation of SiC [19, 30] extending the linear kinetic region and increasing the parabolic rate constant.

At low oxygen partial pressures and very high temperatures, SiC readily decomposes to SiO and CO gases without forming a protective SiO<sub>2</sub> scale (active oxidation) following the reaction described in the equation (3.6).



According to Schneider et al. [18], there is a wide gap in oxygen pressure required for the active-to passive oxidation transition. The active-to-passive oxidation transition is closely dependent on the impurity content in the SiC form. For instance, the partial oxygen pressure required to initiate the active oxidation of a sintered SiC, which possesses slight residual sintering aids as impurities, is  $\sim 10^4$  times higher than that of pure CVD SiC [17].

UNIVERSITY of the  
WESTERN CAPE

The active oxidation rates increases with increasing oxygen partial pressure [35-38]. Some basic oxides such as PbO and Na<sub>2</sub>O, can dissolve the protective SiO<sub>2</sub> scale to form silicates [20]. Silicon carbide is also corrosive in Na<sub>2</sub>SO<sub>4</sub> [36, 37] and a mixture of Na<sub>2</sub>CO<sub>3</sub> and KNO<sub>3</sub>. Moreover, SiC reacts readily with chlorine and sulfur above 900 °C and 1000 °C, respectively. In contrast, SiC is chemically inert to HCl, H<sub>2</sub>SO<sub>4</sub>, HF, NaOH, and a mixture of HF and HNO<sub>3</sub>, even if the oxidizing acids are heated [39].

### **3.3 Survey on Silicon Carbide Bulk Synthesis**

Since the discovery of SiC, there has been a shortage of suitable crystal growth of silicon carbide processes. Silicon carbide does not melt under any reasonably attainable pressure and sublimates at 1800 °C. This feature restrains and makes it difficult to grow this semiconductor material using conventional techniques used for growth of silicon. Silicon Carbide exists in many polytypes with different electronic properties and this polytypes can grow under matching conditions. Despite these difficulties, there has been a major breakthrough in processes involved in the synthesis of silicon carbide. Although the crystal growth is not the primary purpose of this study, but an insight to their production could boost and deepen the understanding as part of the literature survey of SiC. This section deals mainly with the techniques developed in the late fifties and later improved to be re-used in the early eighties for the production of SiC. However, it must be noted that these techniques are used for bulk production of industrial SiC and we describe it since our SiC target used, is a bulk single crystal produced by an American company Cree.



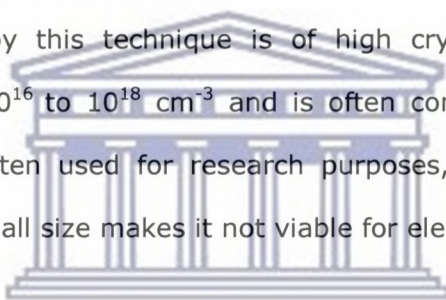
#### **3.3.1 Acheson process**

In this process a through-type furnace is used, in which a mixture of silica and carbon with a small percentage of sawdust and common salt are heated to about 2700 °C. The basic design of the original electric furnace has remained unchanged, despite larger sizes and better efficiency. The result is a combination of crystallites and polycrystalline agglomerates in different states of perfection, but heavily contaminated due to the low purity of the source material. This technique is mostly used for the production of SiC for grinding applications, but also for the fabrication of substrates for Chemical Vapor Deposition and LPE.

### 3.3.2 Lely process

This was the first technique used for the production of semiconducting SiC and was published in 1955 [40]. The SiC powder source is introduced in a porous graphite sleeve, across which a temperature gradient is impressed with a source temperature between 2200 and 2700 °C; SiC crystals are nucleated on the sleeve and the growth proceeds along the basal plane, which is parallel to the crystallographic *a*-axis. The growth material shows a distribution of crystals of different size and polytypes: mainly 6H-SiC (75-95%), 4H, 15R and, less frequently, 8H, 21R and 33R. Since the growth material has a typical pyramid shape, it is necessary to ground away the top part of the crystal, obtaining a platelet of hexagonal shape and 0.3 to 0.35 mm thickness.

The material obtained by this technique is of high crystal quality, with a doping concentration between  $10^{16}$  to  $10^{18}$  cm<sup>-3</sup> and is often completely free of micro pipes [41]. This material is often used for research purposes, but the irregularity of the platelet shape and the small size makes it not viable for electronic applications.



### 3.3.3 Modified Lely process

In this technique a seed crystal is introduced in the Lely chamber and growth proceeds by vapor transport of carbon and silicon bearing species from the source to the growth site. The typical growth pressure is less than 20 Torr, the growth temperature between 2100 and 2400 °C and the temperature gradient between the source and the seed between 20 to 35 °C/cm. The growth is usually performed on {0001} face of 6H or 4H-SiC seed, Si or C face.

### 3.3.4 Chemical Vapor Deposition (CVD)

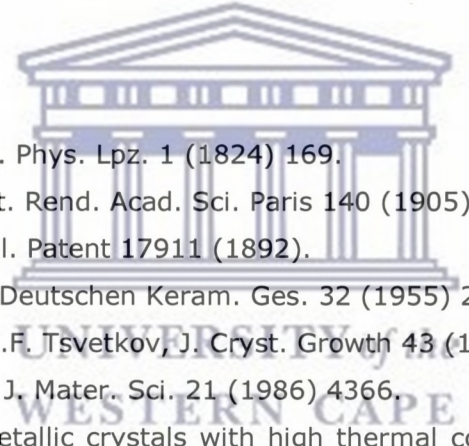
High quality bulk 3C-SiC has been grown by Chemical Vapor Deposition [42], using gas mixture and a growth temperature between 1650 and 1750 °C. The crystals were deposited on resistively heated graphite rods; a thickness of 3 mm and a width less than

10 mm were obtained. Also 6H-SiC has been grown by CVD [43], with growth rates of 0.5 mm/h. The control of Si/C ratio is much better in this technique than in sublimation growth, but CVD is not ready for industrial bulk growth applications.

### 3.3.5 Growth from liquid phase

The crystal growth from the liquid phase is widely used for many types of semiconductors, but for SiC has not been considered promising for two main reasons: low solubility of SiC in the Si melt; inclusions incorporated in grown crystal due to parasitic phase formation. However, high quality SiC crystals with no micropipes and low dislocation density have been grown from melt solutions [44].

## 3.4 References

- 
- [1] J.J. Berzelius, *Ann. Phys. Lpz.* 1 (1824) 169.
  - [2] H. Moissan, *Compt. Rend. Acad. Sci. Paris* 140 (1905) 405.
  - [3] E.G. Acheson, *Engl. Patent* 17911 (1892).
  - [4] J.A. Lely, *Bericht. Deutschen Keram. Ges.* 32 (1955) 229.
  - [5] Y. M. Tairov and V.F. Tsvetkov, *J. Cryst. Growth* 43 (1978) 209.
  - [6] Li and Bradt et al. *J. Mater. Sci.* 21 (1986) 4366.
  - [7] G.A. Slack, *Nonmetallic crystals with high thermal conductivity. J. Phys. Chem. Solids* 34 (1973), pp. 321–335.
  - [8] F. Bechstedt, P. Käckell, A. Zywietz, K. Karch, B. Adolf, K. Tenelsen, and J. Furthmüller, *Phys. Stat. Sol. B* 202 (1997) 35.
  - [9] M.A. Pickering, R.L. Talyor, J.T. Keeley, G.A. Graves, *Nucl. Instrum. And Meth. A* 291 (1990) 95.
  - [10] Yoshida S., "Band structure of SiC: Overview" in *Properties of silicon carbide*, ed. by Harris G. L., INSPEC, London (1995)74.
  - [11] L.L. Snead, T.Nozawa, Y. Katoh, T.-S. Byun, S. Kondo, D.A. Petti, *J. of Nucl. Mater.* 371 (2007) 329–377.
  - [12] A.K. Collins, M.A. Pickering, R.L. Taylor, *J. Appl. Phys.* 68 (1990) 6510.
  - [13] A.F. Pojur, B. Yates, B.T. Kelly, *J. Phys. D* 5 (1972) 1321.
  - [14] JCPDS 29-1126 ~ 29, 39-1196, 22-1319.



- [15] P. Mandracci, Growth and characterization of SiC thin films by plasma assisted techniques for electronic applications, Ph.D thesis, (2001).
- [16] T. Narushima, T. Goto, T. Hirai, *J. Am. Ceram. Soc.* 72 (1989) 1386.
- [17] M.J.H. Balat, *J. Eur. Ceram. Soc.* 16 (1996) 55.
- [18] B. Schneider, A. Guette, R. Naslain, M. Cataldi, A. Costecalde, *J. Mater. Sci.* 33 (1998) 535.
- [19] E.J. Opila, *J. Am. Ceram. Soc.* 82 (1999) 625.
- [20] C. Eric Ramberg, W.L. Worrell, *J. Am. Ceram. Soc.* 84 (2001) 2607.
- [21] T. Goto, H. Homma, *J. Eur. Ceram. Soc.* 22 (2002) 2749.
- [22] Y. Song, F.W. Smith, *J. Am. Ceram. Soc.* 88 (2005) 1864.
- [23] J.A. Costello, R.E. Tressler, *J. Am. Ceram. Soc.* 69 (1986) 674.
- [24] K.L. Luthra, *J. Am. Ceram. Soc.* 74 (1991) 1095.
- [25] T. Narushima, T. Goto, Y. Iguchi, T. Hirai, *J. Am. Ceram. Soc.* 74 (1991) 2583.
- [26] C. Eric Ramberg, G. Cruciani, K.E. Spear, R.E. Tressler, C.F. Ramberg Jr., *J. Am. Ceram. Soc.* 79 (1996) 2897.
- [27] J.D. Kalen, R.S. Boyce, J.D. Cawley, *J. Am. Ceram. Soc.* 74 (1991) 203.
- [28] M.A. Lamkin, F.L. Riley, R.J. Fordham, *J. Eur. Ceram. Soc.* 10 (1992) 347.
- [29] T. Narushima, T. Goto, Y. Yokoyama, M. Takeuchi, Y. Iguchi, T. Hirai, *J. Am. Ceram. Soc.* 77 (1994) 1079.
- [30] T. Narushima, T. Goto, Y. Iguchi, T. Hirai, *J. Am. Ceram. Soc.* 73 (1990) 3580.
- [31] T. Iseki, in: JSPS (Ed.), *Advanced Silicon Carbide Ceramics*, Uchida Rokakuho Publishing Co., Ltd., Tokyo, (2001).
- [32] N.S. Jacobson, *J. Am. Ceram. Soc.* 76 (1993) 3.
- [33] T. Narushima, T. Goto, T. Hirai, Y. Iguchi, *Mater. Trans.* 38 (1997) 821.
- [34] S.C. Singhal, F.F. Lange, *J. Am. Ceram. Soc.* 58 (1975) 433.
- [35] G. Ervin Jr., *J. Am. Ceram. Soc.* 41 (1958) 347.
- [36] R.E. Tressler, M.D. Meiser, T. Yonushonis, *J. Am. Ceram. Soc.* 59 (1976) 278.
- [37] T. Goto, H. Homma, *J. Eur. Ceram. Soc.* 22 (2002) 2749.
- [38] T. Narushima, T. Goto, Y. Iguchi, T. Hirai, *J. Am. Ceram. Soc.* 74 (1991) 2583.
- [39] K. Yamada, M. Mori, in: S. Somiya, Y. Inomata (Eds.), *SiC Ceramics*, Uchida Rokakuho Publishing Co., Ltd., Tokyo, (1988).
- [40] Lely J.A., *Ber. Detsch. Kerm. Ges.*, 32 (1955) 229.
- [41] Larkin, D. J., An overview of SiC epitaxial growth. *Mater. Res. Soc. Bull.* 22 (1997) 36.

- [42] Gorin S. N. and Pleutushkin A. A., *Izvestiya Akademii Nauk, USSR, Ser.Fizicheskaya*, 28 (1964) 1310.
- [43] Kordina O., Hallin C, Ellison A., Bakin A. S., Ivanov I. G., Henry A., Yakimova R., Touminen M., Vehanen A.,and Janzen E., "High temperature chemical vapor deposition of SiC", *Appl. Phys. Lett.*, vol 69 (1996) 1496.
- [44] Marshall R. C. "Growth of silicon carbide from solution", *Mater. Res. Bull.*, 4. (1969) S73.



UNIVERSITY *of the*  
WESTERN CAPE

## CHAPTER-4

### LITERATURE SURVEY ON THE RADIATION INTERACTIONS AND EFFECTS ON SIC

---

#### 4.1. INTERACTIONS OF RADIATIONS WITH MATTER

This section discusses and describes the major interactions of radiations such as protons, neutrons and  $\gamma$ -ray with bulk materials. The theoretical account given here is necessarily a brief and it is based on the work done by Sjirk [1], P. Rinard et al. [2] and G. Nelson et al. [3]. For a more detailed discussion, see Refs. [1], [2] and [3].

##### 4.1.1 Interactions between materials and protons

The interaction between a proton and an atomic nucleus affects the proton flux (nuclear reactions), and the proton trajectory ((in) elastic scattering). The most important contribution to proton scattering comes from the electromagnetic interaction with the nucleus. This gives rise to small scattering angles, but since there are a large number of collisions, the effect can be considerable. If the impact parameter (distance of closest approach between proton and nucleus) is small also the hadronic interaction contributes to elastic scattering. In addition inelastic interactions can occur: these can either be an inelastic scattering process during which the incident proton transfers energy to the nucleus (which will then be in an excited state and decay by  $\gamma$ -emission) or a nuclear reaction process (such as  $(p,n)$ ,  $(p,d)$ ,  $(p,2p)$  or  $(p,3p)$  ) where the incident proton will disappear. In case of scattering of protons by very light nuclei, such as protons in hydrogen, also the recoil nucleus can travel a considerable length before its energy is fully deposited.

Because protons can produce secondary particles ( $\delta$ -electrons, nuclear reaction products or recoil nuclei) as a result from energy loss processes there can be a difference between the local energy loss and the energy absorbed by the medium therefore the following sections give a detailed type of interactions of protons with matter.

#### 4.1.1.1 Proton interaction with electrons

Within the energy range of importance in proton (from stopping protons to  $\approx 250$  MeV) it is convenient to consider two energy intervals separately:

- Low energy: below  $\approx 0.5$  MeV protons can pick up orbital electrons and form hydrogen. Also energy can be lost to atomic nuclei due to electromagnetic interactions (nuclear stopping power). These are complicated processes, but fortunately they only play a role at the very last microns of a proton track.
- High energy: for proton energies between  $\approx 0.5$  MeV and 250 MeV the atoms in the stopping medium can be excited or ionized. The collision process is well understood and in principle the stopping power can be calculated theoretically.

The mean energy loss per proton  $S$  can be described by the Bethe theory [4] which leads to the following expression:

$$\frac{1}{\rho} S = -\frac{1}{\rho} \frac{dE}{dZ} = K \frac{Z}{A} \frac{1}{\beta^2} L(\beta) \quad (4.1)$$

with:

$$K = 2\pi r_e^2 m c^2 N_{av} \approx 0.1535 \text{ MeV } m c^2 \text{ g}^{-1} \quad (4.2)$$

Where  $r_e = \frac{e^2}{4\pi\epsilon_0 mc^2}$  is the classical electron radius,  $\epsilon_0$  the permittivity of the vacuum (which is introduced by the use of SI units),  $mc^2$  is the electron rest mass energy,  $N_{av}$  Avogadro's number,  $\beta$  is the particle velocity in units of the velocity of light.

$(\beta^2 = 1 - (\frac{mc^2}{E+mc^2})^2)$ ,  $mc^2$  is the proton rest mass  $\approx 938.3$  MeV,  $E$  the proton kinetic energy,  $Z$  and  $A$  are the atomic number and relative atomic mass of the target atom.

The amount of energy loss of a proton in a medium is subject to two sources of fluctuations. The number of proton-electron collisions can fluctuate, and at the same time the energy lost in each collision varies statistically. Both distributions are characterized by a Poisson-like behaviour. In most of the proton-electron collisions only a small amount of energy is transferred from the proton to electron, due to the large ratio of proton to electron mass. There is however a small, but finite probability that a collision occurs where the energy transfer approaches  $T_{max}$  and the atomic electron is dissociated from the atom. This extracted electron is called a  $\delta$ -electrons or  $\delta$ -ray. Depending on the application it is possible to use a macroscopic, statistical description of the energy loss or a microscopic description, in which the  $\delta$ -electrons are treated separately. With the statistical description the probability of occurrence of a certain energy loss  $\epsilon$  in a medium layer with thickness  $t$  as a function of mean energy loss  $S$  and proton velocity  $\beta$  can be calculated. With the microscopic description the  $\delta$ -electron spectrum per incident proton can be calculated.

The macroscopic energy loss distribution function depends on the scale one is considering. In a thick layer a large number of collisions occur and the energy loss is expected to be distributed according to a Gaussian. For a small layer of material, however, the probability of a collision with an energy transfer close to the maximum energy transfer ( $T_{max}$ ) occurs remains constant, but its relative contribution to the total

energy loss becomes much larger. This means that larger fluctuations can occur for small layers. The parameter which describes the collision regime is called the skewness parameter  $K$ , which relates the energy loss in a medium with thickness  $t$  to the maximum energy transfer in a single collision:

$$K = \frac{\xi}{T_{max}} \quad (4.3)$$

$$\xi = \rho \frac{Z}{A} \frac{1}{\beta^2} K \cdot t \quad (4.4)$$

The symbols are as in equations (4.1), (4.2). In case  $K < 1$ ,  $\xi$  has the following physical meaning: when a proton passes through a medium with thickness  $t$ , there will occur, on the average, one collision with an atomic electron in which the proton loses an amount of energy greater than  $\xi$ . For  $K \ll 1$ , the energy distribution is described by the Landau theory [5] where the distribution has a large tail towards high energy loss. In case  $K > 1$  ( $\xi$  becomes larger than  $T_{max}$  for thick media) the energy distributions approaches a Gaussian. Vavilov has treated the energy loss distribution in a more general way, which includes the Gaussian and Landau distribution as a limiting case [6]. The Vavilov energy distribution function  $\phi_v$  is a function of  $\beta$ ,  $\kappa$  and the scaled energy loss  $\lambda$ :

$$\lambda = \frac{\epsilon - \bar{\epsilon}}{\xi} - \beta^2 - 1 + 0.577 \dots - \ln \kappa \quad (4.5)$$

Where  $\epsilon$  is the actual energy loss,  $\bar{\epsilon}$  is the mean energy loss  $\phi_v$  ( $=\rho \cdot S \cdot t$ ) 0.577... is Euler's constant and the other symbols are as previous. The actual expression for  $(\beta \kappa \lambda)$  is very complicated and is easiest evaluated numerically, for example using the algorithm of Schorr [7]. In the limit  $K \rightarrow 0$  the Vavilov theory approaches the Landau theory under the assumption that  $\xi$  remains much larger than the mean excitation energy  $I$ . This is necessary in order to treat the atomic electrons as free particles.

In case of thick absorbers the energy loss distribution approaches a Gaussian with a width  $\sigma$  given by [4]:

$$\sigma_E^2 = \xi T_{max} \left(1 - \frac{\beta^2}{2}\right) \quad (4.6)$$

$\xi$  is given by equation (4.4),  $T_{max}$  is given by equation (4.3). The Gaussian approximation is valid if the proton energy can be assumed to be constant during the passage through the absorber. This does not hold anymore for very thick absorbers. In that case one has to divide the absorber into several smaller slabs and sum the  $\sigma_E^2$  of the individual slabs.

In case the energy transfer from the proton to the electron  $T$  is much larger than the mean excitation potential  $I$ , it is also possible to use a microscopic description and explicitly consider  $\delta$ -electrons. The number of  $\delta$ -electrons  $N$  as a function of electron energy  $T$  per unit thickness can be calculated using the Bhabha cross section [8] which can be written as the product of the classical Rutherford cross section and a quantum mechanical correction for spin-1/2 particles (factor between square brackets):

$$\frac{d^2N}{dTdZ} = K \cdot \frac{\rho Z}{A} \cdot \frac{1}{\beta^2} \cdot \frac{1}{T^2} \left[ 1 - \beta^2 \frac{T}{T_{max}} + \frac{T^2}{2(E+Mc^2)^2} \right] \quad (4.7),$$

where the symbols are the same as in equations (4.1), (4.2). The difference between the classical Rutherford cross section and equation (4.7) increases for increasing proton energy and energy transfer, up to 40% for 250 MeV protons and an energy transfer of  $T_{max}$ . The meaning of  $\xi$  can also be illustrated using the integral of equation (4.7) without the quantum mechanical correction factor: this is the probability that one  $\delta$ -electron with an energy  $\xi$  is produced:

$$N(\xi, t) = K \cdot \frac{\rho Z}{A} \cdot \frac{1}{\beta^2} \cdot \frac{t}{\xi} = 1 \quad (4.8)$$

In figure 4.1 the  $\delta$ -electrons spectrum per incident proton according to equation 4.7 can be seen for a number of proton energies.

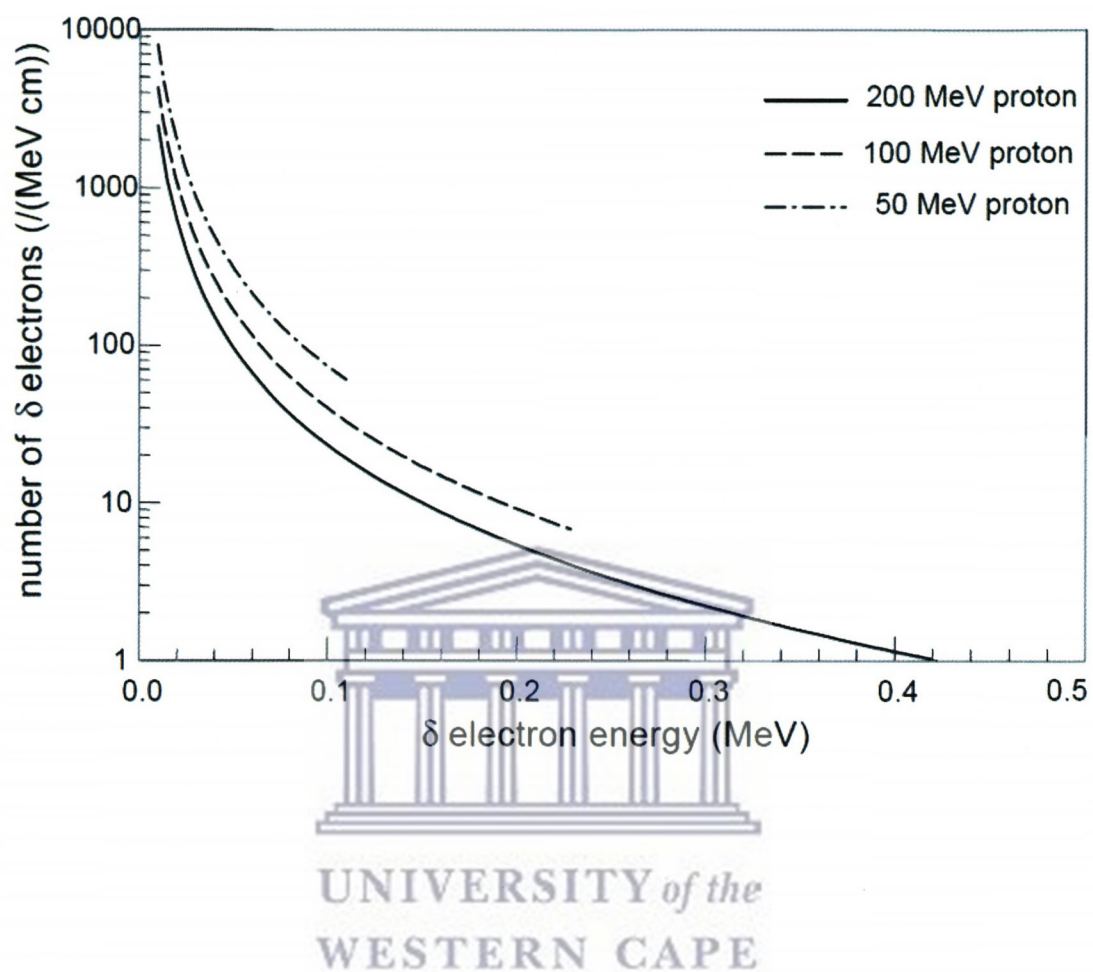


**Figure 4.1:** Number of  $\delta$ -electrons produced per incident proton per cm  $H_2O$  calculated using equation (4.7) [1].



#### 4.1.1.2 Proton interaction with nuclei: scattering

A proton will experience a deflection as it passes in the neighborhood of a nucleus. This deflection is the result of the combined interaction with the Coulomb- and hadronic field of the nucleus (the deflection caused by collisions with electrons can be neglected because of the mass ratio). The Coulomb interaction has been derived by Rutherford [4]:

$$d\sigma(\theta) = \left(\frac{e^2}{16\pi\epsilon_0}\right)^2 \frac{Z^2}{E^2} \frac{1}{\sin^4\frac{\theta}{2}} 2\pi\sin\theta \cdot d\theta \quad (4.9)$$

where  $E$  is the proton kinetic energy (in MeV) and  $d\sigma(\theta)$  the differential cross section in mb ( $\equiv 10^{-31}\text{m}^2$ ), the other symbols as in equations (4.1), (4.2). This cross section decreases very rapidly with increasing angle, and with increasing energy. The consequence is that most particles are only slightly deflected. The hadronic interaction will only play a role when the distance between the proton and the nucleus becomes very small ( $\approx$  diameter of the nucleus  $\approx 1.3 \times 10^{-31} A^{1/3}$  m). Although the mechanism of the hadronic interaction is very complicated, it manifests itself experimentally with deviations from the Rutherford scattering cross section, which can be parametrized using optical models [9]. In figure 4.2 the ratio between the Rutherford cross section and observed elastic cross section (so including the hadronic interaction) can be seen as a function of angle in case of 180 MeV protons on  $^{16}\text{O}$ . The elastic cross section has been calculated using the DWUCK code, with parameters for oxygen from [9].

In addition to this elastic hadronic interaction, also inelastic interactions occur, which are described in the next section. Only for large scattering ( $>4^\circ$ ) angles the difference becomes significant. The probability that a scattering occurs with an angle more than  $4^\circ$  in 1 cm  $\text{H}_2\text{O}$  is less than 0.05 % (this can be calculated using equation (4.4)). So in practice only the small angle deflections, which are caused by distant collisions, contribute.

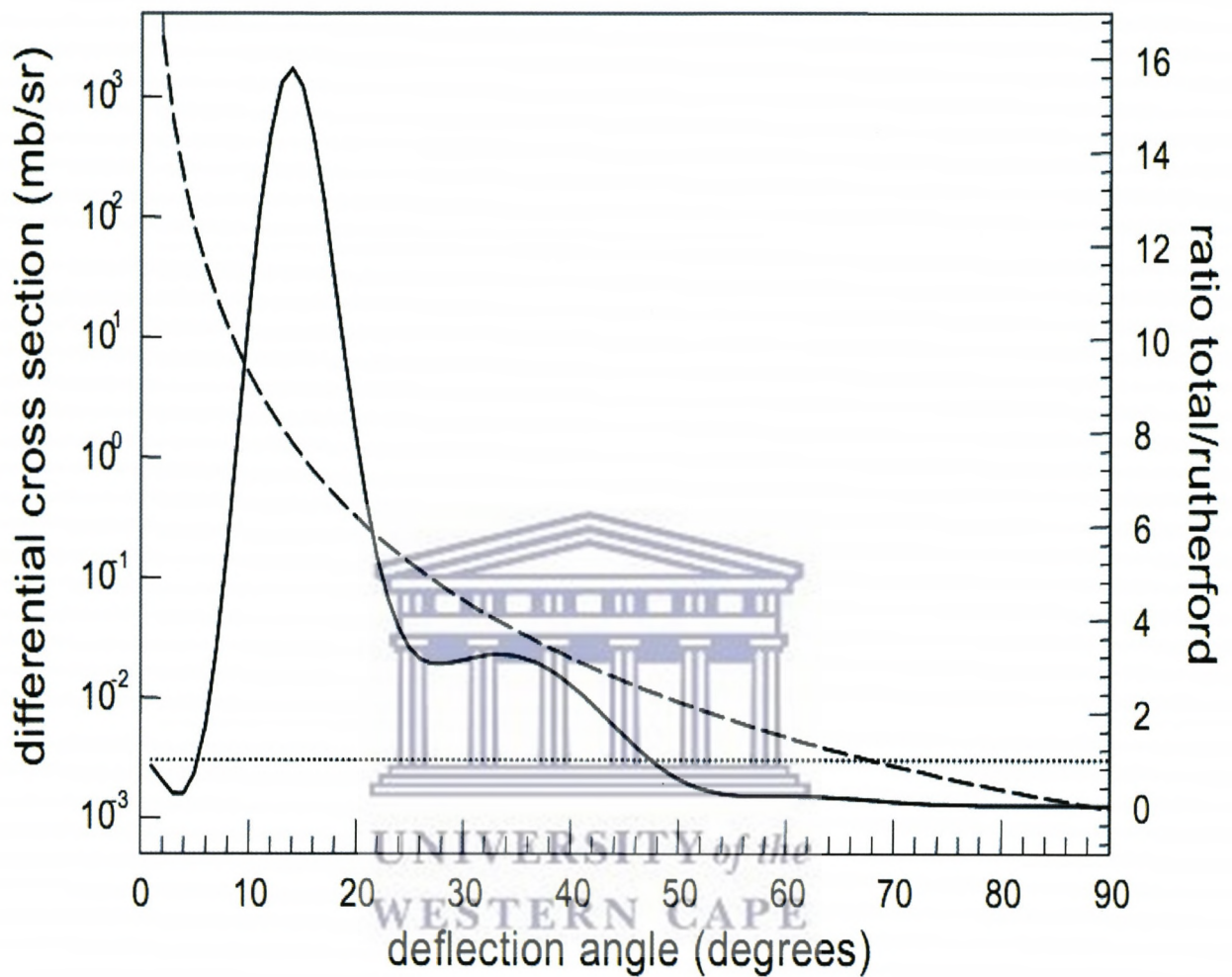


**Figure 4.2:** Solid line (scale on right axis): ratio between total elastic cross section of 180 MeV protons incident on  $^{16}\text{O}$  (using DWUCK4 ) and Coulomb contribution (using equation (4.9) ) as a function of deflection angle. Dotted line: ratio = 1. Dashed line (scale on left axis): Coulomb contribution [1].

However because of the large number of interactions the total effect is considerable. A multiple scattering theory has been derived by Molière [10] and later on improved by Bethe [4] which is valid for scattering angles  $\theta \leq 30^\circ$ . Analog to the energy distribution function it is possible to derive macroscopically an angular deflection distribution function.

According to Molière this distribution function can be expressed as a series expansion which involves complicated functions. The limiting case for many collisions again is a Gaussian distribution:

$$f(\theta) = \frac{1}{\sqrt{2\pi} \theta_0^2} \exp \left[ -\left( \frac{\theta_{plane}}{2\theta_0} \right)^2 \right] d\theta \quad (4.10)$$

For the calculation of the width  $w$  (the mean squared scattering angle projected on a plane  $\theta_{plane}^{rms}$ , which is  $\frac{1}{\sqrt{2}} \theta_{space}^{rms}$  of the Gaussian several approximations exists.

In [11] is shown experimentally that the Highland formula gives the best results for protons:

$$\theta_0 \approx \frac{14.1 \text{ MeV}}{\beta^2 (E + Mc^2)} \sqrt{\frac{t}{L_R}} \left[ 1 + \frac{1}{9} \log_{10} \left( \frac{t}{L_R} \right) \right] \text{ rad} \quad (4.11)$$

where  $t$  is the thickness of the medium,  $E$  the proton kinetic energy,  $Mc^2$  the proton rest mass (expressed in MeV) and  $L_R$  the radiation length of the material, which is the distance over which the electron energy is reduced to a factor  $1/e$  due to bremsstrahlung only (this is tabulated e.g. in [12], for water  $L_R = 36.1 \text{ g/cm}$ ). Although the radiation length is a material property derived for electrons, this formula turns out to fit the experimental data with protons well [11]. For small angles we can approximate

$$\theta_{space}^2 \approx (\theta_{plane,x}^2 + \theta_{plane,y}^2).$$

The deflection in x and y-direction are independent and identical distributed. The Highland formula works under the assumption that the proton kinetic energy remains constant during the passage, which means that the thickness t has to be small. In the case of thick absorbers, it is possible to apply equation (4.11) to a thin slab and in analog way as for the energy straggling by taking the sum of the  $\theta^2_0$  of the individual slabs. Because of the artificial use of the radiation length however, it is necessary to remove the factor  $[1 + \frac{1}{9} \log_{10}(\frac{t}{L_R})]$  from the integral, thus treating it as a correction factor which depends on the *entire* target thickness [11]. The path length travelled by the proton will increase due to the multiple scattering process. This means that the average penetration depth Z of the protons will be shorter than their CSDA range R. The difference between the lengths can be calculated using [4]:

$$\frac{R-Z}{R} = \int_0^{E_0} \frac{1}{(1 - \cos \theta)} \left(-\frac{dE}{dz}\right)^{-1} dE \quad (4.12)$$

Where  $\frac{R-Z}{R}$  is the mean difference and  $\frac{1}{(1 - \cos(\theta))}$  is the mean deflection angle. In [13] they are tabulated for different materials: it turns out that for protons in water for example the effect is negligible above 1 MeV.

When the energy of the proton in some applications is much higher than the Coulomb-barrier, protons will have a probability of reacting with the nucleus other than by elastic or inelastic scattering. This causes a decrease of the proton flux with depth, already long before the end of the proton range. When we assume the CSDA approximation, this can be described by:

$$\Phi = \Phi_0 \exp\left(-\frac{\rho N_{av}}{A_{eff}} \int_E^{E_0} \sigma_{inelas}(\dot{E}) \frac{d\dot{E}}{S(\dot{E})}\right) \quad (4.13)$$

where  $\Phi$  is the flux of protons with energy  $E$ ,  $\Phi_0$  the initial flux,  $E_0$  the start energy,  $S(E)$  the stopping power and  $\sigma_{inelas}(\dot{E})$  is the enelastic nuclear reaction cross section.

Figure 4.3 shows the experimental points together with a fit that has been made by Seltzer [14] using the GNASH-code [15].

With respect to the reaction products the situation is more complicated. The secondary particles can be neutrons, protons and recoil fragments. The energy transferred to the recoil fragments will be deposited locally, but secondary protons can travel a considerable distance before stopping. The secondary neutrons will either escape from the medium or produce another nuclear reaction, in which tertiary particles can be produced.

In general it is not possible to make an analytical calculation of the contribution of nuclear reactions to the energy deposition as a function of depth. Berger [15] uses the estimate that 60 % of the initial proton energy (i.e. before the reaction) is deposited locally while the other 40 % escapes from the medium in the form of neutrons and  $\gamma$ 's. Monte Carlo calculations, however, in which the secondary particles are separately followed are not in agreement with this and show that a depth dependent contribution is deposited. The result for the flux reduction of the primary protons using equation (4.13) can be seen in figure 4.4. The steepness of flux reduction is slightly larger for the 80 MeV proton beam, due to the slightly higher cross section.

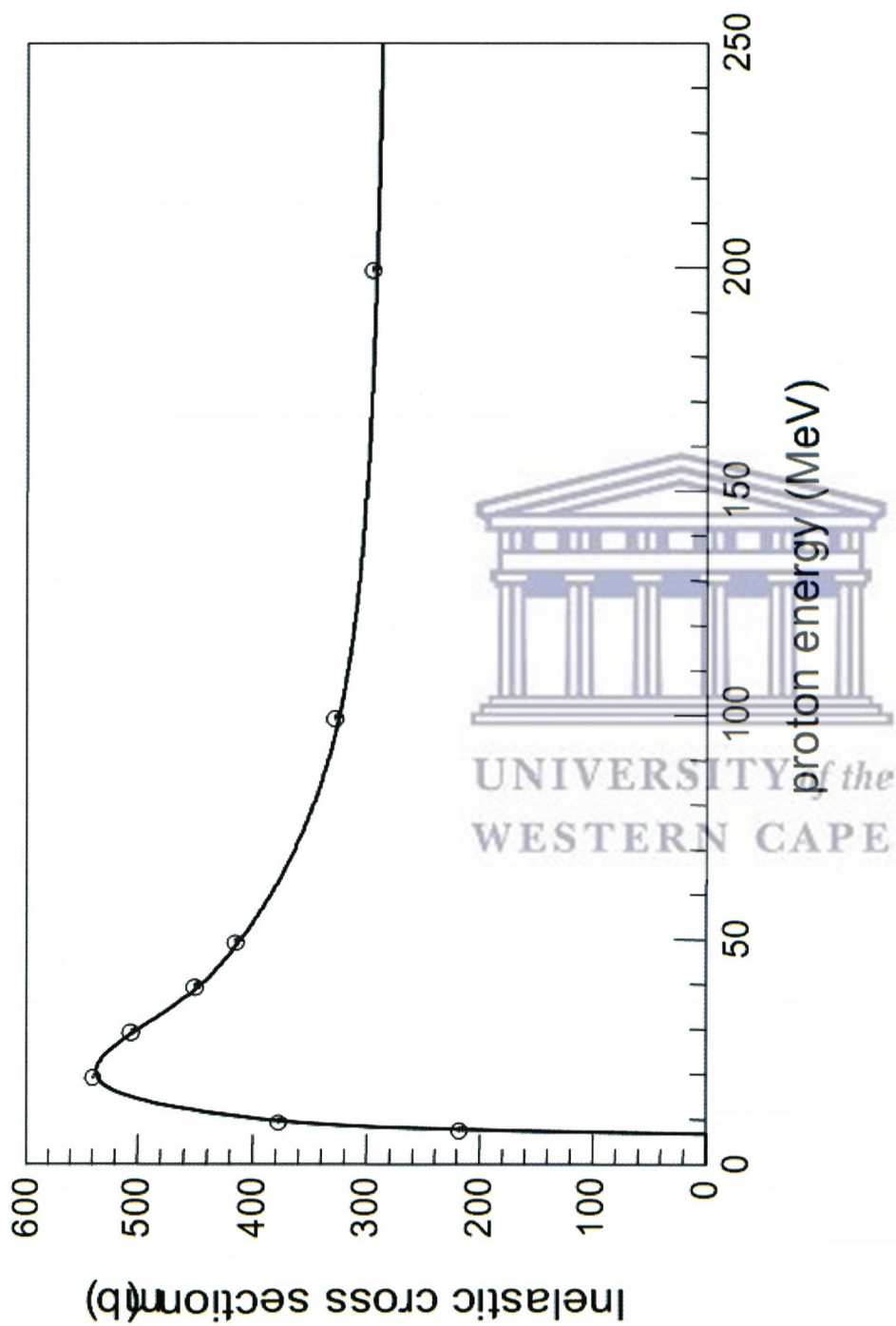


**Figure 4.3:** Total nonelastic nuclear cross section for protons incident on  $^{16}\text{O}$ . The line represents a fit using the GNASH- code [15] to the experimental data [1].

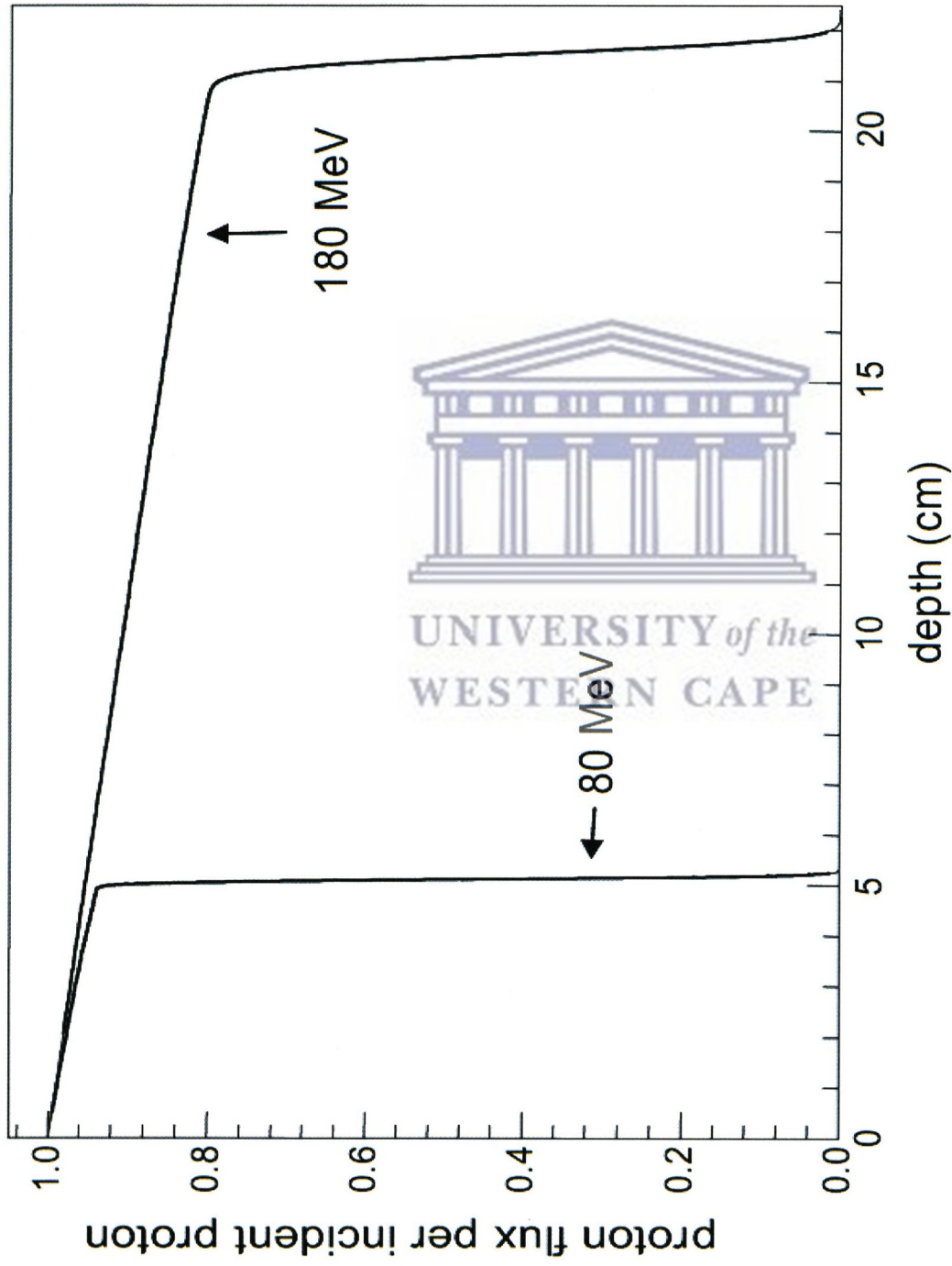


**Figure 4.4:** Proton flux reduction due to inelastic nuclear reactions for a 80 and a 180 MeV beam in a water medium calculated using equation (4.13) and the cross sections in figure 4.3 [1].

## **4.1.2 Interactions with neutrons**

This section provides fundamental information about neutron interactions that are important to nuclear material measurements; the first part of the section describes the interactions on the microscopic level where individual neutrons, interact with other particles and nuclei. The concepts are then extended to macroscopic interactions with bulk compound materials on the second section.

### **4.1.2.1 Microscopic interactions**

#### **4.1.2.1.1 The Cross-Section Concept**

The probability of a particular event occurring between a neutron and a nucleus is expressed through the concept of the cross section. If a large number of neutrons of the same energy are directed into a layer of material, some may pass through with no interaction, others may have interactions that change their directions and energies, and still others may fail to emerge from the sample. There is a probability for each of these events. For example, the probability of a neutron not emerging from a sample (that is, of being absorbed or captured) is the ratio of the number of neutrons that do not emerge to the number originally incident on the layer.

The cross section for being absorbed is the probability of neutrons being absorbed divided by the areal atom density (the number of target atoms Per unit area of the layer): the cross section thus has the dimensions of area it must be a small fraction of a square centimeter because of the large number of atoms involved.



Because this type of cross section, describes the probability of neutron interaction with a single nucleus, it is called the microscopic cross section and is given the symbol  $\sigma$  (A macroscopic cross section for use with bulk matter is defined in Section 4.1.2.2).

Another approach to understanding the concept of the microscopic cross section is to consider the probability of a single neutron attempting to pass through a layer of material that has an area  $A$  and contains  $N$  target nuclei, each of cross-sectional areas. The sum of all the areas of the nuclei is  $N_s$ . The probability of a single neutron hitting one of these nuclei is roughly the ratio of the total target area  $N_s$  to the area of the layer  $A$ .  $N_s/A$  or  $(N/A)_s$ , the areal target density times  $s$ . On the atomic level, however, cross sections for neutron interactions are not simply the geometrical cross-sectional area of the target. By replacing this  $s$  by the  $\sigma$  of the preceding paragraph, a might be thought of as an effective cross-sectional area for the interaction. The cross section for the interaction retains the dimensions of area that  $s$  had.

The physical cross-sectional area  $s$  of a heavy nucleus is about  $2 \times 10^{-24} \text{ cm}^2$ . Interaction cross sections for most nuclei are typically between  $10^{-27}$  and  $10^{-21} \text{ cm}^2$ . To avoid the inconvenience of working with such small numbers, a different unit of area is used the barn, denoted by the symbol  $b$ . It is defined to be  $10^{-24} \text{ cm}^2$ , so that the physical cross-sectional area of a heavy nucleus is about  $2b$ . Many neutron interaction cross sections range between  $0.001$  and  $1000b$ .

Each type of event has its own probability and cross section. The probability of each type of event is independent of the probabilities of the others, so the total probability of any event occurring is the sum of the individual probabilities. Similarly, the sum of all the individual cross sections is the total cross section.

#### 4.1.2.1.2 Types of Interactions

A neutron can have many types of interactions with a nucleus. Figure 4.5 shows the types of interactions and their cross sections. Each category of interaction in the figure 4.5 consists of all those linked below it. The total cross section  $\sigma_t$  expresses the probability of any interaction taking place. A simple notation can be used to give a concise indication of an interaction of interest. If a neutron  $n$  impinges on a target nucleus  $T$ , forming a resultant nucleus  $R$  and the release of an outgoing particle  $g$ , this interaction is shown as  $T(n,g)R$ . The heavy nuclei are shown outside the parentheses. To denote a type of interaction without regard for the nuclei involved, only the portion in parentheses is shown. An example of an  $(n,p)$  reaction is  ${}^5\text{B}(n,p){}^5\text{Be}$ .

An interaction may be one of two major types scattering or absorption. When a neutron is scattered by a nucleus, its speed and direction change but the nucleus is left with the same number of protons and neutrons it had before the interaction. The nucleus will have some recoil velocity and it may be left in an excited state that will lead to the eventual release of radiation. When a neutron is absorbed by a nucleus, a wide range of radiations can be emitted or fission can be induced.

Scattering events can be subdivided into elastic and inelastic scattering. In elastic scattering the total kinetic energy of the neutron and nucleus is unchanged by the interaction. During the interaction, a fraction of the neutron's kinetic energy is transferred to the nucleus. For a neutron of kinetic energy  $E$  encountering a nucleus of atomic weight  $A$ , the average energy loss is  $2EA/(A+1)^2$ . This expression shows that in order to reduce the speed of neutrons (that is, to moderate them) with the fewest number of elastic collisions target nuclei with small  $A$  should be used.

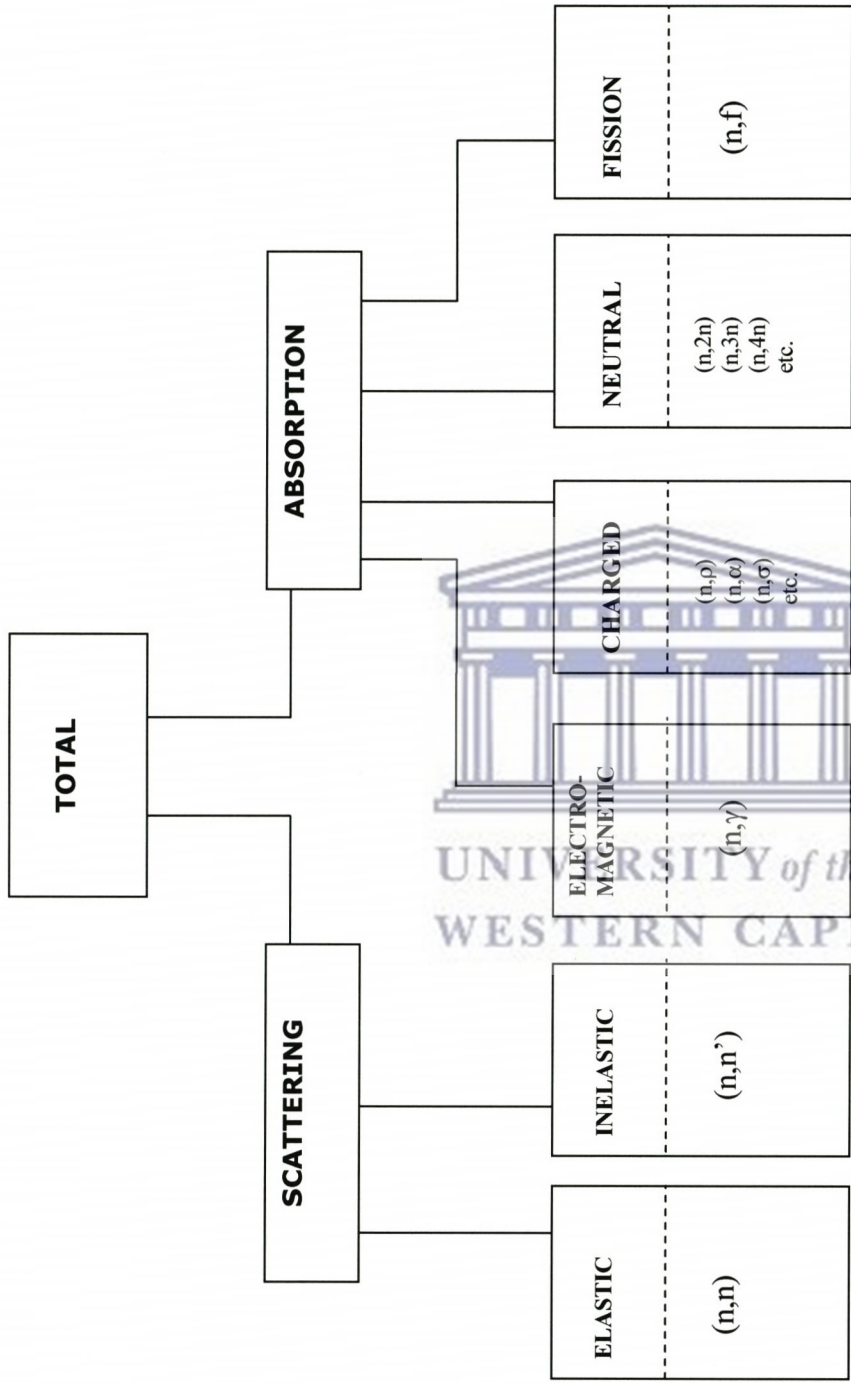
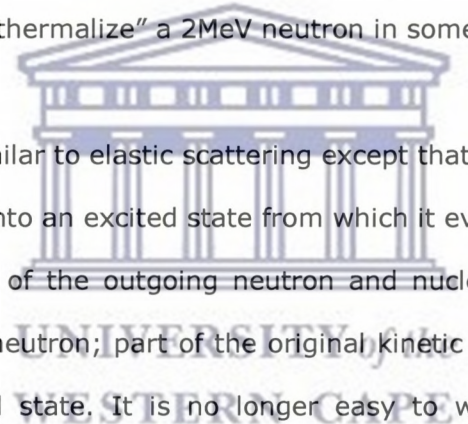


**Fig.4.5** various categories of neutron interactions. The letters separated by commas in the parentheses show the incoming and outgoing particles [2].

By using hydrogen, with  $A = 1$ , the average energy loss has its largest value of  $E/2$ . A neutron with 2 MeV of kinetic energy will (on the average) have 1 MeV left after one elastic collision with a hydrogen nucleus, 0.5 MeV after a second such collision, and so on. To achieve a kinetic energy of only 0.025 eV would take a total of about 27 such collisions. (A neutron of energy 0.025 eV is roughly in thermal equilibrium with its surrounding medium and is considered a "thermal neutron." From the relation  $E = KT$  where  $K$  is Boltzmann's constant, an energy  $E$  of 0.025 eV corresponds to a temperature  $T$  of 20°C.) In general, after  $n$  elastic collisions, the neutron's energy is expected to change from  $E_0$  to  $E_n = E_0[(A^2+1)/(A+1)^2]^n$ . To reach  $E_n$  from  $E_0$  thus requires  $n = \log[(A^2+1)/(A+1)^2]$  collisions, on the average. Table 4.1 gives examples of the number of collisions required to "thermalize" a 2MeV neutron in some materials.



Inelastic scattering is similar to elastic scattering except that the nucleus undergoes an internal rearrangement into an excited state from which it eventually releases radiation. The total kinetic energy of the outgoing neutron and nucleus is less than the kinetic energy of the incoming neutron; part of the original kinetic energy is used to place the nucleus into the excited state. It is no longer easy to write an expression for the average energy loss because it depends on the energy levels within the nucleus. But the net effect on the neutron is again to reduce its speed and change its direction. If all the excited states of the nucleus are too high in energy to be reached with the energy available from the incoming neutron, inelastic scattering is impossible. In particular, the hydrogen nucleus does not have excited states, so only elastic scattering can occur in that case. In general, scattering moderates or reduces the energy of neutrons and provides the basis for some neutron detectors (for example, proton recoil detectors).

<b>Element</b>	<b>Atomic of Weight</b>	<b>Number of Collisions</b>
Hydrogen	1	27
Deuterium	2	31
Helium	4	48
Beryllium	9	92
Carbon	12	119
Uranium	238	2175

**Table 4.1.** Average number of collisions required to reduce a neutron's energy from 2 MeV to 0.025 eV by elastic scattering [2].

Instead of being scattered by a nucleus, the neutron may be absorbed or captured. A variety of emissions may follow, as shown in Figure 4.6. The nucleus may rearrange its internal structure and release one or more gamma rays. Charged particles may also be emitted the more common ones are protons, deuterons, and alpha particles. The nucleus may also rid itself of excess neutrons. The emission of only one neutron is indistinguishable from a scattering event. If more than one neutron is emitted, the number of neutrons now moving through the material is larger than the number present before the interaction; the number is said to have been multiplied. Finally, there may be a fission event, leading to two or more fission fragments (nuclei of intermediate atomic weight) and more neutrons.

The cross sections associated with the various interactions described above can be designated by the following notation:

$\sigma_t$  = total cross section ( $\sigma_s + \sigma_a$ )

$\sigma_s$  = total scattering cross section ( $\sigma_{el} + \sigma_i$ )

$\sigma_{el}$  or  $\sigma_{n,n}$  = elastic scattering cross section

$\sigma_i$  or  $\sigma_{n,n'}$  = inelastic scattering cross section

$\sigma_a$  or  $\sigma_c$  = absorption or capture cross section

$\sigma_{ne}$  = nonelastic cross section,  $\sigma_t - \sigma_{el}$

$\sigma_{n,\gamma}$  = radiative capture cross section

$\sigma_f$  or  $\sigma_{n,f}$  = fission cross section

$\sigma_{n,p}$  = (n,p) reaction cross section.

All of the cross sections described above vary with neutron energy and with the target nucleus, sometimes in a dramatic way. Therefore on the following we give some generalizations about the energy dependence of cross sections and show data [16] for a few important nuclei.

Figure 4.5 is the total cross section for  $^{239}\text{Pu}$  for incident neutrons of 0.001eV to 10 MeV energy. Note that as a general rule the cross section decreases with increasing energy. At low energies, below 1 MeV, the elastic cross section is nearly constant, whereas the inelastic scattering cross section and absorption cross sections are proportional to the reciprocal of the neutron's speed (that is,  $1/v$ ). So at low energies the total cross section can be nearly constant or decreasing with energy, depending on which type of event dominates. For example, in  $^{239}\text{Pu}$  the inelastic cross section dominates and the total cross section decreases as  $1/v$ . Similar behavior is observed for most light and intermediate weight nuclei as well. Figures 4.6 and 4.7 illustrate the low-energy total cross-section behavior of boron and cadmium. The unusually high absorption cross sections of these two materials make them useful as thermal-neutron poisons.

At higher energies the cross section may have large peaks superimposed on the  $1/v$  trend. These peaks are called resonances and occur at neutron energies where reactions with nuclei are enhanced. For example, a resonance will occur if the target nucleus and

the captured neutron form a "compound" nucleus, and the energy contributed by the neutron is close to that of an excited state of the compound nucleus.

In heavy nuclei, large and narrow resonances appear for neutron energies in the eV range. For energies in the keV region the resonances can be too close together to resolve.

In the MeV region the resonances are more sparse and very broad, and the cross sections become smooth and rolling. For light nuclei, resonances appear only in the MeV region and are broad and relatively small. For nuclei with intermediate weights (such as cadmium, nickel, iron), resonances can be found below 1 keV. These resonances have heights and widths between those of light and heavy nuclei.

Some exceptions to the general trends exist in  $^1\text{H}$  and  $^2\text{H}$  where there are no resonances at all and in nuclei with "magic" numbers of protons or neutrons where the behavior may be similar to that of light nuclei despite the actual atomic weight. In practice, it is necessary to rely on tables of cross sections for the nuclei of interest because there is no convenient way to calculate cross sections.

Some neutron-induced fission cross sections important for nondestructive assay are shown in Figure 4.8. The fissile isotopes  $^{235}\text{U}$  and  $^{239}\text{Pu}$  have large cross sections (about 1000b) for fission by thermal or near-thermal neutrons. For fission by fast neutrons (10 keV to 10MeV), these cross sections are reduced to 1 to 2b. The fertile isotopes  $^{238}\text{U}$  and  $^{240}\text{Pu}$  have negligible fission cross sections for low-energy neutrons but exhibit a "threshold" near 1MeV neutron energy. Above 1 MeV the fission cross sections of the fertile isotopes are comparable to those of the fissile isotopes.

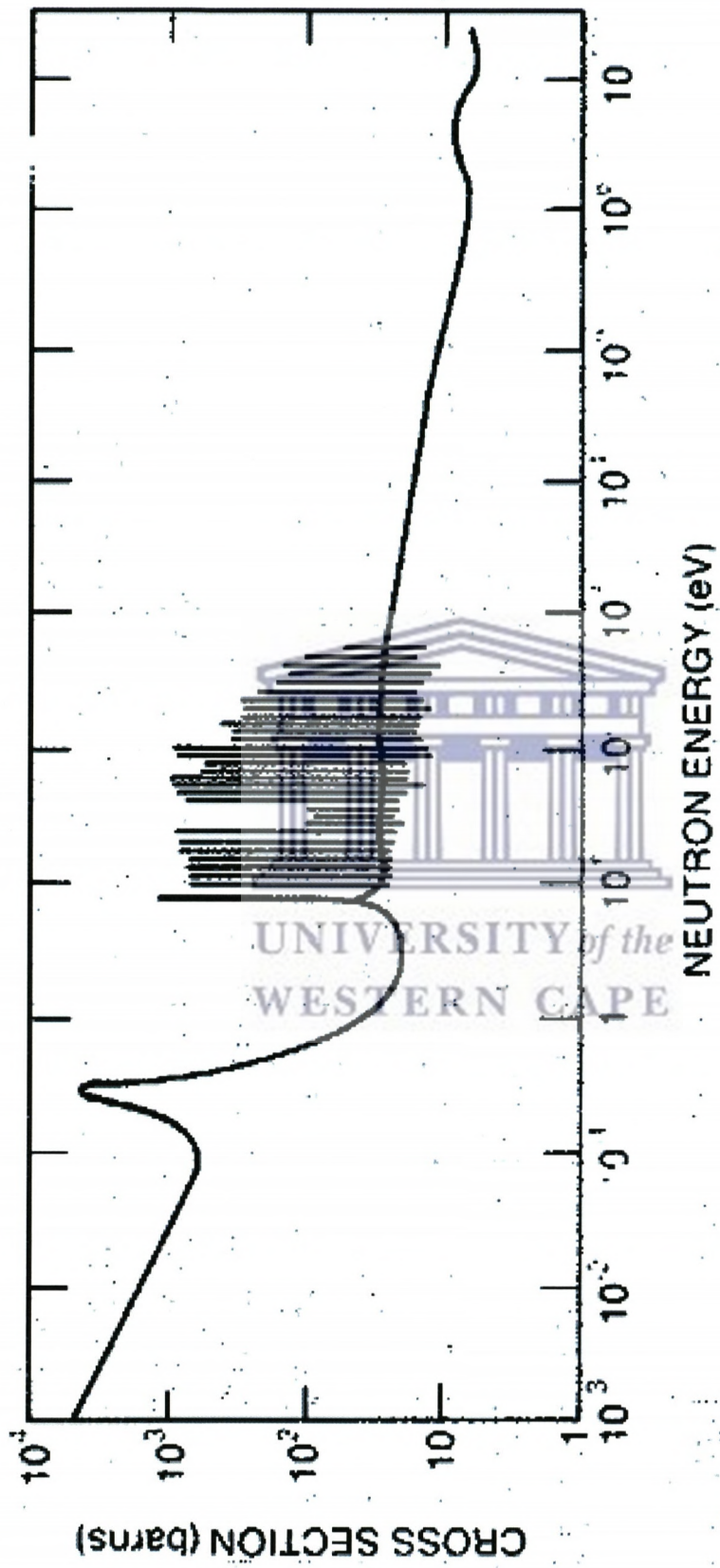
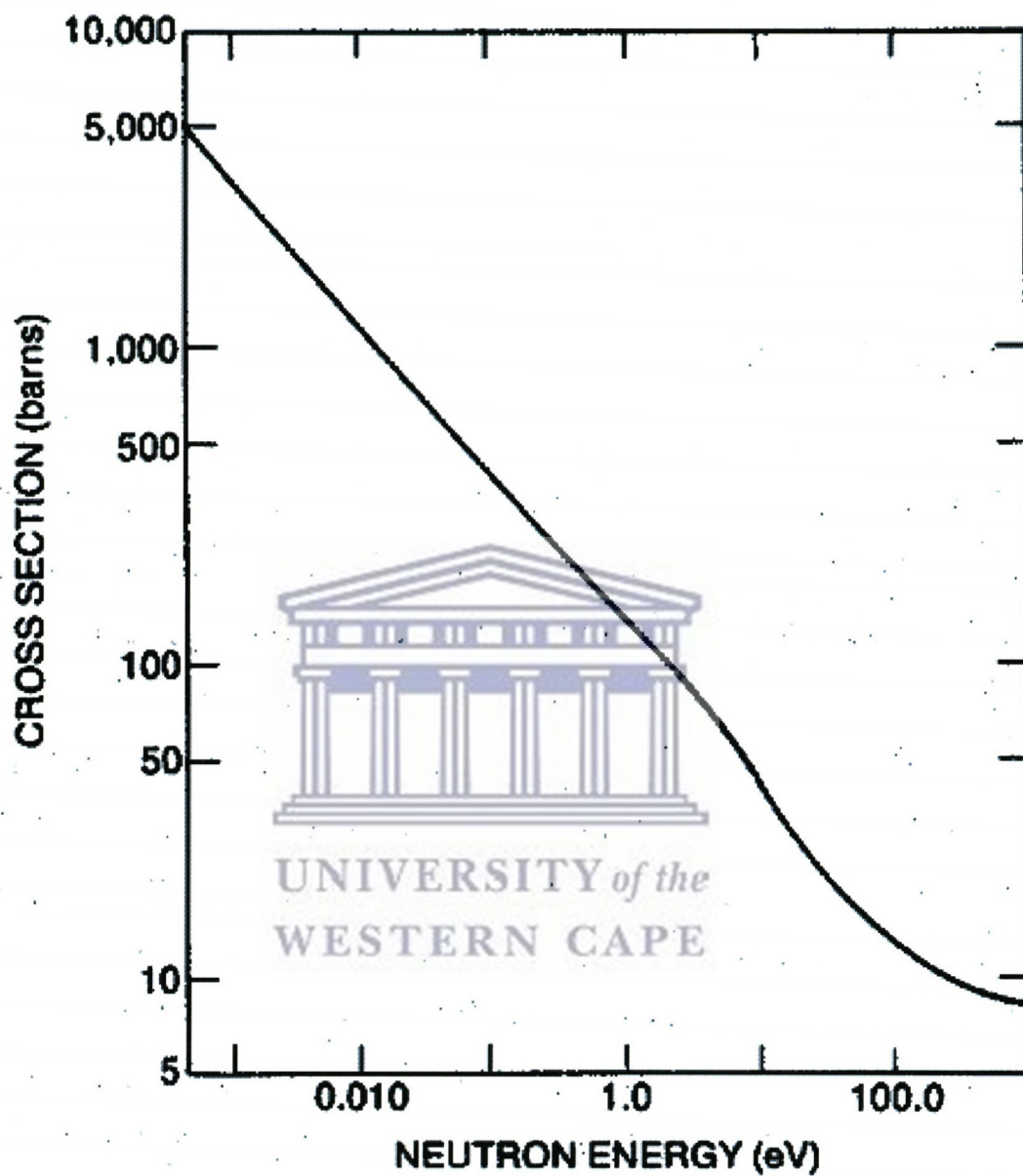
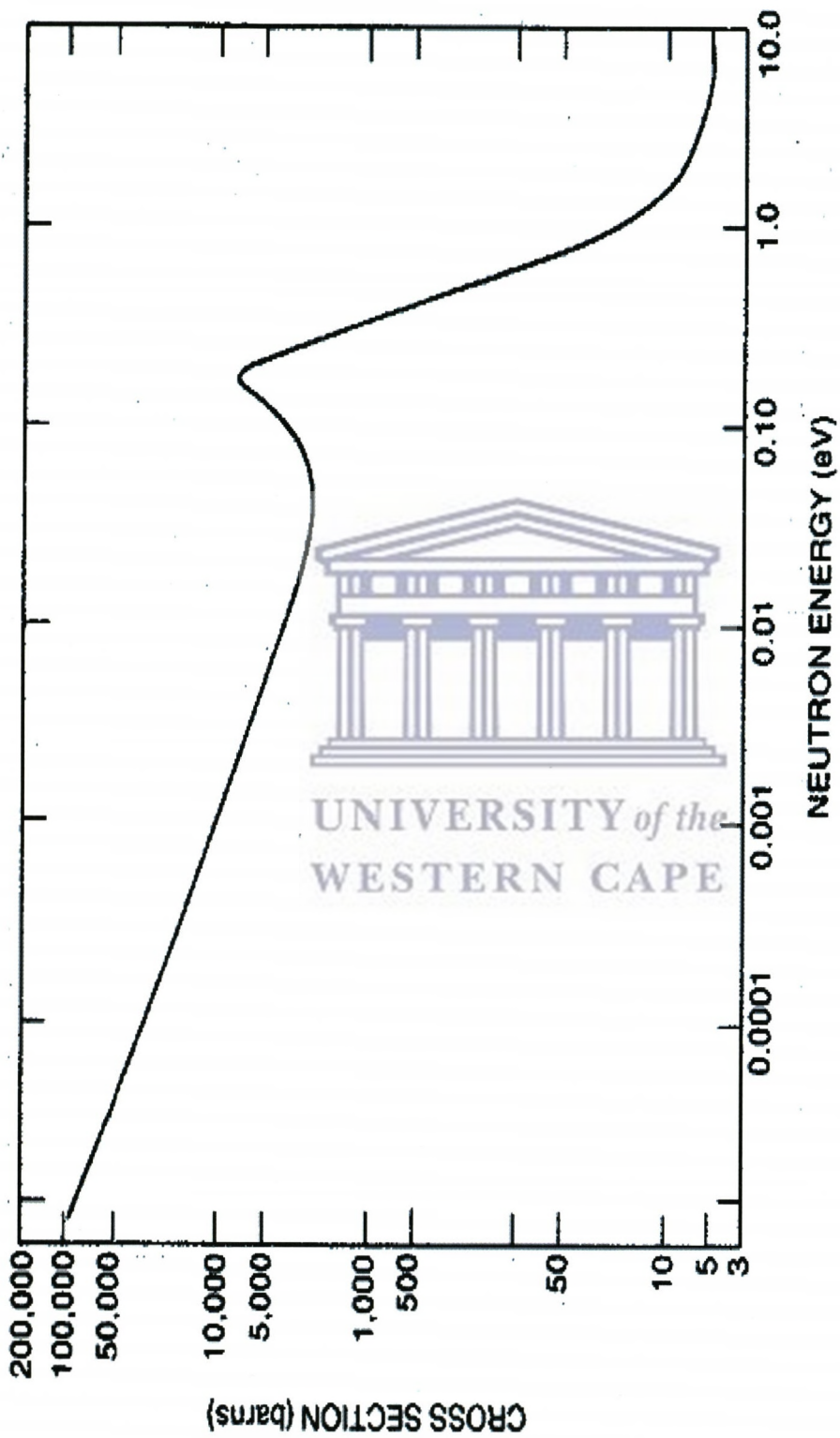


Fig.4.5: Total neutron cross section of  $^{239}\text{Pu}$  [2].





**Fig.4.6:** Low-energy total neutron cross section of boron [16]



**Fig.4.7:** Low-energy total neutron cross section of cadmium [16]

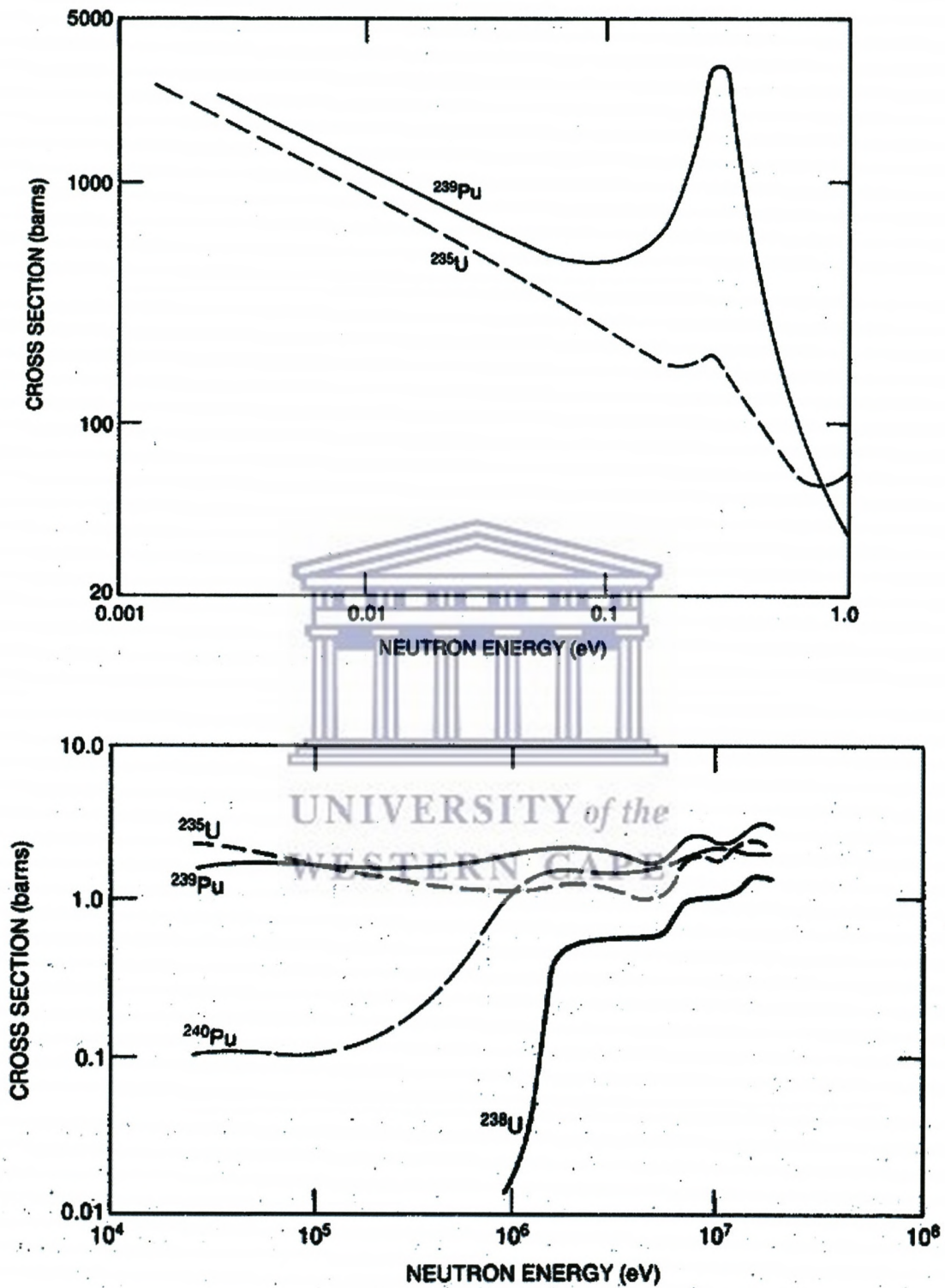


**Fig. 4.8:** Fission cross sections for some important fissile ( $^{235}\text{U}$ ,  $^{239}\text{Pu}$ ) And fertile ( $^{238}\text{U}$ ,  $^{240}\text{Pu}$ ) isotopes [16].

#### 4.1.2.2 Macroscopic interactions

##### 4.1.2.2.1 Macroscopic cross sections

Although study of the interactions of a neutron with a single nucleus on the microscopic scale provides a basis for understanding the interaction process, measurements are actually performed with thick samples that often contain a mixture of elements. These additional features are described by using the macroscopic cross sections appropriate for bulk materials.

The definition of the macroscopic cross section arises from the transmission of a parallel beam of neutrons through a thick sample. The thick sample can be considered to be a series of atomic layers for each layer we can apply the results found with the microscopic cross-section concept. By integrating through enough atomic layers to reach a depth  $x$  in the sample, the intensity  $I(x)$  of the uncollided neutron beam is

$$I(x) = I_0 e^{-N\sigma_t x} \quad (4-14)$$

where  $I_0$  is the intensity of the beam before it enters the sample,  $N$  is the atom density, and  $\sigma_t$  is the total cross section. Figure 4.9 shows the uncollided intensity remaining in a parallel beam as it passes through a thick layer of matter. Note that the fraction transmitted without collisions,  $I(x)/I_0$ , depends on the energy of the neutrons through the energy dependence of the microscopic total cross-section  $\sigma_t$ .

An expression similar to Equation 4.14 is used for gamma-ray attenuation. In that case, low energy gamma rays are very likely to be absorbed and thus removed not only from the parallel beam but from the material entirely. With neutrons at low energies, elastic scattering is the most likely event. Although Equation 4.14 gives the intensity of the neutrons that have had no interaction up to a depth  $x$ , the actual number of neutrons

present that can be detected may be much larger because of multiple scattering multiplication, or finite detector acceptance angle.

The total macroscopic cross section is  $\Sigma_t = N\sigma_t$ .  $\Sigma_t$  has dimensions of  $\text{cm}^{-1}$  (see Equation 4-14 above) and is analogous to the linear attenuation coefficient for gamma rays. If only a particular type of interaction is of interest, a macroscopic cross section for it alone can be defined using its microscopic cross section in place of the total cross section. For quantitative calculations, the concept of macroscopic cross section is less used than the analogous gamma-ray linear attenuation coefficient because of the complications of multiple scattering and other effects mentioned, in the previous

If the sample is a compound instead of a simple element, the total macroscopic cross section is the sum of the macroscopic cross sections of the individual elements:

$$\Sigma = \Sigma_1 + \Sigma_2 + \Sigma_3 \dots \quad (4.15)$$

The atom density  $N_i$  of each element  $i$  is given by

$$N_i = \rho N_a n_i / M \quad (4.16)$$

where  $\rho$  is the density of the compound,  $M$  is the molecular weight of the compound;  $N_a$  is Avogadro's number,  $6.022 \times 10^{23}$  atoms/mole, and  $n_i$  is the number of atoms of element  $i$  in one molecule. From Equations 4-15 and 4-16 the general form of the macroscopic cross section can be written as

$$\Sigma = \frac{\rho N_a}{M} (n_1 \sigma_1 + n_2 \sigma_2 + n_3 \sigma_3 \dots \Sigma \quad (4.17)$$

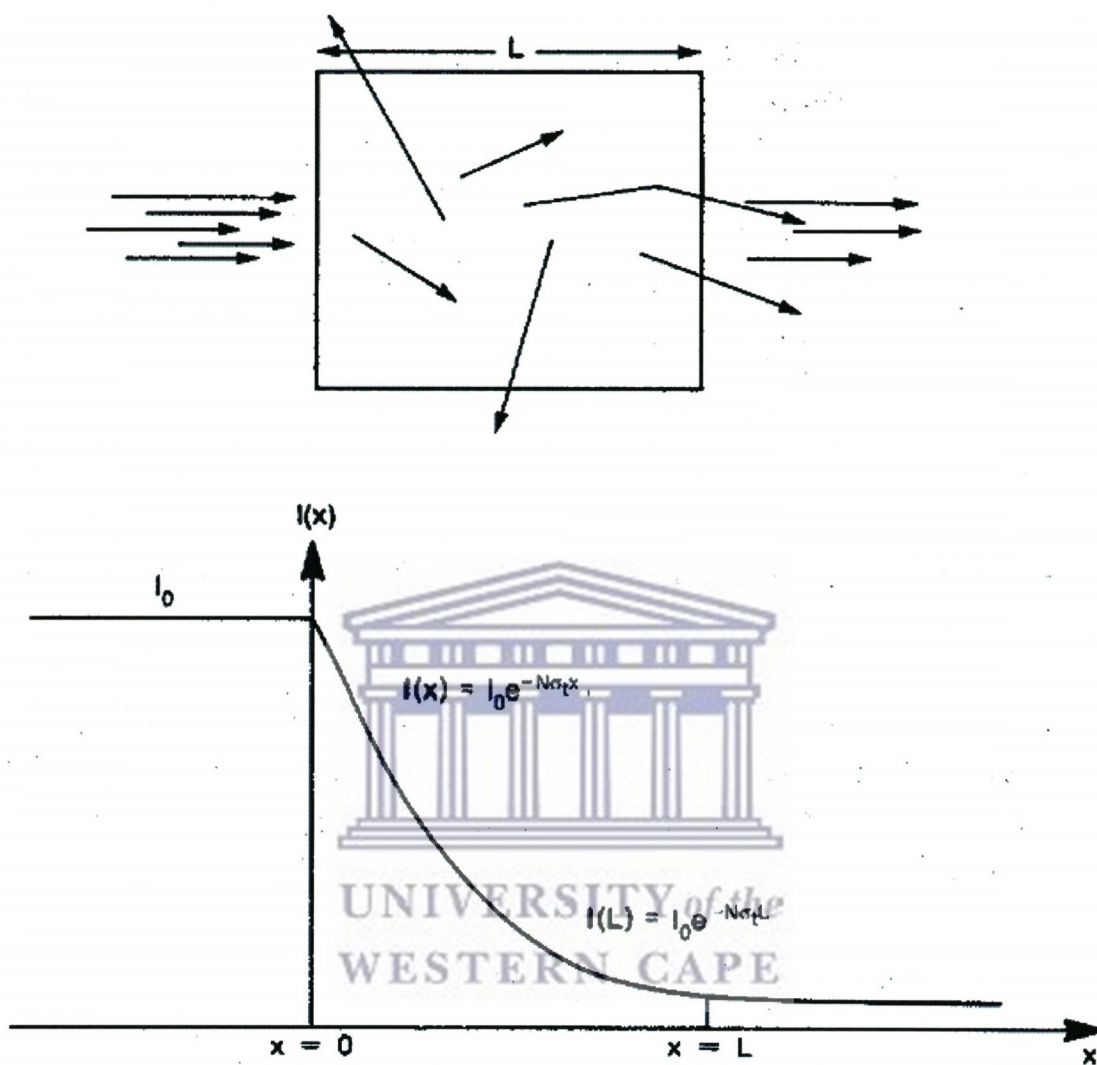


**Fig.4.9:** The intensity of a parallel beam of uncollided neutrons decreases exponentially as it passes through a thick layer of matter [2].

As an illustration of these equations, the total macroscopic cross section for 1-MeV neutrons in  $^{nat}\text{UO}_2$  (density  $10\text{g/cm}^3$ , molecular weight 270) is calculated from the data in Table 4-2.

Isotope	$n_i$	$\sigma_t$ at 1 MeV (b)
$^{235}\text{U}$	0.007	6.84
$^{238}\text{U}$	0.993	7.10
$^{16}\text{O}$	2.000	8.22

**Table 4.2:** Nuclear data for  $^{nat}\text{UO}_2$  [17]

$$\Sigma = \frac{(10)(0.6022)}{270} [(0.007)(6.84) + (0.993)(7.10) + 2(8.22)] = 0.525\text{cm}^{-1} \quad (4.18)$$

Powers of  $10^{24}$  and  $10^{-24}$  have been cancelled in Avogadro's number and in the cross section values. These cross-section values were taken from Table 4.3 [17], which is a compilation of microscopic and macroscopic cross sections at two neutron energies, 0.025 eV (thermal) and 1 MeV.

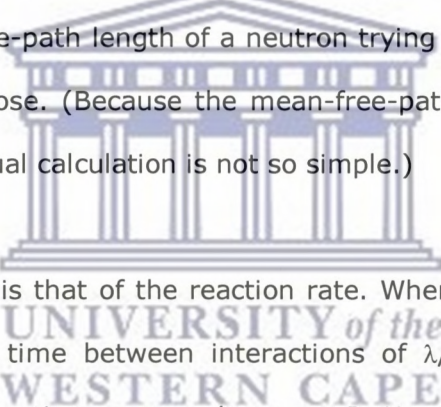
#### 4.1.2.2.2 Mean Free Path and Reaction Rate

A very descriptive feature of the transmission of neutrons through bulk matter is the mean-free-path length, which is the mean distance a neutron travels between interactions. It can be calculated from Equation 4.14 with  $N\sigma_t$  replaced by  $\Sigma_t$ . The mean-free path length  $\lambda$  is

$$\lambda = 1/\Sigma_t \quad (4-19)$$

the reciprocal of the macroscopic cross section. For the case of 1 MeV neutrons in UO<sub>2</sub> calculated above, a macroscopic cross section of 0.525 cm<sup>-1</sup> implies a mean-free-path length of 1.91cm.

The mean-free-path length has many qualitative applications in assay instruments and shielding. (a) If the mean-free-path length of neutrons emitted by a sample in a passive assay instrument is long compared to the dimensions of the sample, it is likely that most of the neutrons will escape from the sample and enter the detection region. (b) If the number of collisions required to thermalize a neutron is known, the necessary moderator thickness of a shield can be estimated. (c) If the thickness of a shield is many times the mean-free-path length of a neutron trying to penetrate the shield, then the shield fulfills its purpose. (Because the mean-free-path length is a function of the neutron's energy, the actual calculation is not so simple.)



A closely related concept is that of the reaction rate. When traveling with a speed  $v$ , a neutron has an average time between interactions of  $\lambda/v$ . The reaction rate is the frequency with which interactions occur:  $v/\lambda$ , or  $v\Sigma_t$ . In Uranium Oxide, for example, a 1 MeV neutron will have a reaction rate of  $7.26 \times 10^8$  per second (from Equations 4-18). This does not mean, however, that in one second there will be that many reactions with each collision the neutron's energy decreases and the cross section changes, thereby altering the instantaneous reaction rate.

The paths of neutrons in matter can be simulated with Monte Carlo calculations. Figure 4.10 shows a few paths for neutrons with 1 MeV of energy entering cylinders of different materials. The mean-free-path length depends on both the type of material and the energy of the neutron. After each collision, the energy is decreased and the mean free-



path length is affected accordingly. Figure 4.10 shows that a cylinder of polyethylene is more effective in preventing the transmission of neutrons than a cylinder of heavy metal. A neutron loses most of its energy by colliding with the light elements in polyethylene and then the mean-free-path length becomes small as the cross sections increase. An important effect of polyethylene is that it seemingly retains a large fraction of the neutrons near a certain depth; these neutrons have had enough collisions to lose nearly all their kinetic energy. If a thermal-neutron detector is placed in this region, the chance of detecting neutrons is optimized.

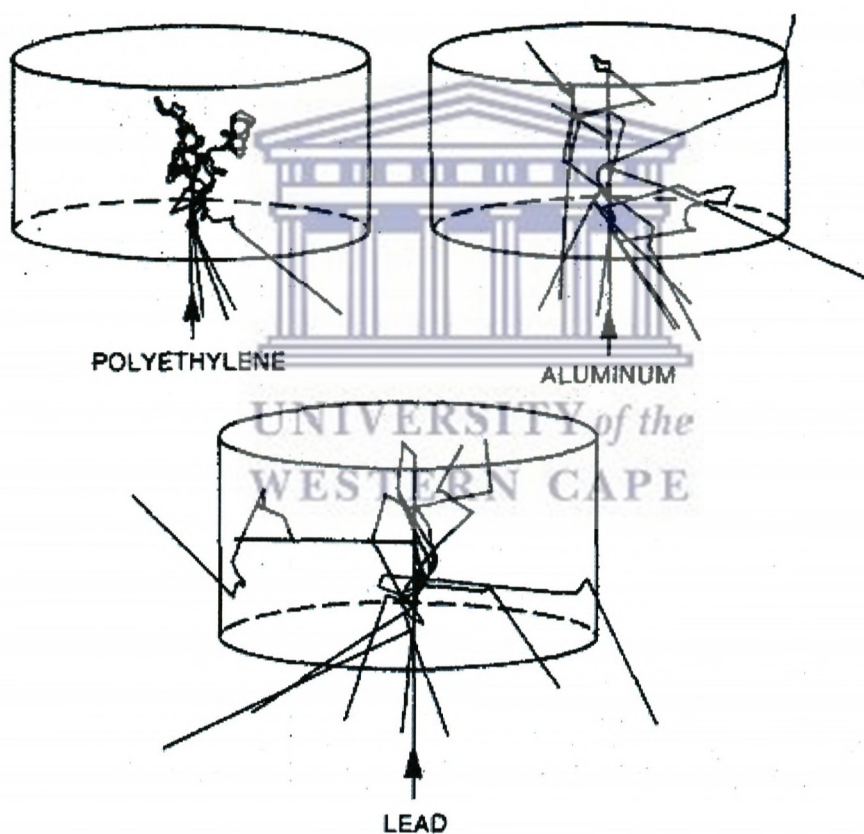


**Fig.4.10:** Neutrons with 1 MeV of kinetic energy are shown Entering cylinders of material from the bottom and then being scattering or absorbed. The paths were calculated using a Monte Carlo technique.

#### 4.1.2.3 Effects of moderation in bulk matter

It is often a design goal to reduce or moderate the speed of neutrons in the sample region or the detector region or both. Recalling the general  $1/v$  trend of interaction cross sections (Figures 4.5 through 4.8), the purpose of the reduction in speeds is to increase the probability of an interaction. In other regions, it may be desirable to hinder interactions by choosing materials that are poor moderators or by adding low-energy neutron absorbers to remove neutrons once they become moderated.

For example, in the assay of plutonium, moderation is not a desirable effect in the sample region. High-speed neutrons are more able to penetrate the sample and they have lower fission cross sections so that multiplication is less than with low-speed neutrons. On the other hand, in the detector region, moderation increases the detection efficiency for detectors such as  $^3\text{He}$  proportional counters. By placing hydrogenous material (such as polyethylene) around the detectors, the neutrons can be counted with more efficiency. Also needed is a filter that will let high-speed neutrons enter the detector region where they can become moderated but will not let the moderated neutrons return to the sample region where they could produce additional fissions. A layer of material with a large absorption cross section for slow neutrons (such as cadmium, Figure 4.7) placed between the sample region and the detector region is effective in this regard.

A standard basis for comparing moderating abilities of different materials is the moderating power. If one material has a larger moderating power than another, less of that material is needed to achieve the same degree of moderation. Two factors are important (1) the probability of a scattering interaction and (2) the average change in kinetic energy of the neutron after such an interaction.

Cross Section <sup>b</sup>										
Material	Atomic or Molecular Weight	Density(g/cm <sup>3</sup> )	E = 0.0253 eV				E = 0.0253 eV			
			$\sigma_{t(b)}$	$\sigma_{a(b)}$	$\Sigma_t$ (cm <sup>-1</sup> )	$\Sigma_a$ (cm <sup>-1</sup> )	$\sigma_{t(b)}$	$\sigma_{a(b)}$	$\Sigma_t$ (cm <sup>-1</sup> )	$\Sigma_a$ (cm <sup>-1</sup> )
<b>Al</b>	27	2.7	1.6	0.232	0.097	0.014	2.37	0.000	0.143	0.0000
<b>B</b>	10	2.3	3845	533	532	532	2.68	0.189	0.371	0.0262
<b>B</b>	11	2.3	5.28	0.005	0.665	0.0006	2.13	0.000	0.268	0.000
<b>Be</b>	9	9.0	6.35	0.010	3.82	0.0060	3.25	0.003	1.96	0.0018
<b>C</b>	12	1.9	4.95	0.003	0.472	0.003	2.58	0.000	0.246	0.000
<b>Nat Ca</b>	40.08	1.55	3.46	0.433	0.081	0.101	1.14	0.004	0.027	0.0001
<b>Cd</b>	112	8.7	2470	2462	115.5	115.2	6.50	0.058	0.304	0.0027
<b>Nat Cl</b>	35.45	Gas	50.2	33.4	Gas	Gas	2.30	0.0005	Gas	Gas
<b>Nat Cu</b>	63.55	8.94	12.5	3.80	1.06	0.322	3.40	0.011	0.288	0.0009
<b>F</b>	19	Gas	3.72	0.010	Gas	Gas	3.15	0.000	Gas	Gas
<b>Fe</b>	56	7.9	14.07	2.56	1.19	0.217	5.19	0.003	0.441	0.0003
<b>Nat Gd</b>	157.25	7.95	49 153	48 981	1496	1491	7.33	0.223	0.223	0.0068
<b>H</b>	1	Gas	30.62	0.33	Gas	Gas	4.26	0.000	Gas	Gas
<b>H</b>	2	Gas	4.25	0.000	Gas	Gas	2.87	0.879	Gas	Gas
<b>He</b>	3	Gas	5337	5336	Gas	Gas	2.87	0.879	Gas	Gas
<b>He</b>	4	Gas	0.86	0.000	Gas	Gas	7.08	0.000	Gas	Gas
<b>Li</b>	6	0.534	938	937	50.3	50.2	1.28	0.230	0.069	0.0123
<b>Li</b>	7	0.534	1.16	0.036	0.053	0.0017	1.57	0.000	0.072	0.0000
<b>Nat Mg</b>	24.31	1.74	3.47	0.063	0.150	0.0027	2.66	0.001	0.115	0.0000
<b>Mn</b>	55	7.2	14.5	13.2	1.14	1.04	3.17	0.003	0.250	0.0002
<b>N</b>	14	Gas	12.22	1.9	Gas	Gas	2.39	0.021	Gas	Gas
<b>Na</b>	23	0.971	3.92	0.529	0.100	0.0134	3.17	0.000	0.081	0.0000
<b>Ni</b>	59	8.9	23.08	4.58	2.10	0.416	3.66	0.0008	0.322	0.0001
<b>O</b>	16	Gas	3.87	0.000	Gas	Gas	8.22	0.000	Gas	Gas
<b>Pb</b>	204	11.34	11.40	0.18	0.381	0.0060	4.39	0.0033	0.147	0.0001
<b>Pu</b>	238.05	19.6	599.3	562.0	29.72	27.87	6.66	0.190	0.330	0.0094
<b>Pu</b>	239.05	19.6	1021	270	50.4	13.3	7.01	0.026	0.346	0.0013
<b>Pu</b>	240.05	19.6	294	293	14.5	14.4	7.15	0.108	0.352	0.0053
<b>Pu</b>	241.06	19.6	1390	362	68.1	17.7	7.98	0.117	0.391	0.0057
<b>Pu</b>	242.06	19.6	26.7	18.9	1.30	0.992	7.31	0.098	0.357	0.0048

<b>Nat Si</b>	28.09	2.42	2.24	0.161	0.116	0.884	4.43	0.001	0.230	0.0001
<b>Th</b>	232	11.3	20.4	7.50	0.598	0.220	7.00	0.135	0.205	0.0040
<b>U</b>	233.04	19.1	587	45.8	29.0	2.26	6.78	0.069	0.335	0.0034
<b>U</b>	234.04	19.1	116	103	5.70	5.07	8.02	0.363	0.394	0.0178
<b>U</b>	235.05	19.1	703	96.9	34.3	4.74	6.84	0.117	0.335	0.0057
<b>U</b>	236.05	19.1	13.3	5.16	0.648	0.251	7.73	0.363	0.377	0.0177
<b>U</b>	237.05	19.1	487.5	476.4	23.6	23.1	6.72	0.135	0.326	0.0066
<b>U</b>	238.05	19.1	11.63	2.71	0.562	0.131	7.10	0.123	0.343	0.0059
<b>Nat U</b>	238.03	19.1	16.49	3.39	0.797	0.1637	7.01	0.120	0.343	0.0058
<b>Nat W</b>	183.85	19.3	23.08	18.05	1.459	1.141	6.95	0.057	0.439	0.0036
<b>CH<sub>2</sub></b>	14	0.94			2.68	0.027			0.449	0.0000
<b>H<sub>2</sub>O</b>	18	1.0			2.18	0.022			0.560	0.0000
<b>D<sub>2</sub>O</b>	20	1.1			0.410	0.000			0.420	0.0000
<b>Average Fission Products of:</b>										
<b><sup>235</sup>U</b>	117		4496	4486			7.43	0.00036		
<b><sup>239</sup>Pu</b>	119		2087	2086			7.48	0.00093		

**Table 4.3:** Neutron cross sections of common materials.

To be an effective moderator, both the probability of an interaction and the average energy loss in one scatter should be high. The moderating power is defined as  $\xi\Sigma_s$  where,  $\Sigma_s$  is the macroscopic scattering cross section and  $\xi$  is the average logarithmic energy decrement in a scatter. This decrement is  $\ln(E_{\text{before}}) - \ln(E_{\text{after}})$ . When elastic collisions in an element with atomic weight  $A$  dominate the scattering process, the decrement becomes

$$\xi = 1 - \frac{(A-1)^2}{2A} \ln \frac{(A+1)}{(A-1)} \quad (4.20)$$

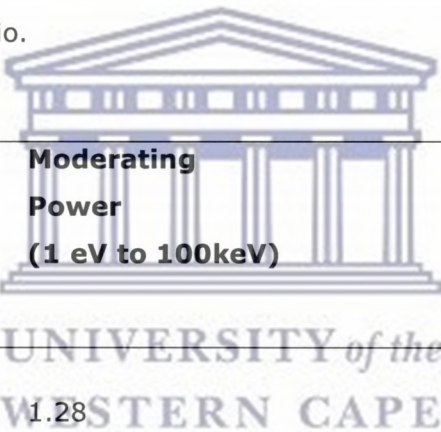
For  $A > 2$ ,  $\xi$  can be approximated by  $2/(A+0.67)$  [18]. The moderating power of a compound is given by

$$\xi \Sigma = \frac{\rho N_a}{M} (n_1 \sigma_1 \xi_1 + n_2 \sigma_2 \xi_2 + n_3 \sigma_3 \xi_3 \dots) \quad (4.21)$$

where  $\rho$  is the density of the compound,  $M$  is its molecular weight,  $N_a$  is Avogadro's number,  $n_i$  is the number of atoms of element  $i$  in one molecule,  $\xi_i$  is the microscopic scattering cross section for element  $i$ , and  $\xi_i$  is the logarithmic energy decrement for element  $i$ .

A material with a large moderating power might nevertheless be useless as a practical moderator if it has a large absorption cross section. Such a moderator would effectively reduce the speeds of those neutrons that are not absorbed, but the fraction of neutrons that survive may be too small to be used in a practical manner. A more comprehensive measure of moderating materials is the moderating ratio,  $\xi\Sigma_s/\Sigma_a$ . A large moderating ratio is desirable; it implies not only a good moderator but also a poor absorber. For a compound, the moderating ratio is given by Equation 4.21 with each  $\sigma_i$  replaced by  $\sigma_s/\sigma_a$  for element  $i$ .

Table 4.4 gives the moderating powers and ratios for some common moderator materials for neutrons in the 1eV to 100keV energy range [19]. Ordinary water has a higher moderating power than heavy water because the atomic weight of hydrogen is half that of deuterium. But the hydrogen nucleus (a proton) can absorb a neutron and create deuterium much more readily than a deuterium nucleus can absorb a neutron and create tritium. This difference in absorption cross sections gives heavy water a much more favorable moderating ratio. However, because of its availability and low cost, ordinary water is often preferred. The solid materials given in the table have a higher moderating ratio than ordinary water and can have fabrication advantages. Polyethylene is commonly selected as a moderator because of its high moderating power and moderating ratio.



<b>Moderator</b>	<b>Moderating Power (1 eV to 100keV)</b>	<b>Moderating Ratio (Approximate)</b>
Water	1.28	58
Heavy Water	0.18	21000
Helium at STP	0.00001	45
Beryllium	0.16	130
Graphite	0.064	200
Polyethylene (CH <sub>2</sub> )	3.26	122

**Table 4.4.** Moderating powers and ratios of selected materials [19].

#### 4.1.2.4 Effects of multiplication in bulk matter

When a neutron interaction yields more than one neutron as a product, a multiplication event has occurred. More neutrons will be present in the material after the interaction than before. The most widely known multiplication event is fission, but other absorption interactions, such as  $(n,2n)$ , can be important contributors to multiplication.

Of the neutrons in a given material at a given moment, some will eventually escape and the others will be absorbed. Additional neutrons can originate in the material as products of the absorption. The definition of the multiplication  $M$  is the total number of neutrons that exist in the sample divided by the number of neutrons that were started.

If 100 neutrons are started in the sample and an additional 59 are found to be created from multiplication events, the multiplication is 1.59. Only a fraction of the first generation of 100 neutrons produces additional neutrons through multiplication event the others escape or are absorbed by other types of interactions. The same fraction of the second generation produces a third generation, and so on. The number of neutrons remaining in the sample steadily decreases until it is zero and the total number of neutrons produced by all the multiplication events is 59.

A related concept that is more commonly used is, the multiplication factor. It relates the numbers of neutrons in successive generations. There are two categories of multiplication factors that apply to different physical sizes of the material involved. If the material is infinite in extent, the multiplication factor is written  $k_{\infty}$  and is defined as the ratio of the number of neutrons in one generation to the number in the previous generation. Because of the infinite size of the material, all neutrons of a generation

become absorbed. Thus  $K_{\infty}$  is also the fraction of the number of neutrons produced in one generation to the number absorbed in the preceding generation.

If the material is not infinite in size, some neutrons in a generation may escape through the surface and not be absorbed these are 'leakage' neutrons. The multiplication factor for this more practical situation is called  $K_{\text{eff}}$ . It is defined as the ratio of the number of neutrons produced in one generation to the number either absorbed or leaked in the preceding generation. The multiplication factor  $\sim$  is the more practical ratio for safeguards work because instruments are often made small to comply with size and weight constraints.

As an example of  $K_{\text{eff}}$  and its connection with the multiplication  $M$ , consider the case described earlier. The original 100 neutrons would constitute the first generation. If the original neutrons create 37 neutrons through reactions, the 37 neutrons would be the next generation. The multiplication factor in this case is thus 0.37. With  $K_{\text{eff}}$  less than one, the number of neutrons in succeeding generations decreases, eventually reaches zero. As Table 4.5 indicates, it takes 7 generations to reduce the number of neutrons from 100 to about zero.

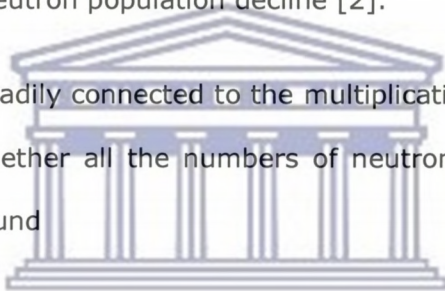
The number of neutrons in one generation is found by multiplying the number in the previous generation by the multiplication factor  $K_{\text{eff}}$ , which in this example is 0.37. This is a statistical process, of course, and the exact number in any generation cannot be exactly known, but for large numbers of neutrons the ratio of populations in successive generations is very nearly constant.



Generation	Average No. of Neutrons for $K_{eff} = 0.37$
1	100
2	37
3	14
4	5
5	2
6	1
7	0
	159

**Table 4.5.** Example of neutron population decline [2].

The multiplication  $M$  is readily connected to the multiplication factor  $K_{eff}$  when  $K_{eff}$  is less than one. By adding together all the numbers of neutrons in all the generations, the geometric sum can be found



$$M = 1/(1-K_{eff}), K_{eff} < 1 \quad (4.22)$$

UNIVERSITY of the  
WESTERN CAPE

With the multiplication of 1.59 in Table 4-5, the multiplication factor is 0.37, showing that the number of neutrons is decreasing in successive generations.

As  $K_{eff}$  approaches one, the value of  $M$  becomes huger and larger, as shown in Figure 12.9. When  $K_{eff} = 1$ , the formula shows that there is no limit to the number of neutrons that will be produced; in practice, there is a finite number of nuclei that can produce neutrons, so the number of neutrons created is finite but extremely large. Criticality is said to be reached when  $K_{eff} = 1$ . If  $K_{eff}$  is larger than one, the sample is supercritical; with  $K_{eff}$  less than one, the sample is subcritical.

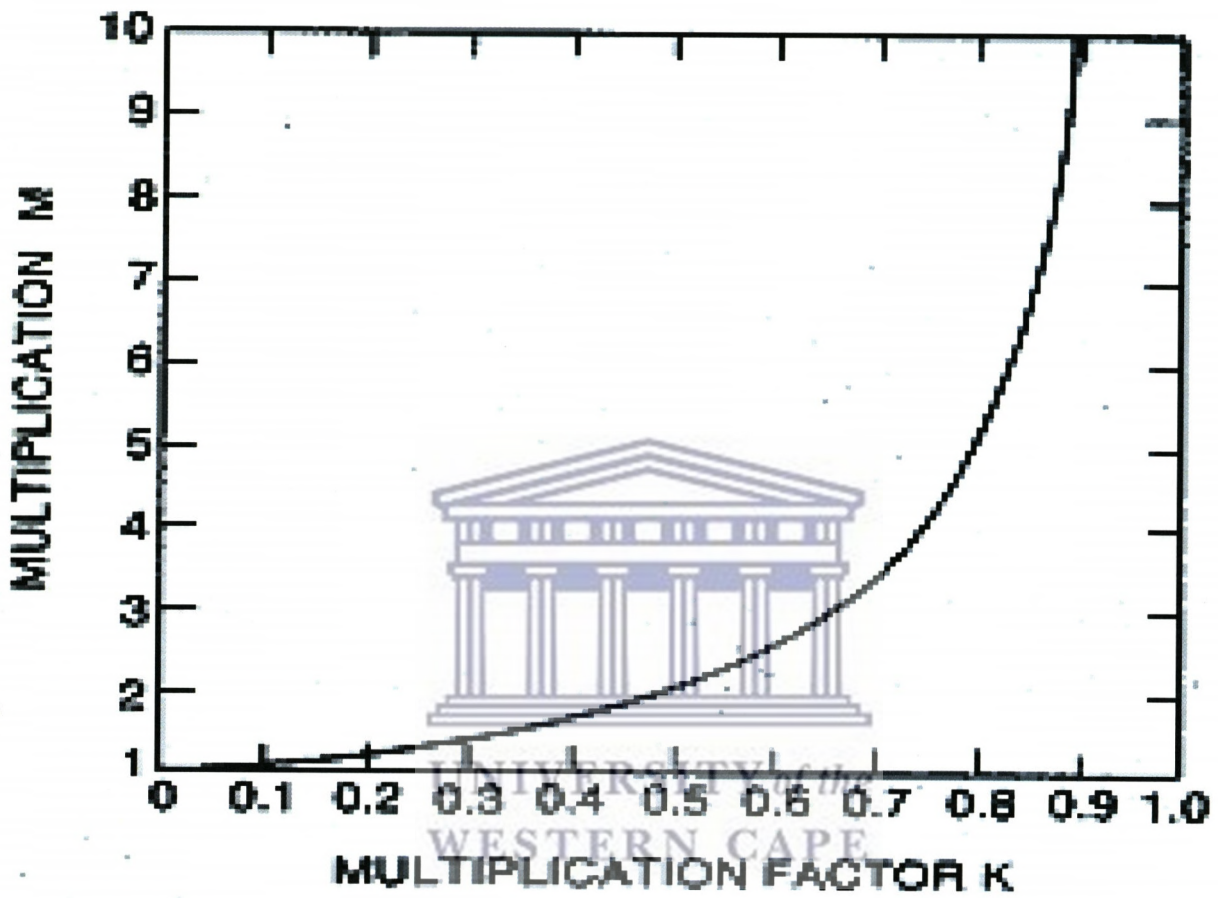


**Fig.4.11** The multiplication  $M$  is shown as a function of the multiplication factor  $K_{\text{eff}}$ . Only subcritical values ( $K_{\text{eff}}$  less than one) are included here [2].

### **4.1.3 Interactions with $\gamma$ -ray**

The gamma rays interact with matter by three major processes: photoelectric absorption, Compton scattering, and pair production. In the photoelectric absorption process, the gamma ray loses all of its energy in one interaction. The probability for this process depends very strongly on gamma-ray energy  $E_\gamma$  and atomic number  $Z$ . In Compton scattering, the gamma ray loses only part of its energy in one interaction. The probability for this process is weakly dependent on  $E$  and  $Z$ . The gamma ray can lose all of its energy in one pair-production interaction. However, this process is relatively unimportant for fissile material assay since it has a threshold above 1 MeV. Reference [3] is recommended for more detailed physical descriptions of the interaction processes.

#### **4.1.3.1 Photoelectric Absorption**

A gamma-ray may interact with a bound atomic electron in such a way that it loses all of its energy and ceases to exist as a gamma ray (see Figure 4.12). Some of the gamma-ray energy is used to overcome the electron binding energy, and most of the remainder is transferred to the freed electron as kinetic energy. A very small amount of recoil energy remains with the atom to conserve momentum. This is called photoelectric absorption because it is the gamma-ray analog of the process discovered by Hertz in 1887 whereby photons of visible light liberate electrons from a metal surface. Photoelectric absorption is important for gamma-ray and matter interactions because the gamma ray gives up all its energy, and the resulting pulse falls in the full-energy peak.

The probability of photoelectric absorption depends on the gamma-ray energy, the electron binding energy, and the atomic number of the atom. The probability is greater the more tightly bound the electron; therefore, K electrons are most affected (over 80% of the interactions involve K electrons), provided the gamma-ray energy exceeds the K-

electron binding energy. The probability is given approximately by Equation 4.23, which shows that the interaction is more important for heavy atoms like lead and uranium and low-energy gamma rays:

$$\tau \propto ZE \quad (4.23),$$

where  $\tau$  is the photoelectric, mass attenuation coefficient.

This proportionality is only approximate because the exponent of  $Z$  varies in the range 4.0 to 4.8. As the gamma-ray energy decreases, the probability of photoelectric absorption increases rapidly. Photoelectric absorption is the predominant interaction for low-energy gamma rays, x-rays, and bremsstrahlung.

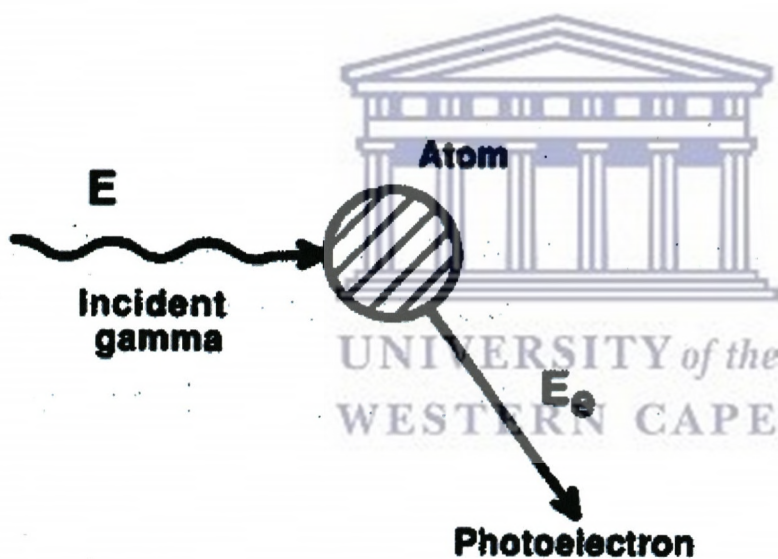
The energy of the photoelectron  $E_e$  released by the interaction is the difference between the gamma-ray energy  $E_\gamma$  and the electron binding energy  $E_b$ :

$$E_e = E_\gamma - E_b \quad (4.24)$$

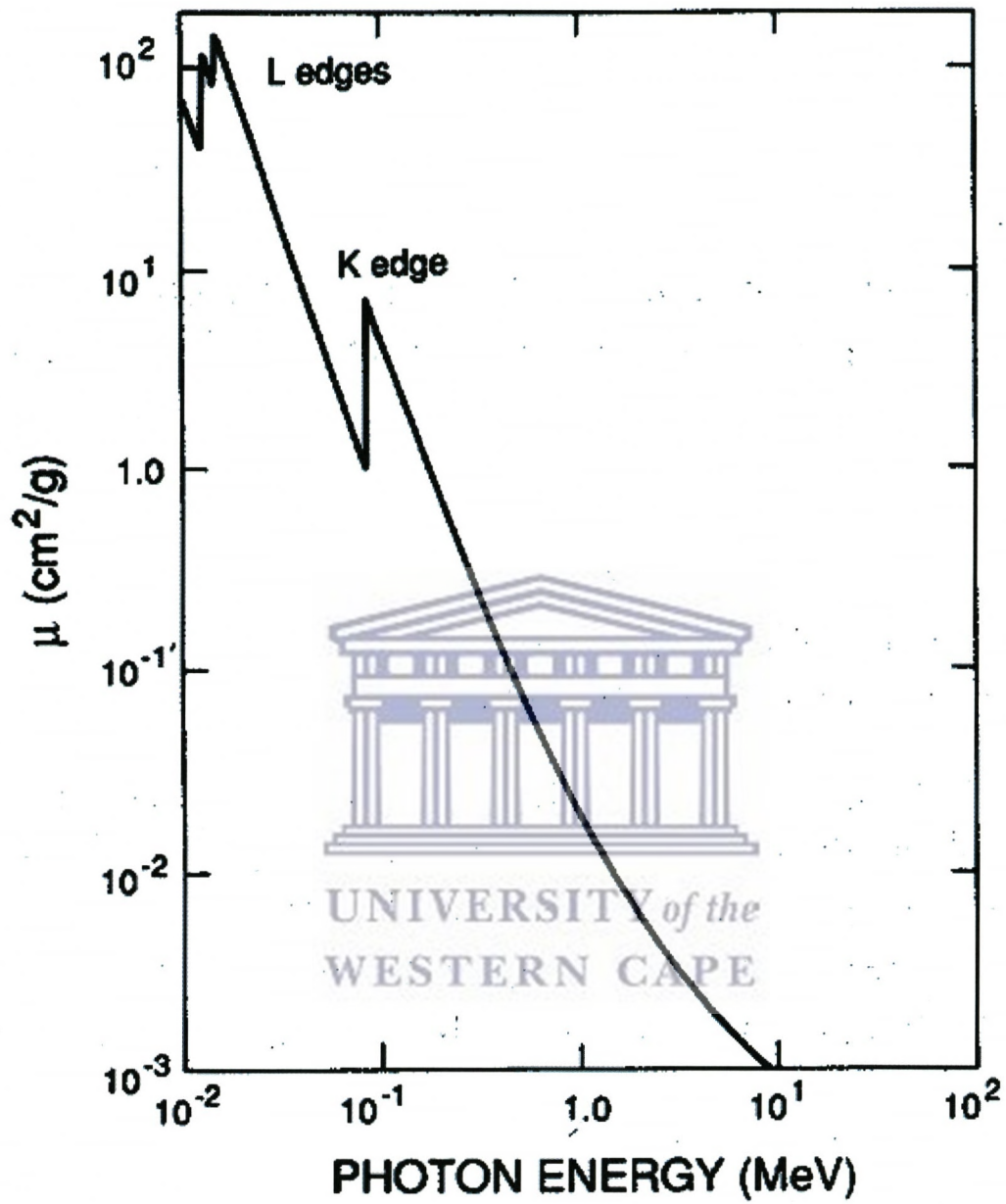
In mostly, the photoelectron is stopped quickly in the active volume of the matter, which emits a small output pulse whose amplitude is proportional to the energy deposited by the photoelectron. The electron binding energy is not lost but appears as characteristic x-rays emitted in coincidence with the photoelectron. In most cases, these x-rays are absorbed in the matter in coincidence with the photoelectron and the resulting output pulse is proportional to the total energy of the incident gamma-ray. For low-energy gamma-rays in very small  $Z$ , a sufficient number of K x-rays can escape from the matter to cause escape peaks in the observed spectrum; the peaks appear below the full-energy peak by an amount equal to the energy of the x-ray.

Figure 4.13 shows the photoelectric mass attenuation coefficient of lead. The interaction probability increases rapidly as energy decreases, but then becomes much smaller at a

gamma-ray energy just below the binding energy of the K electron. This discontinuity is called the K edge below this energy the gamma-ray does not have sufficient energy to dislodge a K electron. Below the K edge the interaction probability increases again until the energy drops below the binding energies of the L electron; these discontinuities are called the  $L_I$ ,  $L_{II}$ , and  $L_{III}$  edges. The presence of these absorption edges is important for densitometry and x-ray fluorescence measurements.



**Fig. 4.12:** A schematic representation of the photoelectric absorption process.



**Fig. 4.13:** Photoelectric mass attenuation coefficient of lead [3].

### 4.1.3.2 Compton Scattering

Compton scattering is the process whereby a gamma-ray interacts with a free or weakly bound electron ( $E_\gamma \gg E_b$ ) and transfers part of its energy to the electron (see Figure 4.14). Conservation of energy and momentum allows only a partial energy transfer when the electron is not bound tightly enough for the atom to absorb recoil energy. This interaction involves the outer, least tightly bound electrons in the scattering atom. The electron becomes a free electron with kinetic energy equal to the difference of the energy lost by the gamma-ray and the electron binding energy. Because the electron binding energy is very small compared to the gamma-ray energy, the kinetic energy of the electron is very nearly equal to the energy lost by the gamma-ray:

$$E_e = E_\gamma - E'$$

(4.25)

where,

$E_e$  = energy of scattered electron

$E_\gamma$  = energy of incident gamma ray

$E'$  = energy of scattered gamma ray.

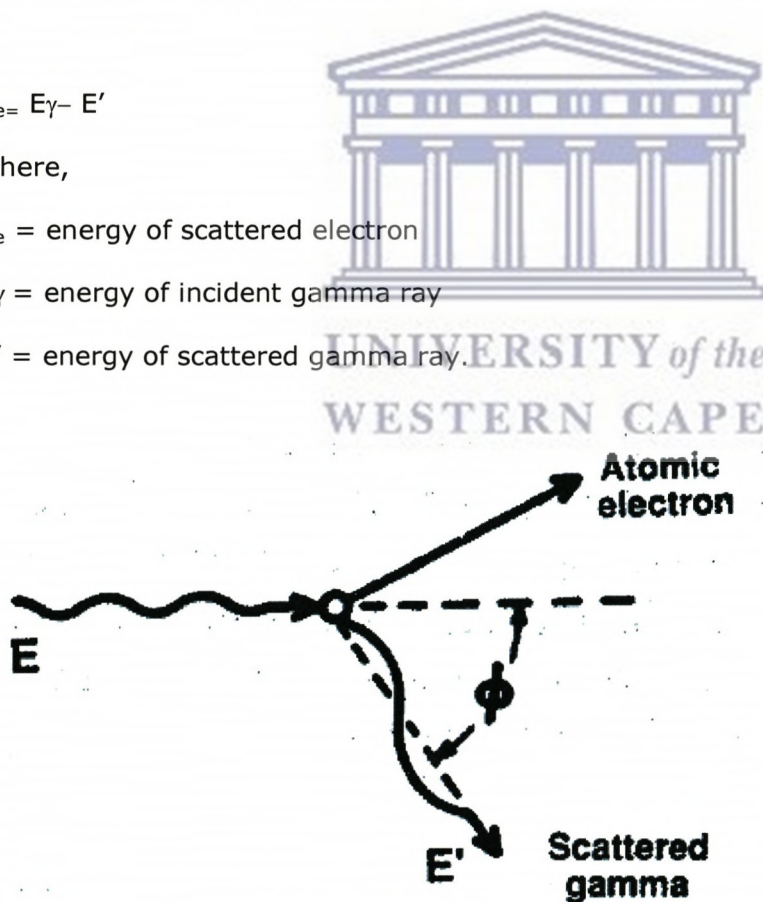


**Fig. 4.14:** A schematic representation of Compton scattering.

Two particles leave the interaction site: the freed electron and the scattered gamma-ray. The directions of the electron and the scattered gamma-ray depend on the amount of energy transferred to the electron during the interaction. Equation 4.26 gives the energy of the scattered gamma ray, and Figure 4.15 shows the energy of the scattered electron as a function of scattering angle and incident gamma-ray energy.

$$E' = m_0c^2 / (1 - \cos \phi + m_0c^2 / E) \quad (4.26)$$

where  $m_0c^2$  is the rest energy of electron = 511 keV

$\phi$  is angle between incident and scattered gamma rays (see Figure 4.14).

This energy is minimum for a head-on collision where the gamma ray is scattered 180° and the electron moves forward in the direction of the incident gamma ray. For this case the energy of the scattered gamma ray is given by Equation 4.27 and the energy of the scattered electron is given by Equation 4.28:

$$E' = m_0c^2 / (2 + m_0c^2 / E) \quad (4.27)$$

$$\approx m_0c^2 / 2 = 256keV; \quad \text{if } E \geq m_0c^2 / 2$$

$$E'(\text{max}) = [E / (1 + m_0c^2 / (2E))] \quad (4.28)$$

$$\approx E - m_0c^2 / 2 = E - 256keV; \quad \text{if } E \geq m_0c^2 / 2$$

For very small angle scatterings ( $\phi \approx 0$ ), the energy of the, scattered gamma ray is only slightly less than the energy of the incident gamma ray and the scattered electron takes very little energy away from the interaction. The energy given to the scattered electron ranges from near zero to the maximum given by Equation 4-28.



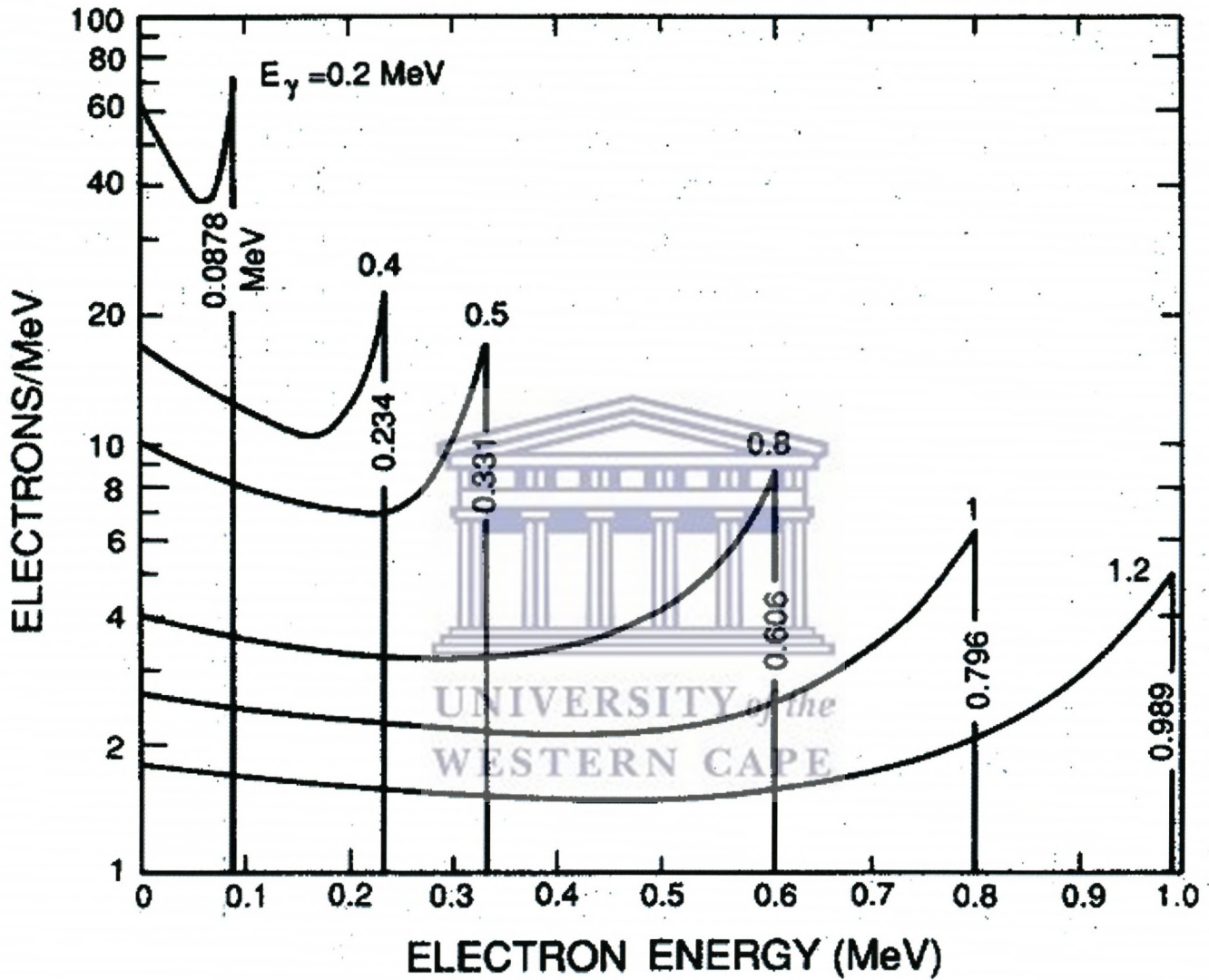


**Fig. 4.15:** Energy of Compton-scattered electrons as a function of scattering angle and incident gamma-ray energy ( $E_\gamma$ ). The sharp discontinuity corresponds to the maximum energy that can be transferred in a single scattering [3].

When a Compton scattering occurs in a detector, the scattered electron is usually stopped in the detection medium and the detector produces an output pulse that is proportional to the energy lost by the incident gamma ray. Compton scattering in a detector produces a spectrum of output pulses from zero up to the maximum energy given by Equation 4.28. It is difficult to relate the Compton-scattering spectrum to the energy of the incident gamma ray.

Figure 4.16 shows the measured gamma-ray spectrum from a mono energetic gamma-ray source ( $^{137}\text{Cs}$ ). The full-energy peak at 662 keV is formed by interactions where the gamma ray loses all of its energy in the detector either by a single photoelectric absorption or by a series of Compton scattering followed by photoelectric absorption.

The spectrum of events below the full-energy peak is formed by Compton scattering where the gamma ray loses only part of its energy in the compound. The step near 470 keV corresponds to the maximum energy that can be transferred to an electron by a 662 keV gamma-ray in a single Compton scattering. This step is called a Compton edge the energy of the Compton edge is given by Equation 4.28 and plotted in Figure 4.17. The small peak at 188 keV in Figure 4.16 is called a backscatter peak. The backscatter peak is formed when the gamma-ray undergoes a large-angle scattering ( $\approx 180^\circ$ ) in the material surrounding and then is absorbed in the compound.

The energy of the backscatter peak is given by Equation 4.27, which shows that the maximum energy is 256 keV. The sum of the energy of the backscatter peak and the Compton edge equals the energy of the incident gamma-ray. Both features are the result of large-angle Compton scattering of the incident gamma ray. The event contributes to the backscatter peak when only the scattered gamma ray deposits its

energy in the detection it contributes to the Compton edge when only the scattered electron deposits its energy in the compound.

Because Compton scattering involves the least tightly bound electrons, the nucleus has only a minor influence and the probability for interaction is nearly independent of atomic number. The interaction probability depends on the electron density, which is proportional to  $Z/A$  and nearly constant for all materials. The Compton-scattering probability is a slowly varying function of gamma-ray energy.

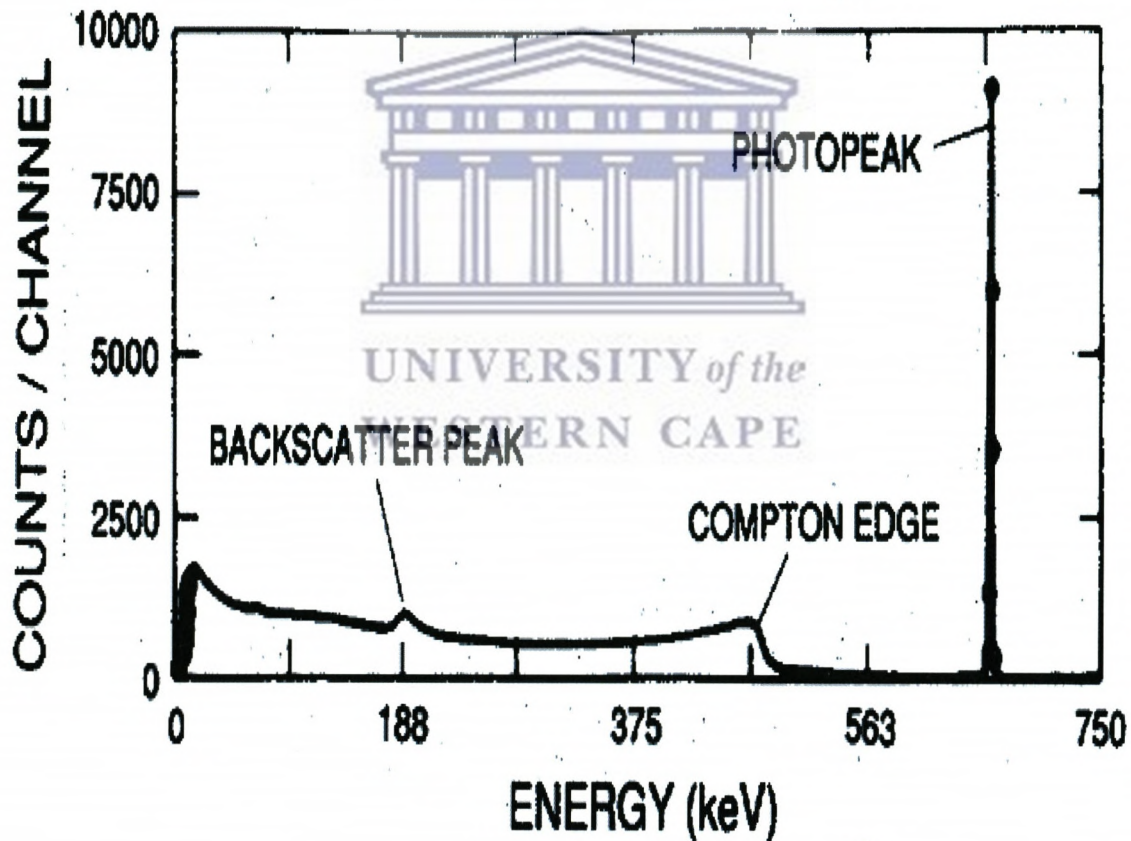


**Fig. 4.16:** High-resolution spectrum of  $^{137}\text{Cs}$  showing full-energy photo peak, Compton edge, and backscatter peak from the 662 keV gamma ray. Events below the photo peak are caused by Compton scattering in the detector and surrounding materials [3].

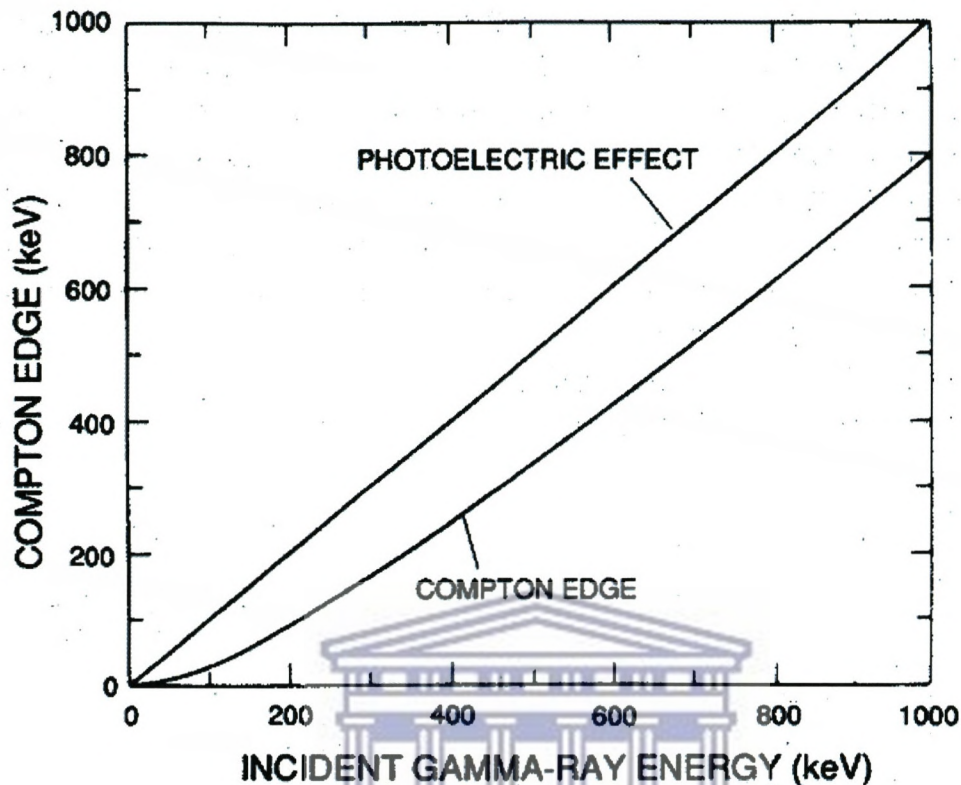


**Fig. 4.17:** Energy of the Compton edge versus the energy of the incident gamma ray [3].

UNIVERSITY of the  
WESTERN CAPE

#### 4.1.3.3 Pair Production

A gamma-ray with energy of at least 1.022 MeV can create an electron-positron pair when it is under the influence of the strong electromagnetic field in the vicinity of a nucleus (see Figure 4.18). In this interaction the nucleus receives a very small amount of recoil energy to conserve momentum, but the nucleus is otherwise unchanged and the gamma ray disappears. This interaction has a threshold of 1.022 MeV because that is the minimum energy required to create the electron and positron. If the gamma-ray energy exceeds 1.022 MeV, the excess energy is shared between the electron and positron as kinetic energy. This interaction process is relatively unimportant for nuclear material assay because most important gamma-ray signatures are below 1.022 MeV.

The electron and positron from pair production are rapidly slowed down in the absorber. After losing its kinetic energy, the positron combines with an electron in an annihilation process, which releases two gamma rays with energies of 0.511 MeV. These lower energy gamma-rays may interact further with the absorbing material or may escape. In a gamma-ray detector, this interaction often gives three peaks for a high-energy gamma ray (see Figure 4.19).

The kinetic energy of the electron and positron is absorbed in the detector. One or both of the annihilation gamma rays may escape from the detector or they may both be absorbed. If both annihilation gamma-rays are absorbed in the detector, the interaction contributes to the full-energy peak in the measured spectrum; if one of the annihilation gamma-rays escapes from the detector, the interaction contributes to the single-escape peak located 0.511 MeV below the full-energy peak; if both gamma rays escape, the interaction contributes to the double-escape peak located 1.022 MeV below the full-energy peak. The relative heights of the three peaks depend on the energy of the incident gamma-ray and the size of the detector. These escape peaks may arise when samples of irradiated fuel, thorium, and  $^{232}\text{U}$  are measured because these materials have important gamma rays above the pair-production threshold. Irradiated fuel is sometimes measured using the 2186 keV gamma ray from the fission-product  $^{144}\text{Pr}$ . The gamma-ray spectrum of  $^{144}\text{Pr}$  in Figure 4.19 shows the single and double-escape peaks that arise from pair-production interactions of the 2186keV gamma ray in a germanium detector.

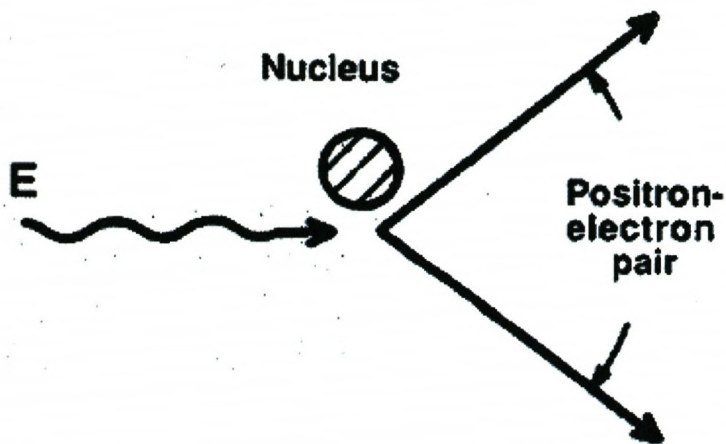


Fig. 4.18: A schematic representation of pair production.

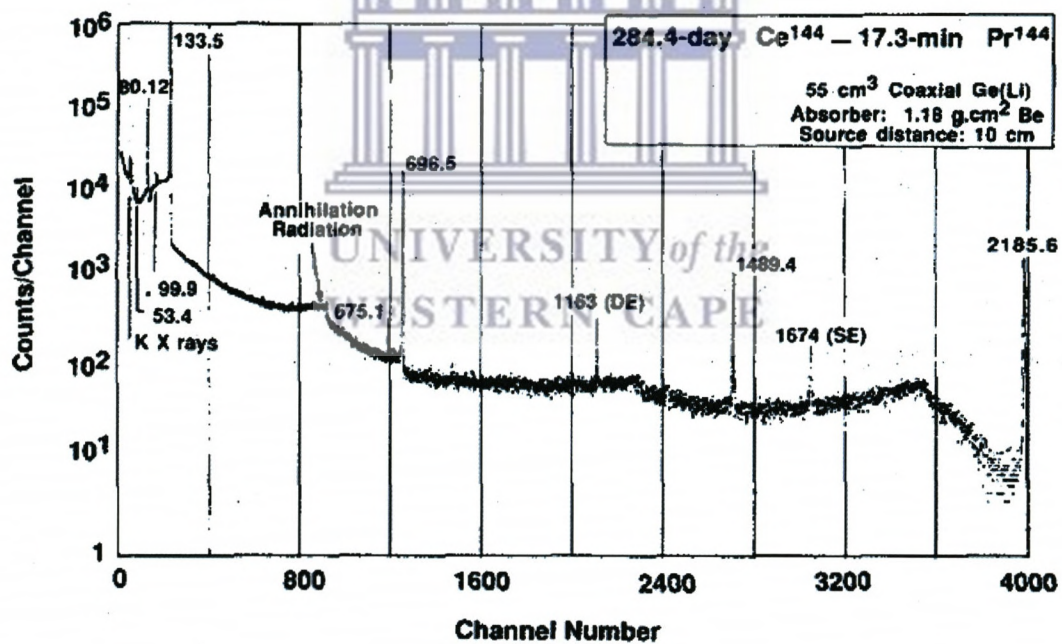


Fig. 4.19: Gamma-ray spectrum of the fission-product  $^{144}\text{Pr}$  showing single-escape (SE) and double-escape (DE) peaks (1674 and 1163) that arise from pair-production interactions of 2186 keV gamma rays in a germanium detector [3].

Pair production is impossible for gamma rays with energy less than 1.022 MeV. Above this threshold, the probability of the interaction increases rapidly with energy. The probability of pair production varies approximately as the square of the atomic number  $Z$  and is significant in high- $Z$  elements such as lead or uranium. In lead, approximately 20% of the interactions of 1.5-MeV gamma rays are through the pair-production process, and the fraction increases to 50% at 2.0 MeV. For carbon, the corresponding interaction fractions are 2% and 4%.

#### **4.1.3.4 Interactions with electrons**

The interactions of solids with electrons has been studied extensively by many researchers, however the effects of irradiation is comparatively small in contrast to the effect other high-energy particles. There are two important aspects in relation to the interest in the study of the irradiation of solids using electrons. Irradiation with electrons using energies above 1 MeV gives rise to both simple known point defects (vacancies, substitution and interstitial atoms) and the complexes. On the other hand irradiation with low energies (below 1 MeV) makes it possible to determine the configuration of defect-related centers and their behavior under the effect of various factors. This approach can be used to determine the threshold energy for the defect formation ( $E_d$ ), i.e. the minimum energy that the particle must transfer to an atom in the semiconductor lattice in order to form a common known Frenkel defect. This type of a defect is produced by the displacement of an atom from its normal lattice site [20] and concluded that the vacancy left behind together with the original atom in an interstitial position constitute a trapping site for normal charge carriers.

When an energetic particle enters the solid material, it interacts with electrons and nuclei. The energy loss of the particle depends on the nature of the incident particle and its energy. Elastic collisions with the nuclei lead to atomic displacements, whereas the

interaction with the electrons of the solid target material determines the penetration depth of the incident particle. Figure 4.20 gives a schematic picture of a simple binary elastic collision and described by the following equation (4-29).

$$T = \frac{2m}{M} E \left( 2 + \frac{E}{mc^2} \right) \cos^2 \phi \quad (4-29)$$

E is the kinetic energy of the incident particle with mass M. The amount of kinetic energy T transmitted to the atom of mass M depends strongly on the angular deflection of the incident particle.

The studies done by various researchers on the irradiation of SiC with high energy electrons reveal that the main radiation defects in SiC polytypes were isolated neutral silicon vacancies  $V_{Si}$  or negatively charged silicon vacancies  $V_{Si}^-$  [21-23] as illustrated in fig 4.21.

Inui et al. [24], in their measurements found that the threshold dose for amorphization of SiC irradiated with electrons is equal to  $10^{22}$ - $10^{23}$  cm<sup>-2</sup>.

The temperature of annealing the electron irradiation created defects is dependent on the SiC polytype.

Bae et al. [25], reported on the structural changes of SiC under electron-beam irradiation. Single crystalline 6H-SiC wafers were subjected to heavy electron irradiation using TEM equipped with field emission gun at various irradiation temperatures.

The acceleration voltage of electrons used in this study was 300 kV. Electrons accelerated by 300 kV transfer up to 30 eV to Si and 71 eV to C. Previous studies have shown that the threshold displacement energies for Si and C atoms were reported to be 35 and 20 eV, respectively [26].



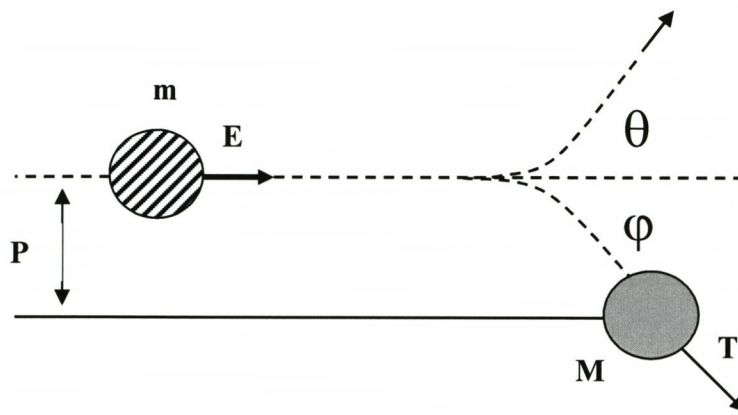


**Figure 4.20:** gives a schematic picture of a simple binary elastic collision.

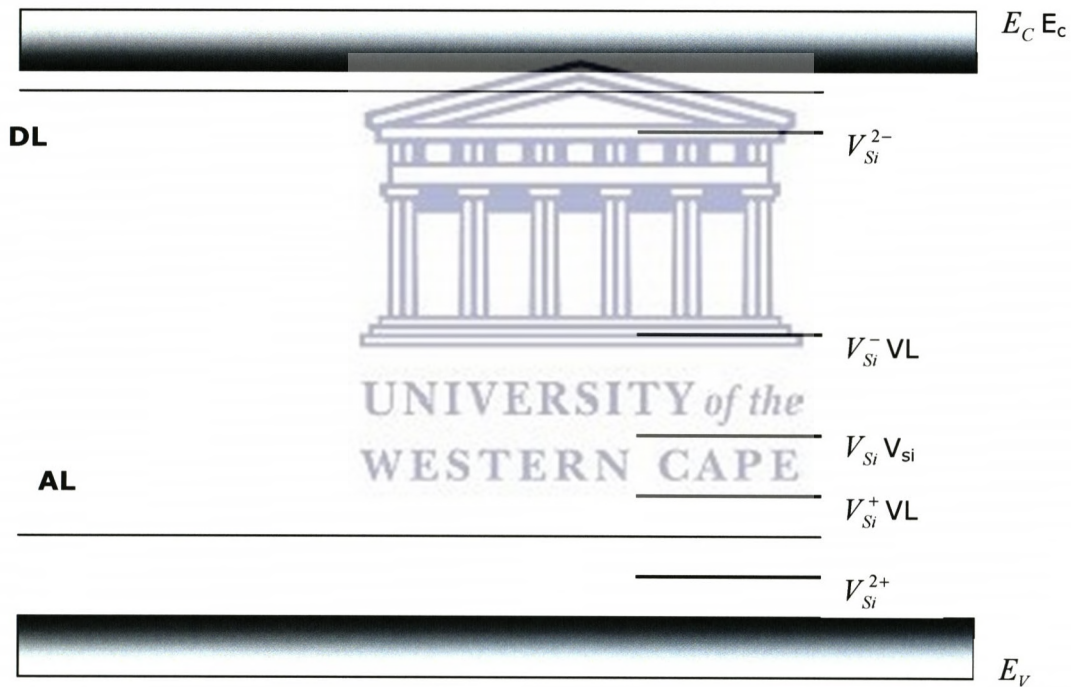


**Figure 4.21:** Schematic representations of positions of the energy levels for silicon vacancies in the SiC band gap. DL stand for donor level and AL stands for acceptor level.

During electron irradiation, the temperatures varied from -170 °C through room temperature to 250 °C (RT) using TEM specimen holders equipped with a cooling and a heating stage. It was found that at temperatures of -170 °C and RT, amorphization of 6H-SiC occurred. It is considered that the preferential knock-on displacement of C atoms by incident 300 kV electrons is responsible for amorphization at -170°C and RT irradiations. In the electron irradiation at 250 °C, crystalline Si was induced from 6H-SiC.

Recently, Kozubal et al. [27], have reported on the Effect of electron irradiation on defect structure of 6H-SiC grown by physical vapour transport (PVT) method. They have used a both sides mirror polished n-type 6H-SiC:N wafer with (0001) orientation. DLTS was used in the determination of deep-level defects detected in the samples of 6H-SiC:N before and after electron irradiation. It is found that the irradiation with a dose of  $\sim 2 \times 10^{17} \text{ cm}^{-2}$  of 300 keV electrons results in the formation of 0.50 eV electron trap, cautiously identified with carbon vacancies, whose concentration in the as-irradiated material is  $\sim 2 \times 10^{17} \text{ cm}^{-3}$ . The effect of the irradiation dose on the concentration of electron traps is also discussed.

Muto et al. [28], investigated the damaging process of  $\alpha$ -SiC under electron irradiation in a transmission electron microscope. A commercial (0001) oriented 6H-SiC wafer (n-type) was submitted to electron irradiation in an ultra-high voltage transmission electron microscope at accelerating voltages of 1.25 MV at 108 K with a dose rate of  $1.8 \times 10^{-3} \text{ dpa/s}$ . The irradiated samples were examined using TEM equipped with an electron energy-loss spectrometer (EELS). The experimental results revealed that there was a considerable volume swelling occurred by amorphization due to electron irradiation. It was further revealed that damaging process is mainly characterized by the different mobility of displaced atoms and stability of the C- and Si-sublattices. During which the structural disordering, Si-Si direct bonding is more easily formed than

C-C bonding in the matrix. A comparison with other studies is being made and amorphization mechanism at room temperature is further discussed.

## **4.2 Irradiation effects on SiC**

The effects of different irradiation on the mechanical properties and the microstructure of SiC and SiC-based fibers is currently the main focal point world-wide for the improvement of radiation damage resistant materials. Low fluence irradiation of SiC is known to produce point defects, such as vacancies and interstitials, or point like defects such as divacancies or antisites. These defects introduce deep levels in the material's energy band gap and deep level transient spectroscopy [29] is mostly employed and suitable for the characterization of these levels at low fluence. At higher fluences channeling Rutherford Backscattering Spectroscopy (RBS) and Positron Annihilation Spectroscopy is mostly used to characterize different kinds of defects due to its sensitivity. Defects and impurities often affect the electrical, optical and other physical properties of SiC. The annealing properties of intrinsic and impurity-related defects have been investigated in irradiated SiC by various experimental techniques and computer simulations. There is still a need for a better understanding of the defect migration processes and formation mechanism of defect clusters particularly, formed after high dose at high temperature irradiation. Annealing of these irradiation-induced defects has been performed by different researchers at different temperatures. This section deals with on the overview of the effects of different irradiation on the physical properties and the microstructure of SiC and SiC-based materials mostly reported so far in the literature.

#### 4.2.1 Irradiation with protons

Protons and  $\alpha$ -particles are equally effective at revealing growth features in materials, but protons have a unique advantage of greater penetration, enabling surface scratches to be defocused during microscopic examination. These lightest ions represent the main fraction of cosmic radiation (~80%) and it was reported that if accelerated at energies up to 50 MeV, a large number of primarily displaced atoms can be expected due to its elastic scattering by the atoms and nuclei of the target material [30]. Protons generate mostly elementary radiation defects, vacancies and interstitial atoms, which act not only as simple structural distortions, but also as diffusion carriers of metal and semiconductor atoms [31-35].

Litrico et al. [36] has reported on the low temperature reaction of point defects in ion irradiated 4H-SiC. In this study the defects in 4H- and 6H-SiC were introduced by irradiation with a 7.0 MeV of  $C^+$  ions at fluence of  $6 \times 10^9 \text{ cm}^{-2}$ . Annealing followed at the temperature range of 57-127°C. This team concluded that the defects in 4H- and 6H-SiC created as a result of irradiation were stabilized by low temperature annealing.

Von Bardeleben et al. [37], by using Electron Paramagnetic Resonance (EPR), studied proton implantation induced defects in monocrystalline 4H- and 6H-SiC. The samples were irradiated at room temperature with 12 MeV protons at doses between 1 and  $8 \times 10^{16} \text{ cm}^{-2}$ . They found that different defects are created for proton irradiated n- and p-type 6H-SiC.

#### 4.2.2 Irradiation with Neutrons

During normal operation of the nuclear reactor, neutrons are amongst the species emitted as a result of nuclear fission. Generally, neutrons can penetrate deep into the matter. They have a broad spectrum of energies from 0 to 15 MeV. Neutrons irradiation results in degradation of materials. Intense bombardment with neutrons creates dislocations in materials, leading to embrittlement of metals and other materials, and to

swelling to some of them. This poses a problem for nuclear reactor vessels, and significantly limits their lifetime which can be somewhat prolonged by controlled annealing of the vessel, reducing the number of the built-up dislocations. Under hostile environment, such as neutron irradiation, many materials suffer neutron induced damages and undergo structural changes such as swelling, amorphization and in turn affect their mechanical, chemical and physical properties.

Although SiC has been reported to withstand such hostile conditions, the material properties are strongly affected by intrinsic and extrinsic defect centers formed during the crystal growth. Thus, to control the material quality, it is important to know the electronic properties of defect centers and to understand their nature. The studies of intrinsic defects can be most conveniently performed on neutron irradiated material. There are a number of techniques used previously to characterize the irradiation defect centers as a result of irradiation of SiC crystals with thermal neutrons. The increase in the interest to study the effect of irradiation with neutrons on the structural properties of SiC was awakened after when it was reported that nuclear transmutational doping of this compound with phosphorus <sup>31</sup>P can be attained using irradiation of this semiconductor with thermal neutrons [38].

Recently, Xu et al. [39], used positron annihilation spectroscopy to study the vacancy-defect type of neutron irradiated 4H-SiC. The sample was irradiated with neutron dose of up  $3.2 \times 10^{21} \text{ m}^{-2}$  with an energy  $E > 1 \text{ MeV}$  at  $200^\circ\text{C}$ . After irradiation annealing was carried out from  $50^\circ\text{C}$  to  $1600^\circ\text{C}$  in a helium gas flow. After careful analysis using Positron Annihilation Spectroscopy, it was found that carbon and silicon vacancies and carbon silicon di-vacancies were formed. The recovery process comprised of several stages. However, it was concluded that vacancy-type defect in 4H-SiC was annealed out at temperature of  $1600^\circ\text{C}$ , but interstitial-type defects and anti-site defects were stable.

Kondo et al. [40], studied the microstructural defects in neutron irradiated SiC at high temperatures using transmission electron microscopy. A high purity poly crystalline  $\beta$ -SiC was irradiated with fast neutrons (up to  $9.6 \times 10^{25}$  n/m<sup>2</sup>) at very high temperatures, 1130, 1300 and 1460 °C with  $E > 0.1$  MeV. After TEM characterization, irradiation induced cavities, voids and dislocation loops were identified at all irradiation temperatures.

Snead et al. [41], studied neutron irradiation induced amorphization of silicon carbide. In this study, high purity single crystal *hcp* and high purity, highly faulted (cubic) chemically vapor deposited SiC were irradiated with fast neutron fluence to  $2.6 \times 10^{25}$  n/m<sup>2</sup> at 60 °C with  $E > 0.1$  MeV. Transmission electron microscopy, electron and X-ray diffraction were used to characterize the irradiated samples. It was found that high purity single crystalline  $\alpha$ -SiC and high purity polycrystalline  $\beta$ -SiC irradiated with neutrons to  $2.6 \times 10^{25}$  n/m<sup>2</sup> at 60 °C have transformed from the crystalline state with a density of  $3.203 \pm 0.001$  to an amorphization state 10.8% lower density.

Brink et al. [42], studied neutron irradiation effects in SiC polytypes (3c-SiC and 4H-SiC). For this study, the neutron irradiation was performed at nuclear reactor (SAFARI-1) using a total neutron fluence up to  $10^{16}$  n.cm<sup>-2</sup>. By using different optical characterization techniques such as UV-visible, Infra-red reflectance, Raman spectroscopy and Photoluminescence were employed as characterization tools for the study. Transmission measurements in the visible range clearly indicated that there is a small but measurable amount of amorphization present after irradiation with infra-red reflectance and Raman spectroscopy measurements showing that the long-range order in the SiC crystals has been disrupted. However, Brink et al. have concluded that high fluences is required for the effects on both SiC polytypes to be noticeable.

Shustov et al. [43], investigated the radiation defects in silicon carbide implanted by heavy ions of Bi at high energy. 6H-SiC Lely crystals were irradiated by  $^{209}\text{Bi}$  ions with different fluences:  $D = 5 \times 10^{10}$ ,  $1 \times 10^{11}$ ,  $1 \times 10^{13} \text{ cm}^{-2}$  and the implantation energy was 710 MeV. Cathodoluminescence was used as the characterization technique for the study.

Based on the results of this study, in all the fluences used there was a structural modification confirmed by catholuminescence techniques. The team concluded that radiation defects formation mechanism for heavy ions has the same nature as that for light ions, neutrons and electrons. There are two processes that are responsible for final radiation defect distribution in the implanted sample. Radiation accelerated diffusion is the first one and gettering effect is the second one. These mechanisms are leading to formation of area with radiation defects two order of magnitude deeper than ion penetration depth. Annealing of the implanted samples at high temperature results in partial disappearing of radiation defects due to annealing and diffusion.

#### 4.2.3 Irradiation with $\gamma$ -rays

Gamma rays are amongst the most ionizing radiation and it is important to understand their effects on the properties of silicon carbide. This material has been investigated for the use in hostile environments since 1963 [44]. Since then it has been reported by many researchers around the world that devices based on 6H-SiC optimized to work at high temperatures ( $>500 \text{ }^\circ\text{C}$ ) have shown to have negligible degradation for gamma radiation up to 100 Mrad but showed significant degradation with neutron irradiation for high fluences in excess of  $10^{16} \text{ n/cm}^2$ [45,46].

Yoshikawa et al. [47], studied the effects of gamma-ray irradiation on cubic silicon carbide metal-oxide semiconductor structure. The cubic (3C-SiC) is known to be the most stable polytype of all forms of the polytypes of SiC with a large band gap (2.2 eV at room temperature) and excellent thermal stability.

The fabricated 3C-SiC metal-oxide semiconductors, procedure described in [47] were irradiated with  $^{60}\text{Co}$  gamma-ray in an argon atmosphere at room temperature. The dose rate was 8.8 kGy ( $\text{SiO}_2$ )/h.

The conclusion on the study was made based on the measurements of the C-V after irradiation. It was observed that gamma-rays generate bulk defects as well as interface traps and oxide traps near the 3C-SiC/ $\text{SiO}_2$  interface. Based on the comparison of the irradiation effects with Si metal-oxide semiconductor structures, it was further concluded that the interface trapped charges and oxide trapped chargers are significantly lower for 3C-SiC structure compared with Si MOS structure.

Sheridan et al. [48] investigated the high dose gamma irradiation on high-voltage 4H-SiC schottky diode and SiC- $\text{SiO}_2$  interface. In this study a 4H-SiC was irradiated at room temperature in a gamma cell  $^{60}\text{Co}$  irradiator using high gamma irradiation dose of 10, 40, 100 krad(Si) and 1 Mrad (Si) (1Mrad (SiC) = 1.03 Mrad (Si)). It was found that the irradiated 4H-SiC schottky diodes were extremely radiation resistance up to 1 Mrad.

Kim et al. [49] reported on the high dose gamma ray irradiation of SiC schottky rectifiers. The substrates used in the study were a 4H-SiC based diodes. The devices were exposed to 600 Ci  $^{60}\text{Co}$  source for accumulated doses of approximately 300-600 Mrad. The study examined the reverse current-voltage characteristics before and after  $^{60}\text{Co}$  gamma irradiation to a dose of 600 Mrad.

The 4H-SiC schottky rectifiers showed fixed changes in reverse breakdown voltage even after very high  $^{60}\text{Co}$  gamma-rays doses (up to 600 Mrad) but the forward current and on-state resistance were badly degraded through the deterioration of the rectifying morphology.

Kang et al. [50], studied the current-voltage characteristics of a SiC radiation detector irradiated by  $^{60}\text{Co}$  gamma rays. The sample used was a 6H-SiC wafer. The samples were irradiated in a glass bottle with  $^{60}\text{Co}$  gamma rays. The irradiation was performed at doses of 5 and 15 kGy/h for 8 hours. The total doses of the two samples were 40 and



120 kGy, respectively. Based on the *I-V* measurements it was found that the leakage currents of the irradiated samples decreased relatively to the non-irradiated ones. It was reported in the literature that gamma rays irradiation can only create point defects. When enough of these defects have been formed, a carrier lifetime is reduced. The surface effects are directly related to the increase in leakage current. The effect of point defect caused by  $^{60}\text{Co}$  gamma rays irradiation decreased the leakage current as compared to the non-irradiated SiC samples.

#### 4.2.4 Irradiation with Laser

Many studies have been conducted on the irradiation of SiC using lasers. The interaction of laser radiation with semiconductors has been a subject of great interest in solid state physics. The first stage of this interaction is transformed into heat [51]. Medvid et al. [52], studied the formation of nanostructures on the surface of SiC by laser irradiation. In this study, a crystal of 6H-SiC (0001) was used. The experiment was conducted at room temperature and atmospheric pressure. The samples were irradiated by a focused  $\text{N}_2$  laser at an average intensity  $5 \text{ GW/m}^2$ .

On the irradiated surface, it was found that there's a formation of nanoholes which is as a result of melting because the temperature of the surface is lower than that in the bulk material. This temperature distribution has been explained to be as a result of the low sublimation energy for SiC. Medvid further said there was a decrease in the hardness of the irradiated surface due to a photomechanical effect and as a result nanohills were formed.

Gorelik et al. [53], investigated carbon onions produced by laser irradiation of amorphous SiC. Amorphous stoichiometric SiC films with a thickness in the range of 100-200 nm produced by pulsed laser deposition were irradiated with a single short of KrF laser. The experiment was conducted at sample temperature of  $600 \text{ }^\circ\text{C}$  with a single short of KrF laser (pulse duration 25 ns, fluence  $800 \text{ mJ/cm}^2$ ) at wavelength of 248 nm.

According to Si-C phase diagram shown in figure 3.6, the liquid phase of SiC does not exist. As concluded by Medvid [52], laser treatment of SiC induces melting of the surface layer. The high-intensity pulses induce vaporization of Si from the surface and deviate from the 1:1 stoichiometry in the liquid phase [54-55], leading to a graphite surface layer formation. Experiments with laser treatment of graphite showed that the irradiation causes a breakdown in well-ordered layers of hexagonal structural rings with solidification of an amorphous state [56]. In this experiment, carbon ions were produced inside a semi-conductive Nano crystalline SiC matrix using laser irradiation. The TEM results showed that the laser irradiation of amorphous SiC layers resulted in the crystallization of the surface-near region up to a depth of 50-100 nm. Larger crystals (up to 50 nm) were formed at the surface while smaller crystals (5-10 nm) were observed near the interface to the unaffected amorphous material. Konishi et al. [57], investigated the growth control of carbon nanotubes on silicon carbide surfaces using the laser irradiation effect. A 6H-SiC (0001) was irradiated with ArF laser with a wavelength of 193nm and power of 0.01 J/cm<sup>2</sup> and with a KrF excimer laser with wavelength of 248nm and power 0.01 J/cm<sup>2</sup>.

#### 4.3 References:

- [1] Thesis by Boon, Sjirk Niels, "Dosimetry and quality control of scanning proton beams", (1998)
- [2] P. Rinard, Neutron Interactions with Matter, Los Alamos Technical Report <http://www.fas.org/sqp/othergov/doe/lanl/lib-www/la-pubs/00326407.pdf>.
- [3] G. Nelson and D. Reilly, Gamma-Ray Interactions with Matter, Los Alamos Technical Report <http://www.fas.org/sqp/othergov/doe/lanl/lib-www/la-pubs/00326397.pdf>
- [4] H.A. Bethe and J. Ashkin, Passage of Radiations through Matter, Experimental Nuclear Physics (E. Segré, ed.), vol. I, Wiley, New York, p. 176 (1953).
- [5] L. Landau, On the energy loss of fast particles by ionization, J. Phys. USSR 8, 201 (1944).

- [6] P.V. Vavilov, Ionization losses of high energy particles, *Zh. Eksp. Teor. Fiz.* 32 (Engl. transl. *Sov. Phys. JETP* 5, 749, 1957) 920, (1957).
- [7] B. Schorr, Programs for the Landau and the Vavilov distributions and the corresponding random numbers, *Comp. Phys. Comm.* 7, 216 (1974).
- [8] H.J. Bhabha, On the Penetrating Component of Cosmic Radiation, *Proc. Roy. Soc. A*164, 257 (1938).
- [9] C.M. Perey and F.G. Perey, Optical-Model Parameters, 1954-1975, *Atomic Data and Nuclear Data Tables* 17, 23 (1976).
- [10] G. Molière, Theorie der Streuung schneller geladener Teilchen II. Mehrfach und Vielfachstreuung., *Z. Naturforschung* 3a, 78 (1948).
- [11] B. Gottschalk, A.M. Koehler, R.J. Schneider, J.M. Sisterson, and M.S. Wagner, Multiple Coulomb scattering of 160 MeV protons, *Nucl. Instrum. Methods B* 74, 467 (1993).
- [12] W.R. Leo, *Techniques for Nuclear and Particle Physics Experiments*, 2nd ed., Springer, New York, (1994).
- [13] ICRU, Stopping Powers and Ranges for Protons and Alpha Particles, Tech. Report 49, ICRU Bethesda MD, (1993).
- [14] M.J. Berger, Proton Monte Carlo Transport Program PTRAN, Tech. Report NISTIR 5113, NIST, (1993).
- [15] P.G. Young, E.D. Arthur, M. Bozoian, T.R. England, G.M. Hale, R.J. Labauve, R.C. Little, R.E. MacFarlane, D.G. Madland, R.T. Perry, and W.B. Wilson, Transport data libraries for Incident Proton and Neutron Energies to 100MeV, Tech. Report LA-11753- MS, Los Alamos National Laboratory, (1990).
- [16] D. L. Garber and R. R. Kinsey, "Neutron Cross Sections, Vol. II, Curves," Brookhaven National Laboratory report BNL 325 (1976).
- [17] Evaluated Nuclear Data File ENDF/B-V (available online and maintained by the National Nuclear Data Center of Brookhaven National Laboratory).
- [18] J. R. Lamarsh, *Introduction to Nuclear Reactor Theory* (Addison-Wesley, Reading, Massachusetts, (1966)).
- [19] S. Glasstone and A. Sesonske, *Nuclear Reactor Engineering* (D. Van Nostrand Co., Inc., Princeton, New Jersey, (1967)).

- [20] Knoll G F, Radiation Detection and Measurements 3rd edition (New York: Wiley) (2000)., K. Debertin and R. G. Helmer., Gamma- and X-ray Spectroscopy with Semiconductor Detectors., (Amsterdam: North-Holland) (1988).
- [21] V.S. Balandovich and G.N. Violina, Cryst. Lattice Defects Amorphous Mater. 13, 189 (1987).
- [22] J. Scheneider and K. Maier, Physica B (Amsterdam) 185, 199 (1993).
- [23] A.I. Girka, V.A. Kuleshin, A.D. Mokroshin, et al., Fiz. Tekh. Poluprovodn., Sov. Phys. Semicond. 23 1337 (1989).
- [24] H. Inui, H. Mori, and H. Fujuta, Philos. Mag. B 61, 107 (1993).
- [25] I. Bae , M. Ishimaru, Y. Hirotsu, Nucl. Instr. and Meth. B 250 315 (2006).
- [26] R. Devanathan, W.J. Weber, F. Gao, J. Appl. Phys. 90 2303 (2001).
- [27] M. Kozubal, P. Kamiński, R. Kozłowski, E. Tymicki, K. Graszka, S. Warchoł, Superlattices and Microstructures 45 402 (2009).
- [28] S. Muto, T. Tanabe, T. Shibayama, H. Takahashi, Nucl. Instr. and Meth. B 191 519 (2002).
- [29] D.V. Lang, J. Appl. Phys. 45 3023 (1974).
- [30] V.M Lulakov, E.A. Ladygin, V.I Shakhov, et al. Effect of penetrating radiation on semiconductor devices, Ed. By E.A. Ladygin Sovetskoe Radio, Moscow, 34 (1980).
- [31] V.V. Kozlovski, V.N. Lomasov, Surface Invest. 3 146 (1987).
- [32] V.V. Kozlovski, V.A. Kozlov, V.N. Lomasov, Semiconductors 34 123 (2000).
- [33] V. Kozlovski, V. Abrosimova, Radiation Defect Engineering, World Scientific, Singapore (2005).
- [34] V.V. Kozlovski, V.N. Lomasov, D.S. Rumyantsev, I.V. Grekhov, P.A. Ivanov, T.P. Samsonova, H.I. Helava, L.O. Ragle, Nucl. Instr. and Meth. B 215 385 (2004).
- [35] V.V. Kozlovski, P.A. Ivanov, D.S. Rumjanzev, V.N. Lomasov, T.P. Samsonova, Semicond. 38 745 (2004).
- [36] G. Litrico, G. Izzo, L. Calcagno, F. La Via, G. Foti Diamond ad Related materials 18 39-42 (2009).
- [37] H.J. von Bardeleben, J.L Cantin, Nucl. Inst. And Meth. B 186 2001 (2002).
- [38] E. Meese Plenum., Neutron transmutation Doping in Semiconductors, 3rd Ed. By, New York (1979).
- [39] Q. Xu, T. Yoshiie, M. Okada, J. Nucl. Mater. (2009).
- [40] S. Kondo, Y. Katoh, L.L. Snead, J. Nucl. Mater. 382 160 (2008).
- [41] L.L. Snead, J.C. Hay, J. Nucl. Mater. 273 213 (1999).

- [42] D.J. Brink, J. Malherbe, J. Camassel, Nucl. Instr. And meth. Phys. Res. B 267 2716 (2009).
- [43] D. Shustov, V. Kalinin, E. Kalinina, M. Zamoryanskaya, Physica B 404 4761 (2009).
- [44] G. Ervin Jr., J. Am. Ceram. Soc. 41 347 (1958).
- [45] S. Seshadri, R. Dullo, F. Rudy, J. Seidel and L. Rowland, IEEE Trans. Elect. Devices 46, 3 567 (1999).
- [46] J. McGarrity, F. McLean, W. DeLancey, J. Palmour, C. Carter, J. Edmond and R. Oakey, IEEE Trans. Nucl.Sci. 39 1974 (1992).
- [47] M. Yoshikawa, H. Itoh, Y. Morita, I. Nashiyama, S. Misawa, H. Okumura, S. Yoshida, J.Appl.Phys. 70 1309 (1991).
- [48] D.C. Sheridan, G. Chung, S. Clark, J.D. Cressler, IEEE Trans. Nucl. Sci. 6, 48 (2001).
- [49] J. Kim, S. Nigam, F. Ren, D. Schoenfeld, G.Y. Chung, S.J. Pearton, Electrochemical and Solid-state Lett. 8 G105 (2003).
- [50] S.M. Kang et al., Nucl. Instr. and Meth. A 579 145 (2007).
- [51] D.K. Biegelsen, G.A. Rozgonyi, and C.V Shank, Mater. Res. Soc. 32 (1985).
- [52] A. Medvid, B. Berzina, L. Trinkler, L. Fedorenko, P. Lytvyn, N. Yusupov, T. Yamaguchi, L. Sirghi, and M. Aoyama, Phys. Stat. Sol. (a) 195., 1 199 (2003).
- [53] T. Gorelik, S. Urban, F. Falk, U. Kaiser, U. Glatzel, Chem. Phys. Lett. 373 642 (2003).
- [54] S. Urban, F. Falk, T. Gorelik, U. Kaiser, Mater. Sci. Forum. 87 389 (2002).
- [55] D.K. Senguta, N.R. Quick, A. Kar, J. Laser-appl. 13 26 (2001).
- [56] M.B. Agramat, S.I. Ashitkov, A.V. Kivrillin, A.V. Kostanoviski, V.E. Fortov, S.I. Anisimov, P.S. Kondratenko, J. Phy. lett. 66 699 (1997).
- [57] H. Konishi, H. Matsuoka, N. Toyama, M. Naitoh, S. Nishgaki, M. Kusunoki, thin solid films, 464 295 (2004).

## CHAPTER 5

### CHARACTERIZATION TECHNIQUES

---

#### 5.1 X-ray diffraction

The structural characterization of the samples has been performed by X-ray diffraction. X-ray diffraction (XRD) is a versatile, non-destructive technique used for qualitative and quantitative analysis of crystalline materials. X-ray diffraction is a quick and efficient technique for phase identification in thin films. This technique has been used to determine the overall structure of bulk solids, including lattice constants, identification of the unknown materials, orientation of single crystals, orientation of polycrystalline, stress, texture, film thickness etc. the interaction of X-rays with sample create a secondary "diffracted" beams of X-ray related to interplanar spacing in the crystalline powder according to a relationship called Bragg's Law [1]:

$$2d \sin\theta = n\lambda$$

(5.1)

With variable  $d$  being the distance between atomic layers in a crystal,  $n$  the order of the reflection,  $\lambda$ , the variable lamda is the wavelength of the incident x-ray beam (see figure 5.1 below) and  $\theta$  the incident angle. This relationship states that for a constant interpalnar distance and incoming energy constructive will occur at a scattering angle of  $\theta$ . The Bragg law requires that  $\theta$  and  $\lambda$  can be matched for diffraction by varying  $\theta$  and recording where constructive interference occurs the  $d$  spacing of the crystal planes can be measured. Diffraction occurs from crystallites, which happen to be oriented at the angle to satisfy the Bragg condition [1-3].

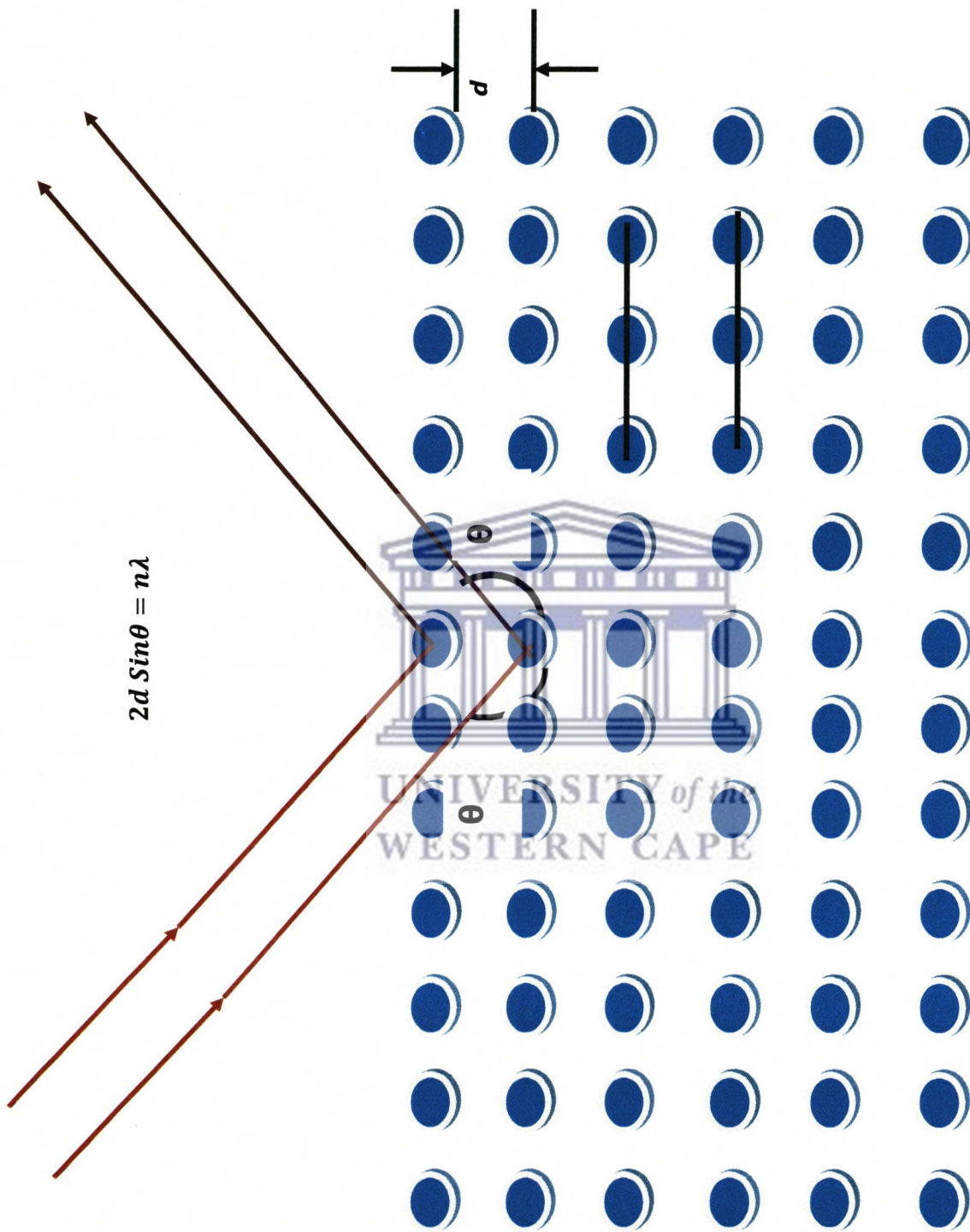
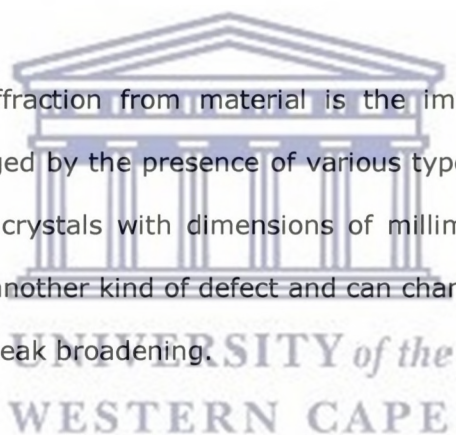


Figure 5.1: Bragg's law

Diffractometers come in two different basic varieties:  $\theta$ - $\theta$  in which the x-ray tube and detectors move simultaneously (Bragg-Brentano) or a  $\theta$ - $2\theta$  in which the x-ray tube is fixed, and the specimen moves at  $\frac{1}{2}$  the rate of the detector to maintain the  $\theta$ - $2\theta$  geometry. The angle of diffraction (recorded as  $2\theta$  by conversion) is related to the interplanar spacing,  $d$ , by the Bragg Law and intensity of the diffraction maximum is related to the strength of those diffractions in the specimen. A spectrum of reflections of the family of planes parallel to the sample surface is obtained. The analysis of this spectrum permits the identification of the crystalline species of the sample. A more precise analysis of the diffraction profile permits the measurements of structural parameters.

Another aspect of the diffraction from material is the importance to consider how diffraction peaks are changed by the presence of various types of defects such as small number of dislocations in crystals with dimensions of millimeters. Small size of grain size can be considered as another kind of defect and can change diffraction peak widths. Very small crystals cause peak broadening.



The crystallite size is easily calculated as a function of peak width (specified as the full-width at half maximum peak intensity (FWHM)), peak position and wavelength using the well known Scherrer's formula.

$$D = \frac{0.9\lambda}{\Delta(2\theta)\cos\theta} \quad (5.2)$$

It is used to estimate the size of crystals from measured width of the diffraction peaks. Note that whether a value of 0.9 or 1 is used depends on shapes of the crystallites assumed to be sample.



Figure 5.2 shows the XRD D8 advance Bruker diffractometer, with  $\text{CuK}_\alpha$  radiation of wavelength  $1.54 \text{ \AA}$  and a position sensitive Lynx-Eye, Si-strip detector with 196 channels. facility used at iThemba LABS for the crystallographic study of the samples.

### 5.1.1 Generation of X-ray

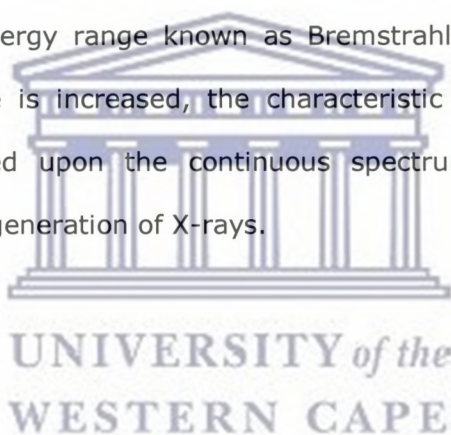
X-rays can be thought of as waves with wavelengths on the order of  $0.1 \text{ \AA}$  to  $\sim 10 \text{ \AA}$ . The shorter the wavelength, the more energetic the wave. Because of the relatively short wavelengths of electromagnetic radiation in the X-ray region, X-rays are high energy waves and are much more penetrating compared to UV, visible, IR, or radio waves. The conversion between energy, frequency, and wavelength is the well-known de Broglie relationship:

$$E = h\nu = hc/\lambda, \quad (5.3)$$

where  $\nu$  is the frequency,  $h$  is Planck's constant ( $6.62 \times 10^{-34}$  joule-second),  $c$  is the speed of light ( $2.998 \times 10^8$  m/sec), and  $\lambda$  is the wavelength of the radiation (in m).

When electrons strike a metal anode with sufficient energy, X-rays are produced. This process is usually accomplished using sealed x-ray tube, which consist of a metal target (often copper metal) and a tungsten metal filament, which can be heated by passing a current through it (typically  $10^{-15}$  mA), resulting in the "boiling off" of electrons from the hot tungsten metal surface. These "hot" electrons are accelerated from the tungsten filament (negative bias) to the metal target (positive bias) by an applied voltage (typically 15-30 kilovolts). The collision between these energetic electrons and electrons in the target atoms results in electron from target atoms being excited out of their core-level orbitals, placing the atom in a short-lived excited state. The atom returns to its ground state by having electrons from lower binding energy levels (i.e. levels further from the nucleus) make transitions to the empty core level. The difference in energy

between these lower and higher binding energy levels is radiated in the form of X-rays. This process results in the production of characteristic X-rays (i.e. X-rays whose energies are unique to the target metal due to the quantized nature of the electron energy levels of each atom and the unique energies of these energy levels) [Cu K $\alpha$ 1 (L3 to K electronic transition:  $E = 8047.78$  eV,  $\lambda = 1.54051$  Å), Cu K $\alpha$ 2 (L2 to K electronic transition:  $E = 8027.83$  eV,  $\lambda = 1.54433$  Å), Cu K $\beta$ 1 (M3 to K transition:  $E = 8905.29$  eV,  $\lambda = 1.39217$  Å)]. Thus X-rays provide a convenient means of determining what elements are present in a sample because of the unique wavelengths produced by each unique element. A lower energy process that involves the interaction of electrons with the nucleus of an atom in the target metal produces a continuum of lower intensity X-radiation over a broad energy range known as Bremsstrahlung [4]. As the voltage is made on; the X-ray tube is increased, the characteristic line spectra of the target element are superimposed upon the continuous spectrum. Figure 5.3 shows the schematic diagram of the generation of X-rays.



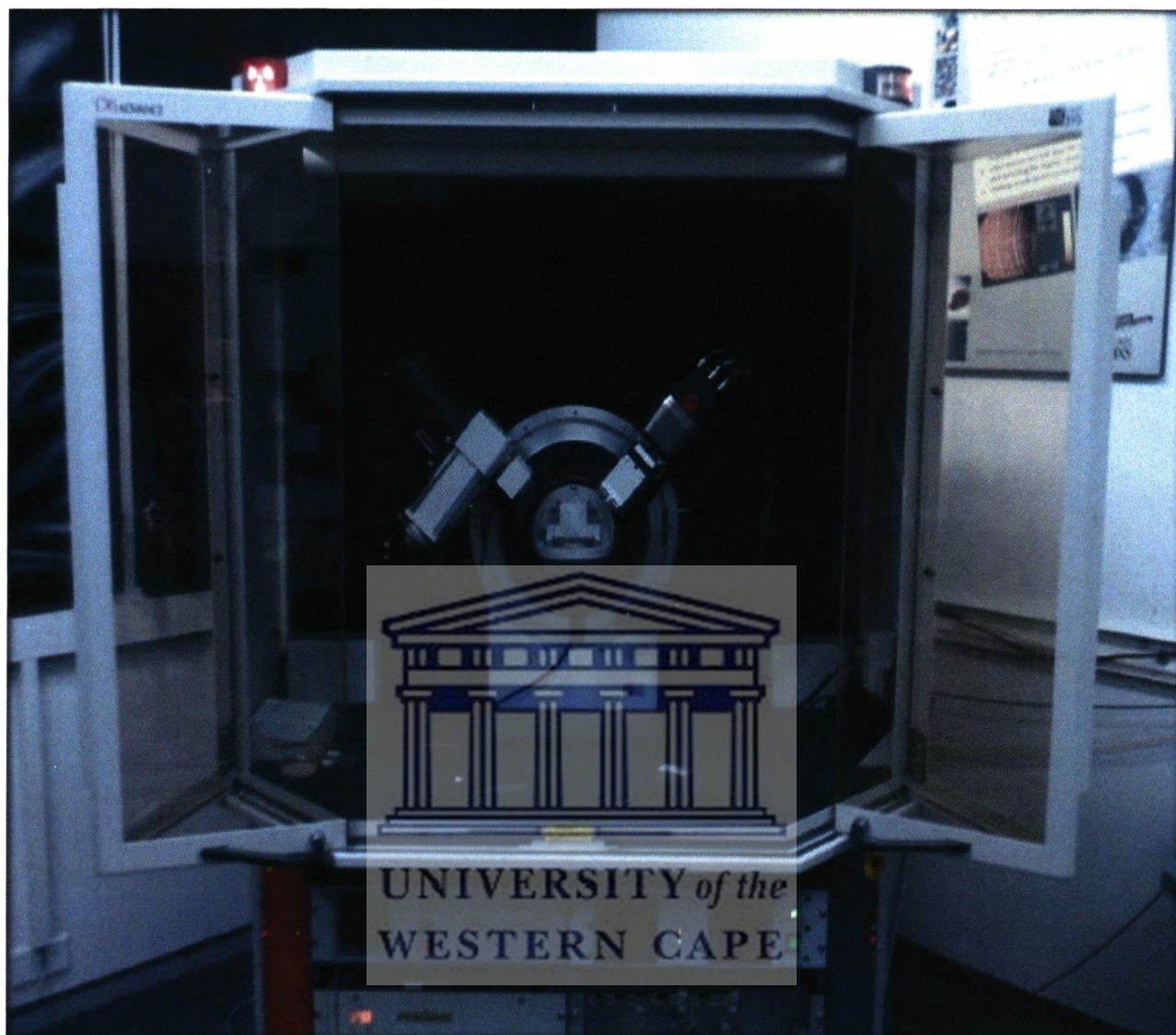


**Figure 5.2:** XRD facility at iThemba LABS used for the crystallographic study of the samples.

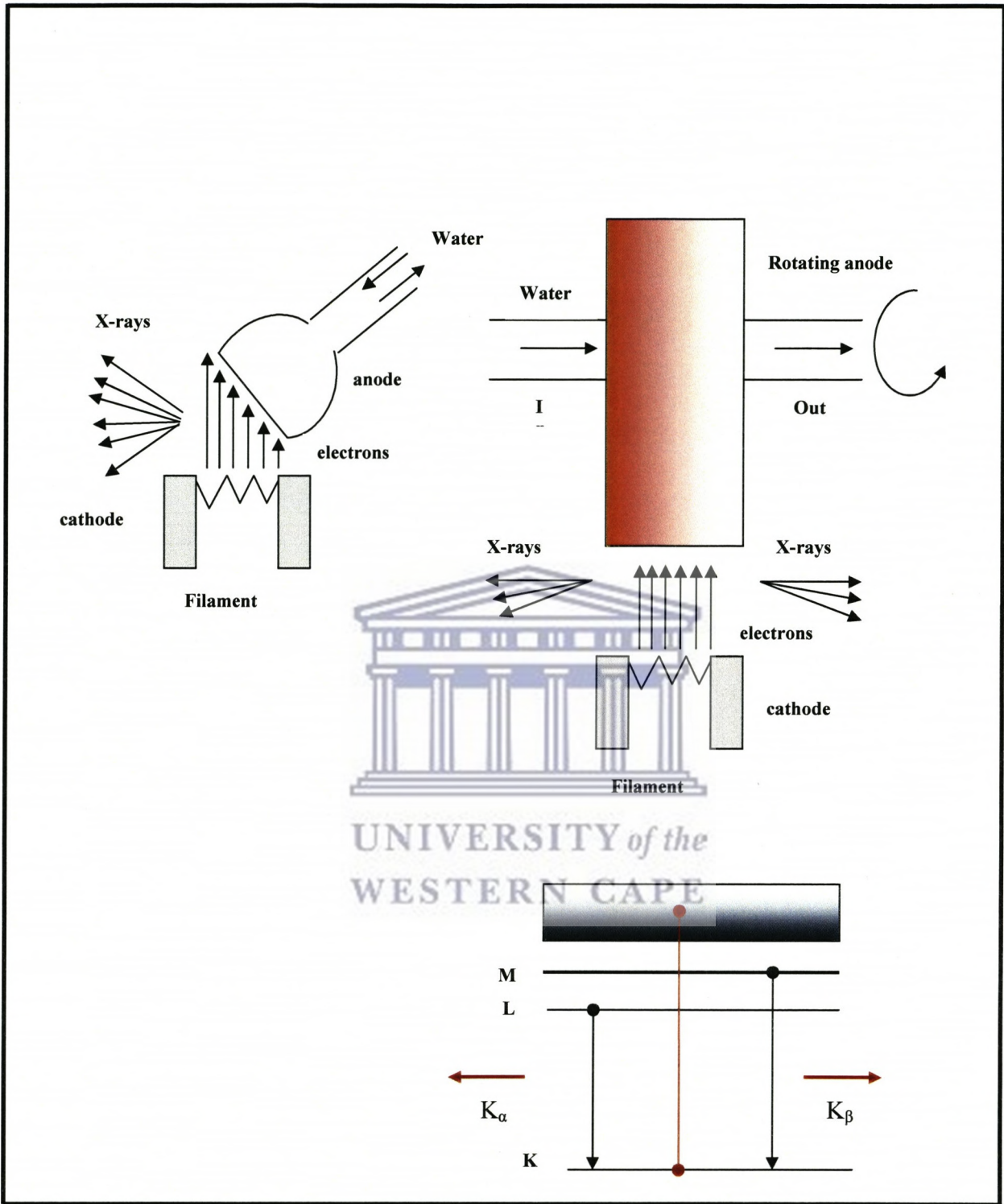
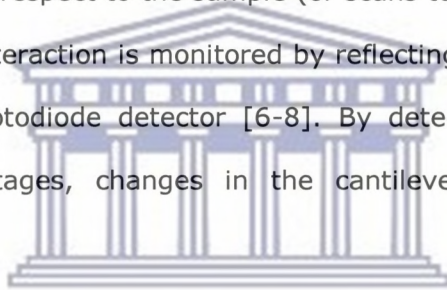


**Figure 5.3:** Scheme of generation of X-rays.

## 5.2 Atomic Force microscopy

Since the invention of AFM by Binnig et al [5] in 1986, high resolution three-dimensional maps of surfaces have been achieved. AFMs probe the sample and make measurements in three dimensions  $x$ ,  $y$ , and  $z$  (normal to the sample surface), thus enabling the presentation of three-dimensional images of a sample surface. AFM consists of scanning a sharp tip on the end of a flexible cantilever across a sample surface while maintaining a small constant force. An integrated silicon tip can be seen in figure 5.4. The tips typically have an end radius of 2 nm to 20 nm, depending on the tip type. The scanning motion is conducted by a piezoelectric tube scanner which scans the tip in a raster pattern with respect to the sample (or scans to the sample with respect to the tip). The tip-sample interaction is monitored by reflecting a laser off the back of the cantilever into a split photodiode detector [6-8]. By detecting the difference in the photodetector output voltages, changes in the cantilever deflection or oscillation amplitude are determined.



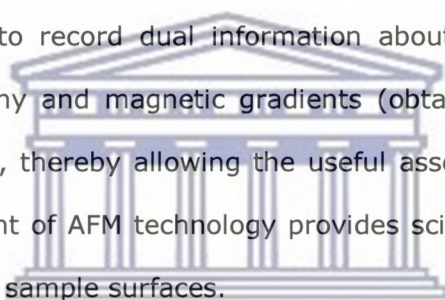
UNIVERSITY of the  
WESTERN CAPE

A schematic of this can be seen in figure 5.4 below. The two most commonly used modes of operation are contact mode AFM and Tapping mode AFM, which are conducted in air or liquid environments. Contact mode AFM consists of scanning the probe across a sample surface while monitoring the change in cantilever deflection with the split photodiode detector. A feedback loop maintains a constant cantilever deflection by vertically moving the scanner to maintain a constant photodetector difference signal [9].

The distance the scanner moves vertically at each  $x$ ,  $y$  data point is stored by the computer to form the topographic image of the sample surface. This feedback loop maintains a constant force during imaging, which typically ranges between 0.1 to 100 nN. Tapping mode AFM consists of oscillating the cantilever at its resonance frequency

(typically  $\sim 300$  KHz) and lightly “tapping” on the surface during scanning. The laser deflection method is used to detect the root-mean-square (RMS) amplitude of cantilever oscillation [9]. A feedback loop maintains constant oscillation amplitude by moving the scanner vertically at every  $x, y$  data point. Recording this movement forms the topographical image [9].

The advantage of Tapping mode with respect to contact mode is that it eliminates the lateral, shear forces present in contact mode. This enable Tapping mode to image soft, fragile, and adhesive surfaces without damaging them, which can be a drawback of contact mode AFM. The third imaging mode of AFM is the Lift mode AFM, which provides the operator with a tool to record dual information about a sample surface at one location such as topography and magnetic gradients (obtained in the magnetic force microscopy or MFM mode), thereby allowing the useful association of the two images. The continuing development of AFM technology provides scientists with a powerful tool to characterize a variety of sample surfaces.



UNIVERSITY of the  
WESTERN CAPE

Minimal sample preparation, use in ambient conditions, and the ability to image non-conducting specimens at atomic scale (in some cases) make AFM an extremely versatile and useful form of microscopy. Recent advances in AFM have allowed the successful imaging of polymeric and biological samples and imaging of magnetic microstructures. Figure 5.5 shows the atomic force microscopy (AFM) which is a nanoscope IIIa digital instruments incorporated within the tapping mode AFM unit at iThemba LABS for the imaging of the surface morphology and roughness of the samples.

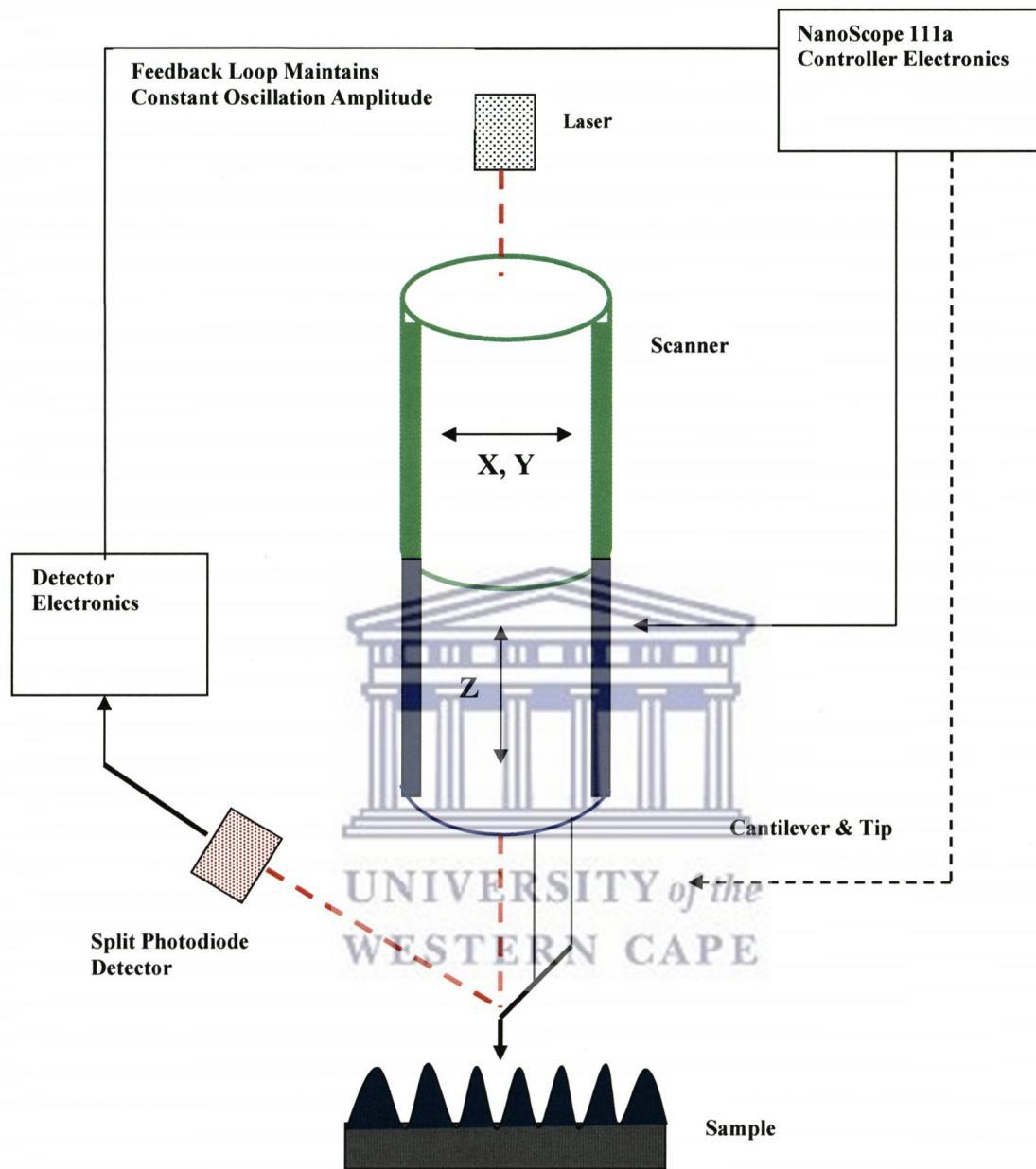


**Figure 5.4:** Schematic diagram of the major components of the AFM showing the feedback loop for TappingMode operation.



**Figure 5.5:** AFM unit at iThemba LABS used for the imaging of the surface morphology and roughness of the samples.



## 5.3 Raman Spectroscopy

### 5.3.1 Introduction

Raman spectroscopy is a spectroscopic technique based on inelastic scattering of monochromatic light, usually from a laser source. Inelastic scattering means that the frequency of photons in monochromatic light changes upon interaction with a sample [10]. Photons of the laser light are absorbed by the sample and then reemitted. Frequency of the reemitted photons is shifted up or down in comparison with original monochromatic frequency, which is called the Raman effect [10]. This shift provides information about vibrational, rotational and other low frequency transitions in molecules. Raman spectroscopy can be used to study solid, liquid and gaseous samples.

### 5.3.2 Origins of Raman phonon modes

The Raman effect is based on molecular deformations in electric field  $E$  determined by molecular polarization  $\alpha$  [10]. The laser beam can be considered as an oscillating electromagnetic wave with electrical vector  $E$ . Upon interaction with the sample, it induces electric dipole moment  $P = \alpha E$  which deforms molecules. Because of periodical deformation, molecules start vibrating with characteristic frequency  $\nu_m$ .

Amplitude of vibration is called a nuclear displacement. In other words, monochromatic laser light with frequency  $\nu_0$  excites molecules and transforms them into oscillating dipoles [10]. Such oscillating dipoles emit light of three different frequencies as shown in Figure 5.6 and 5.7 when:

- A molecule with no Raman-active modes absorbs a photon with frequency  $\nu_0$ . The excited molecule returns back to the same basic vibrational state and emits light

with the same frequency  $\nu_0$  as an excitation source. This type of interaction is called an elastic Rayleigh scattering.

- A photon with frequency  $\nu_0$  is absorbed by Raman-active molecule which at the time of interaction is in the basic vibrational state. Part of the photon's energy is transferred to the Raman-active mode with frequency  $\nu_m$  and the resulting frequency of scattered light is reduced to  $\nu_m - \nu_0$ . This Raman frequency is called Stokes frequency, or just "Stokes" [10].
- A photon with frequency  $\nu_0$  is absorbed by a Raman-active molecule, which, at the time of interaction, is already in the excited vibrational state. Excessive energy of excited Raman active mode released, molecule returns to the basic vibrational state and resulting frequency of scattered light goes up to  $\nu_m + \nu_0$ . This Raman frequency is called Anti-Stokes or just "Anti-Stokes".

About 99.999% of all incident photons in spontaneous Raman undergo elastic Rayleigh scattering. This type of signal is useless for practical purposes of molecular characterization. Only about 0.001% of the incident light produces inelastic Raman signal with frequencies  $\nu_0 \pm \nu_0$ .

Spontaneous Raman scattering is very weak and special measures should be taken to distinguish it from the predominant Rayleigh scattering. Instruments such as notch filters, tunable filters, laser stop apertures, double and triple spectrometric systems are used to reduce Rayleigh scattering and obtain high quality Raman spectra.

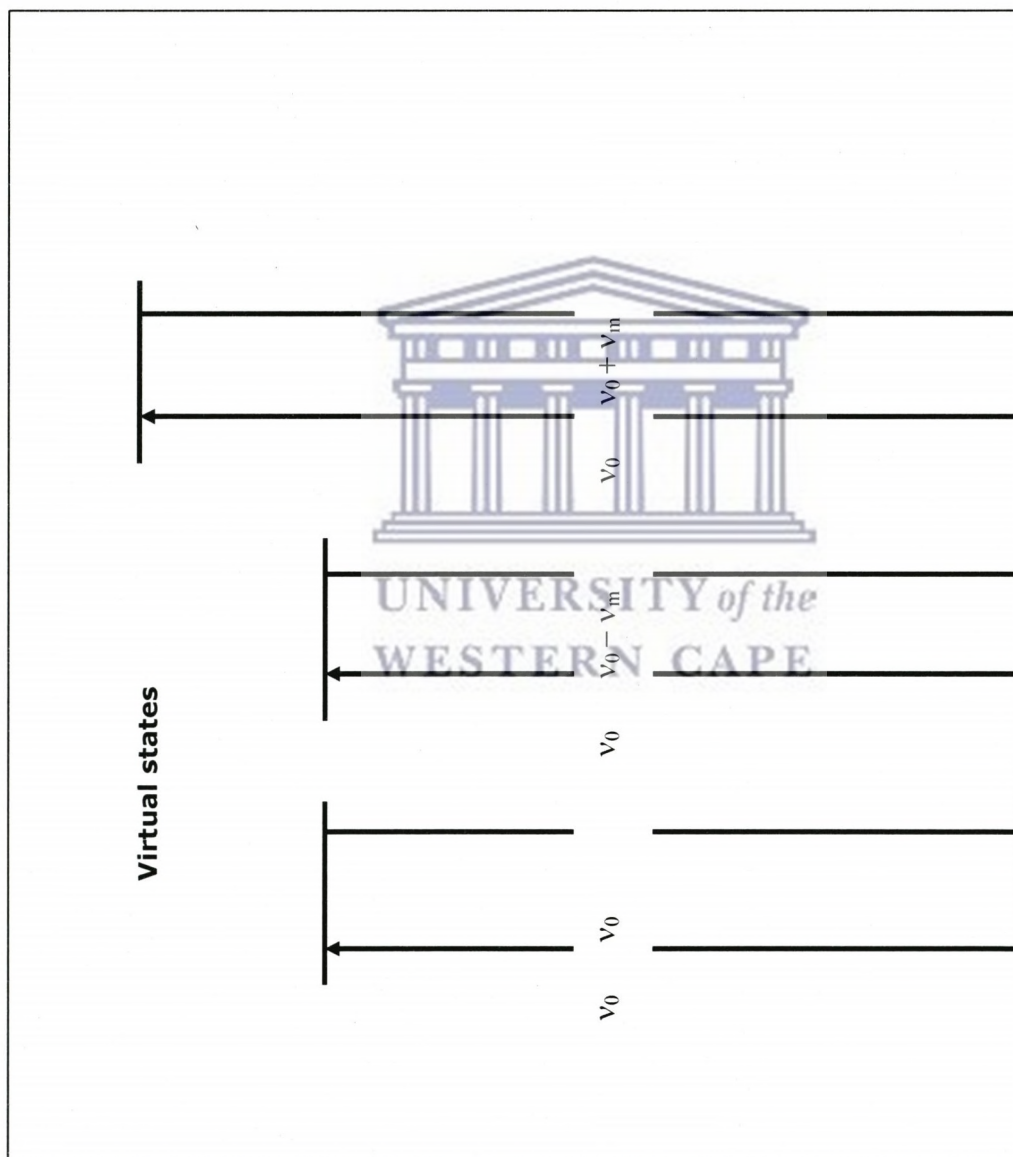


**Figure 5.6:** Raman virtual states.

### 5.3.3 Instrumentation

A Raman system typically consists of four major components:

- Excitation source (Laser).
- Sample illumination system and light collection optics.
- Wavelength selector (Filter or spectrophotometer).
- Detector (Photodiode array, CCD or PMT)

A sample is normally illuminated with a laser beam in the ultraviolet (UV), visible (Vis) or near infrared (NIR) range. Scattered light is collected with a lens and is sent through interference filter or spectrophotometer to obtain a Raman spectrum of a sample. Since spontaneous Raman scattering is very weak the main difficulty of Raman spectroscopy is separating it from the intense Rayleigh scattering. More precisely, the major problem here is not the Rayleigh scattering itself, but the fact that the intensity of stray light from the Rayleigh scattering may greatly exceed the intensity of the useful Raman signal in the close proximity to the laser wavelength. In many cases the problem is resolved by simply cutting off the spectral range close to the laser line where the stray light has the most prominent effect.

Many researchers use commercially available interference (notch) filters which cut-off spectral range of  $\pm 80\text{-}120\text{ cm}^{-1}$  from the laser line. This method is efficient in stray light elimination but it does not allow detection of low-frequency Raman modes in the range below  $100\text{ cm}^{-1}$ . Stray light is generated in the spectrometer mainly upon light dispersion on gratings and strongly depends on grating quality. Raman spectrometers typically use holographic grating which normally have much less manufacturing defects in their structure than the ruled ones. Stray light produced by holographic gratings is about an order of magnitude less intense than from ruled gratings of the same groove density. Using multiple dispersion stages is another way of stray light reduction. Double and

triple spectrometers allow taking Raman spectra without use of notch filters. In such systems Raman-active modes with frequencies as low as  $3\text{-}5\text{ cm}^{-1}$  can be efficiently detected. It is reported that in earlier times scientists primarily used single-point detectors such as photon-conducting Photomultiplier Tubes (PMT) [11].

However, a single Raman spectrum obtained with PMT detector in wavenumber scanning mode was taking substantial period of time, slowing down any research or activity based on Raman analytical technique. Today, more and more often researchers use multi-channel detectors like Photodiode Arrays (PDA) or, more commonly a Charge-Coupled Devices (CCD) to detect the Raman scattered light. Sensitivity and performance of modern CCD detectors are rapidly improving. In many cases CCD is becoming the detector of choice for Raman spectroscopy.

Raman spectroscopy data of the samples were collected using a T64000 micro-Raman spectrometer from HORIBA Scientific, Jobin Yvon Technology equipped with a triple monochromator system to eliminate contributions from the Rayleigh line. All the samples were analysed with a 514 nm Argon excitation laser (12 mW at laser exit to avoid thermal effects), a  $\times 50$  objective with recording times ranging between 120s and a resolution of  $2\text{cm}^{-1}$ .

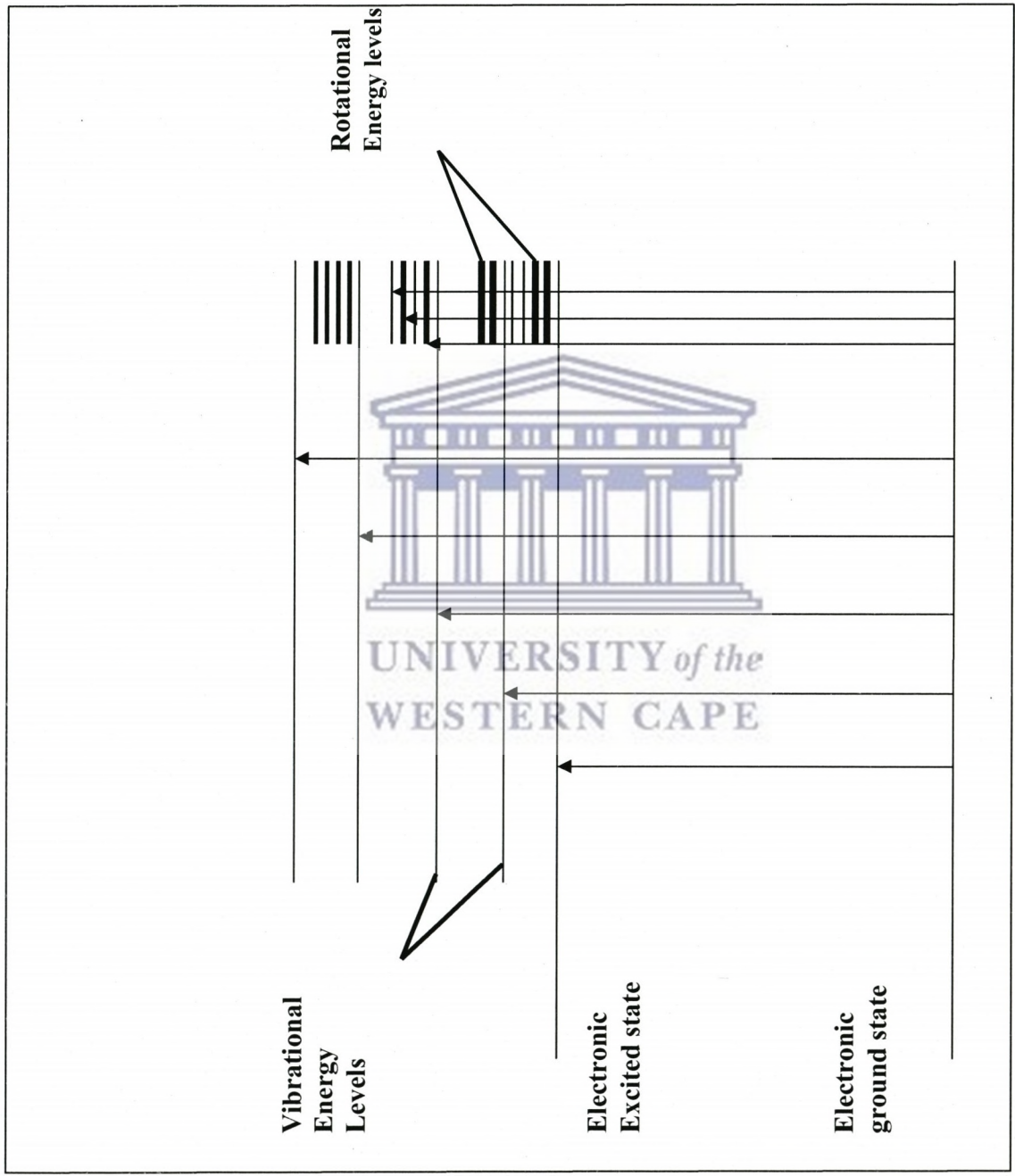


**Figure 5.7:** Electronic energy levels and transitions.

## 5.4 Photoluminescence

Photoluminescence (PL) is a powerful and relatively simple method, extensively used as characterization technique of semiconductor physics for a number of reasons:

- It is non-destructive because it is based on pure optical processes.
- No sample preparation is required
- Highly sensitive
- Detailed information on the electronic structure in the semiconductor can be deduced from the experiments.

Information that could be deduced from PL study includes the size of the band gap, impurity levels, interface, and surface properties as well as density of states and excitonic states. Basically in PL measurements, a semiconductor sample is optically excited by an excitation source such as a laser which produces photons having energies larger than the band gap of the semiconductor. The incident photons are absorbed under creation of electron-hole pairs in the sample. After a short time the electrons eventually recombine with the holes, to emit photons, and light or luminescence will emerge from the sample. The energy of the emitted photons reflects the energy carrier in the sample. The emitted luminescence is collected, and intensity is recorded as a function of the emitted photon energy, to produce a PL spectrum. In a PL measurement, the excitation energy is kept fixed, while the detection energy is scanned. The energy of emitted photon is characteristic for radiative recombination process. PL technique is particularly helpful in the analysis of discrete defect and impurity states.

### 5.4.1 Radiative recombination mechanisms observed in PL.

In semiconductors, the luminescence can be achieved by several radiative transitions between the conduction band and valence band, exciton, donor and acceptor levels, as

shown in figure 5.9. Upon excitation at energy above the band gap, free electrons are created in the conduction band together with the free holes in the valence band. These carriers will energetically relax down the band edge. Due to mutual coulomb interaction, electron-hole pair is formed. This electron-hole is usually called a free exciton (FE). Its energy is slightly smaller than the band gap energy. This energy difference is binding energy of the free exciton.

A neutral donor (acceptor) will give rise to an attractive potential, free exciton might be captured at the acceptor (donor) and a bound exciton is formed (BE). Another possibility is that a hole bound to an acceptor recombines with an electron bound to a donor in donor-acceptor pair (DPA) transition [12-13]. Both the donor and the acceptor are neutral before the recombination (i.e. the donor positively and the acceptor negatively charged). Thus there is a Coulomb interaction between the donor and acceptor after transition and extra Coulomb energy is gained in the final state added to the radiative recombination energy. The transition energy  $E$  depends on the distance  $R$ , between the donor and acceptor atoms. Micro-photoluminescence spectroscopy High spatial resolution is gained in the micro-PL by replacing the lens focusing the laser on the sample by a microscope objective. The microscope objective offers possibility to focus the laser spot down to  $2\mu\text{m}$  in diameter and gives the value up to  $\mu\text{m}$  precision in the sample position. The focusing of light is managed by moving the objective, while the cryostat, which makes possible measurement at very low temperature, is adjusted vertically and horizontally to change the position of the excitation spot. A magnified image of the sample is taken from the CCD-chip of a video camera, allowing precise control of laser focusing and sample position.



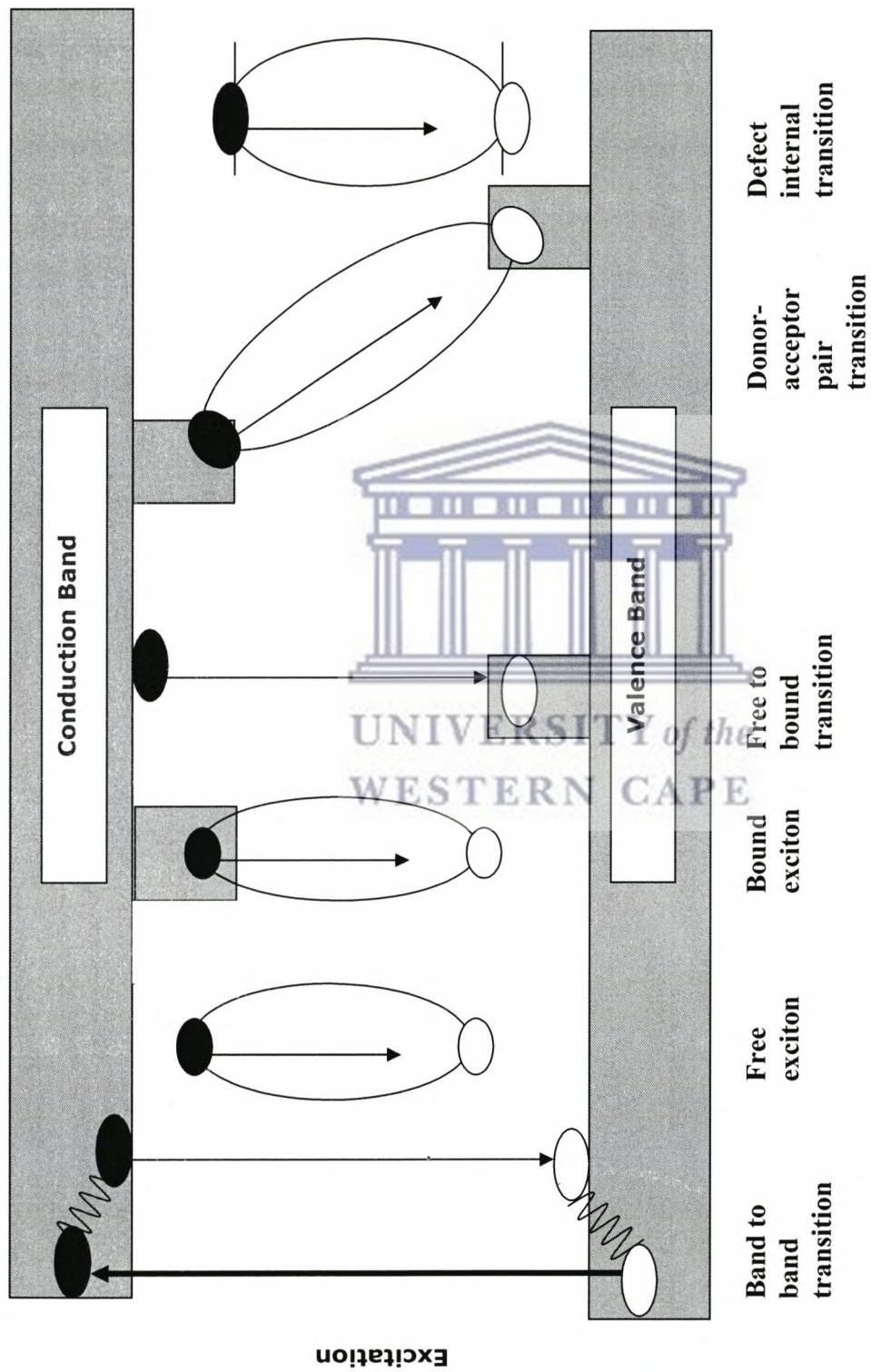


**Figure 5.8:** Schematic illustration of common recombination processes.

### **5.4.2 Experimental setup**

The experimental setup consists of an excitation source, cryostat, microscope objective, monochromator, CCD-TV camera and additional components.

### **5.4.3 Excitation source**

Excitation source is usually a laser, which provides a stable and well defined source of the monochromatic light. The fourth harmonic of CW Nd: Vanadate laser (226) was used in our measurements.

### **5.4.4 Cryostat**

The cryostat is used to cool the sample to a low temperature. The sample is mounted inside the continuous He-flow close to the glass window. This allows adjusting microscope objective at the focal point of the microscope to get the smallest laser spot size (1 $\mu$ m). Vacuum pump was used to decrease the pressure above the helium surface and the temperature varied from 2-300K.

### **5.4.5 Microscope Objectives**

The microscope objective, outside the cryostat is used for both focusing laser light excite and collect the emitted light from the sample. By using beam splitters and mirrors the collected light is guided to spectrometer and detector.

### **5.4.6 Monochromator**

The monochromator was used to choose wavelength that will reach the detector at the exit of slit of the monochromator. We used single monochromator 0.55 m with 2400 gratings with a spectral resolution <0.2 meV at 360 nm.

### 5.4.7 Video camera

Video camera is used for obtaining an image of the surface on the monitor. This is achieved by illuminating the sample with white light lamp through the microscope objective and detecting light from the sample. The camera helps us to locate the sample and guarantees that we are measuring at the same sample position. The camera also shows the laser spot and helping in obtaining the optimal alignment of the setup.

## 5.5 References

- [1] B. D. Cullity, Elements of X-ray Diffraction, 2<sup>nd</sup> edn, Addison Wesley, Reading, MA. 1978.
- [2] B. L. Dutrow. Louisiana State University. M. C. Clark. Eastern Michigan University. X-ray powder diffraction
- [3] R. Jenkins, X-ray techniques:overview, Encyclopedia of analytical chemistry, R. A. Meyers (Ed.) (2000) 13269–13288
- [4] G. Gauglitz, T. Vo-Dinh, The Handbook of spectroscopy Wiley-VCH, ISBN 3-527-29782-0, (2003),1000
- [5] G. Binning, C. F. Quate, Ch. Gerber. Atomic force microscope. Phys. Rev. Lett. 56 (9), (1986) 930.
- [6] V. Clemente, K. Gloystein, Principles of atomic force microscopy, Physics of advanced materials winter school, (2008).
- [7] Park Scientific Instruments. A practical guide to scanning probe microscopy. (1997).
- [8] N. Yao, Z. L. Wang. Handbook of Microscopy for Nanotechnology. (2005).
- [9] Veeco. Scanning Probe Microscopy Training Notebook. Version 3.0. (2000).
- [10] [http://content.piacton.com/Uploads/Princeton/Documents/Library/UpdatedLibrary/Raman\\_Spectroscopy\\_Basics.pdf](http://content.piacton.com/Uploads/Princeton/Documents/Library/UpdatedLibrary/Raman_Spectroscopy_Basics.pdf): Princeton instruments; Raman Spectroscopy Basics.
- [11] Photomultiplier Handbook, Supersedes PMT-62, 8-80 Printed in U.S.A./ 10-89
- [12] N. F. Mott, E. A. Davis Electronic Process in Non-crystalline Materials, Bristol, (1979)
- [13] W. E. Spear et P. G. Le Comber, Solid St. Comm., 17 1193 (1975)

## CHAPTER 6

### 6 RESULTS AND DISCUSSIONS

---

#### 6.1 Samples

In this study, we have used high-quality n-type 6H-SiC samples with orientation (0001) and the thickness of about 363  $\mu\text{m}$ . The 6H-SiC (0001) wafers were grown by Cree in USA by employing the sublimation method in which SiC powder is sublimated under low pressure and high temperature and allowed to crystallize on a seed crystal at the top of the growth chamber maintained at a slightly lower temperature.

#### 6.2 Irradiation

Small pieces of about  $1 \times 1 \text{ cm}^2$  were cut from the purchased samples and were irradiated with reactor neutrons,  $\gamma$ -rays and protons. Here prior to irradiation we have use chemical reagents like soap solution, methanol, acetone, trichloroethylene, acetone methanol and De-ionised water for cleaning the cut substrates.

Chart for the Substrate cleaning process with alcohol

Ultrasonicate with methanol (5 minutes two times)



then Ultrasonicate 5 minutes with Acetone



then Ultrasonicate by Trichloroethylene and then by Acetone (5 minutes each time)



then Ultrasonicate by Methanol and then by De-ionized water (5 minutes each time)

### 6.2.1 Reactor neutrons irradiation

Four pieces were first enrobed with high purity Aluminium wafer then separately inserted in a well sealed container made of Aluminium, and irradiated at different neutrons fluencies. The irradiation parameters are given in table 6.1.

We note that sample 1 was irradiated at NUR research reactor of Nuclear Research Center of Draria (CRND), Algiers, at a position where the temperature is less than 40°C. Whereas the samples 2, 3 and 4 were irradiated at Es-Salam heavy water (HWRR) research reactor of, Nuclear Research Center of Berine (CRNB).

### 6.2.2 $\gamma$ -rays irradiation

The irradiation for  $\gamma$ -rays were performed at room temperature using the Co-60 source of Nuclear research Center of Algiers (CRNA) with an average energy of 1.25 MeV. Four samples were irradiated at different doses as reported in table 6.1.

### 6.2.3 Protons irradiation

A hexagonal 6H-SiC single crystal wafers (363  $\mu\text{m}$  thick,  $1 \times 1 \text{ cm}^2$ ) were bombarded with a 2 MeV protons up to a dose of approximately  $7.17 \times 10^{16} \text{ H}^+/\text{cm}^2$  in a Van de Graaff accelerator at iThemba LABS national facility, South Africa. A homogeneous circular beam 1 mm in diameter is used. This experiment is conducted at room temperature at different doses. Each sample is mounted onto stainless-steel samples holder and can hold about ten samples.

The sample holder is then inserted in the beam tube followed by the evacuation of the chamber (base pressure  $\sim 5 \times 10^{-5}$  mbar).

Sample	Thermal Neutron Fluence (n.cm <sup>-2</sup> )	Fast Neutron Fluence (En > 1.2 MeV) (n.cm <sup>-2</sup> )	γ-ray (KGy)	Proton(MeV)
1	5.8 x 10 <sup>17</sup>	3.2x 10 <sup>17</sup>	200	0.5
2	6.1 x 10 <sup>18</sup>	2.4x 10 <sup>17</sup>	500	1
3	6.7 x 10 <sup>18</sup>	3.4 x 10 <sup>17</sup>	1000	1.5
4	8.8 x 10 <sup>18</sup>	4.4x 10 <sup>17</sup>	1200	2



**Table 6.1:** The irradiation experimental details.

The proton beam is magnetically analyzed, shaped, and steered prior to its entry into the target chamber. After irradiation, system is brought back to atmospheric pressure before the chamber is opened for the samples removal.

A proton beam current ( $I_b$ ) of approximately 50 nA is stepped across the target area at an offset angle of 45°. The samples are offset in order to increase the time of interaction of the charged particle inside the layer, since this is the region of interest.

The irradiation parameters are also given in table 6.1.

### **6.3 RESULTS AND DISCUSSIONS**

In this section, we report on the damages and/or defects induced by the various irradiation sources on 6H-SiC, namely: Neutrons, Gamma rays ( $\gamma$ -rays) and Protons. The dependence of structural, morphological and optical properties on the effect of irradiation is discussed. The structures of the non-irradiated and irradiated samples were studied using X-ray diffraction analysis (XRD), Raman spectroscopy and the surface morphology using Atomic Force Microscopy (AFM). The optical properties evolution after irradiation, were investigated using Photoluminescence spectroscopy (PL).

#### **6.3.1 Effect of Neutrons and $\gamma$ -rays irradiation**

##### **6.3.1.1 X-ray diffraction**

Figure 6.1.a reports the corresponding XRD profiles of the typical of the non-irradiated sample of 6H-SiC. The figure 6.1a shows two set of diffraction peaks at low and higher angle: one at 36.65° and another one at 76.8°. The first one can be attributed to the (006) planes of 6H-SiC, while the second can be due to (0012) planes of 6H-SiC and concur with the diffraction peaks of hexagonal 6H-SiC (JCP2.cat: 00-002-1463).

The diffraction patterns acquired in Bragg-Brentano (BB) configuration of the neutrons irradiated samples compared to the non-irradiated sample are shown in Figure 6.1b, reporting on the evolution of the main plane (0012). As shown in figure 6.1b (0012) pattern of the irradiated samples are practically equal to that of the non-irradiated sample revealing that no preferential orientation of the crystal grain or the formation of other SiC polytypes structures that have been induced by irradiation.

Also from figure 6.1b there is a slight displacement of the (0012) peak position revealing that there is small change in structural properties within increasing the fast neutron fluence as the position of the (0012) have shifted to high angle and the shift becomes more pronounced at the higher neutron fluence of  $4.4 \times 10^{17} \text{ n.cm}^{-2}$ . This indicates that the used fast neutron fluence is too small to induce very pronounced defects or the swelling of the samples and higher fluence are necessary to see swelling or amorphization of the samples. Snead et al. [1], investigated the effects of neutron irradiation on single crystalline 6H-SiC and polycrystalline 3C-SiC up to a fluence of  $2.6 \times 10^{25} \text{ n/cm}^2$ . Amorphization is observed for both materials with a reduction in density of 10.8% [1].

In figure 6.1c, we are reporting the peak position evolution as function of the  $\gamma$ -rays dose used to irradiate the 6H-SiC samples. We notice also that there is no much effect of the  $\gamma$ -ray irradiation on the samples structural properties as there were no others peaks appearing. At the same time we notice there is only a shift that appears for the sample irradiated with 200 Gky.

As a comparison the effect of fast neutrons and thermal  $\gamma$ -ray fluencies were not significant to induced defects in the 6-H-SiC samples. And higher fluencies are needed to induce very pronounced defects.



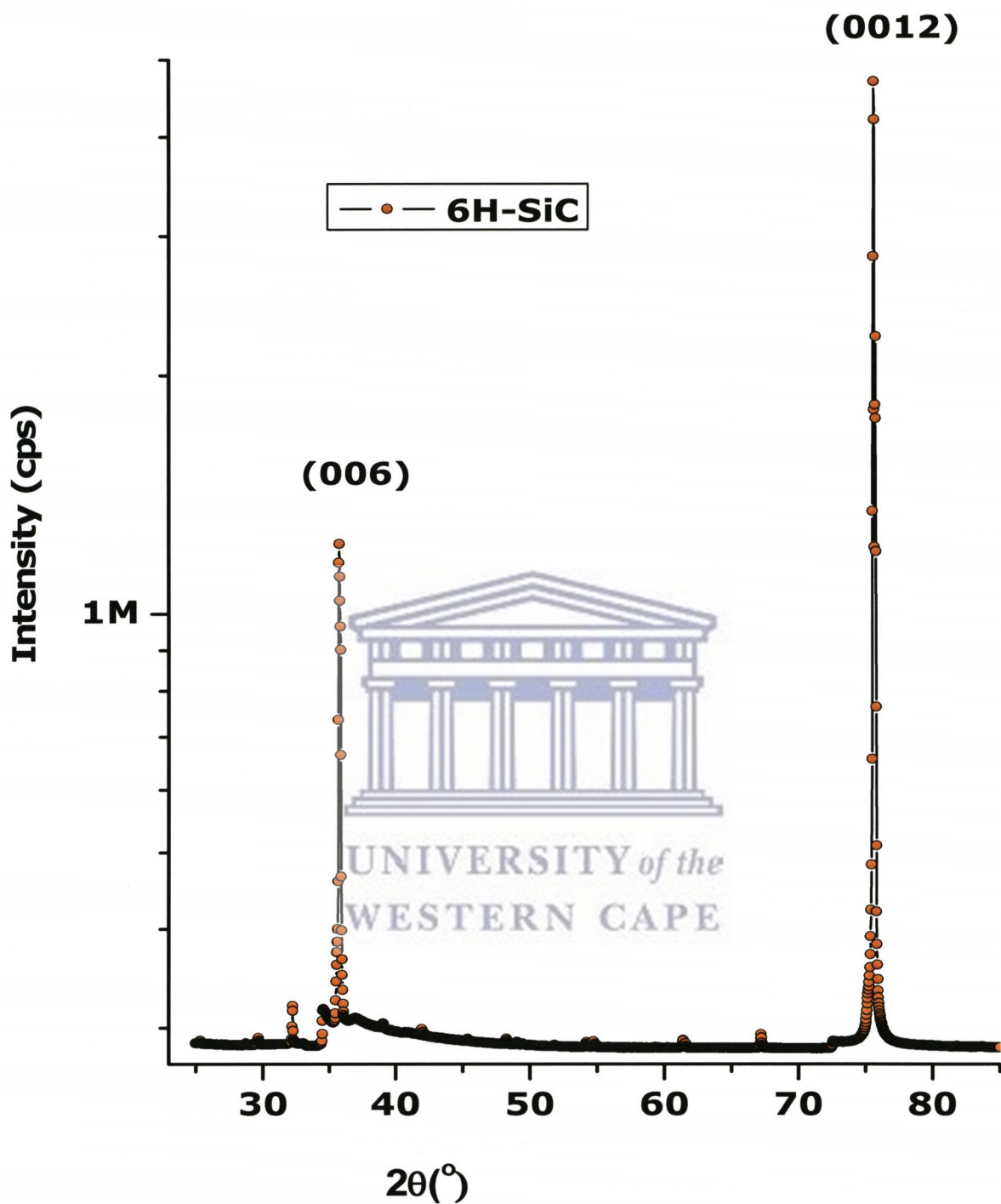


**Figure 6.1.a:** XRD patterns in BB configuration of the non-irradiated samples of 6H-SiC.

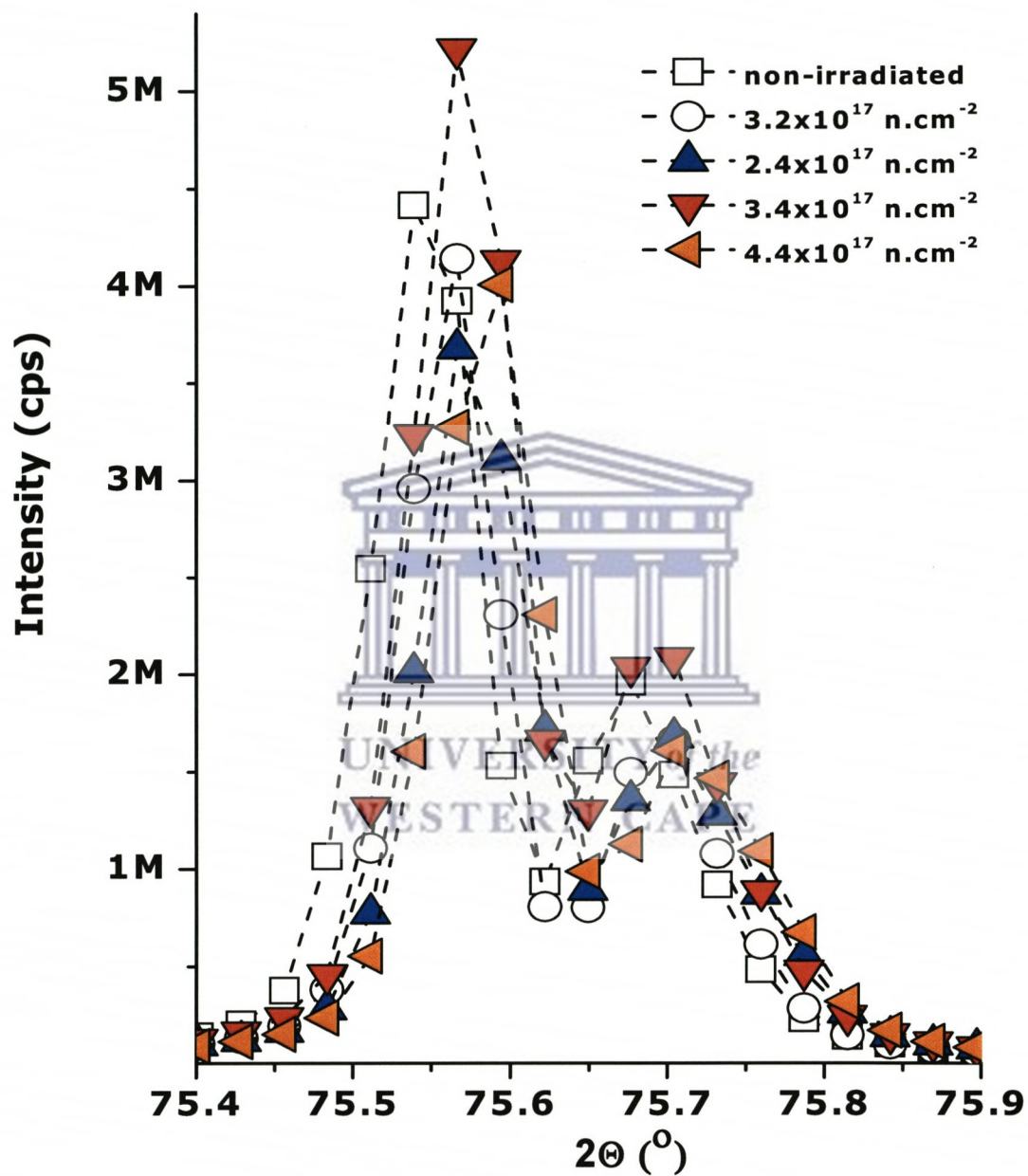


**Figure 6.1b:** (0012) XRD pattern in BB configuration evolution with the neutrons irradiation dose.

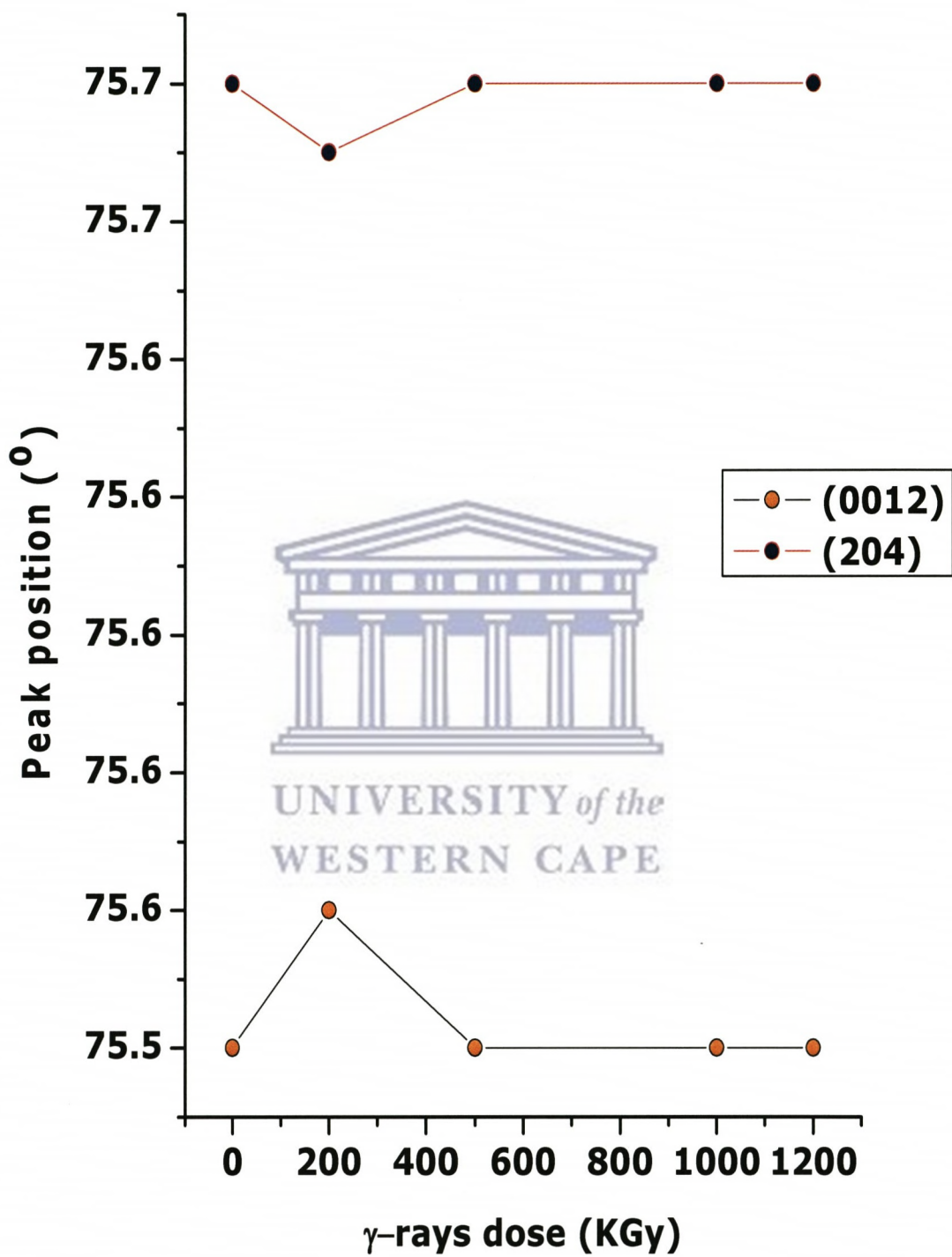


**Figure 6.1c:** peak position for irradiated and non-irradiated samples of SiC.

### 6.3.1.2 Raman spectroscopy

After XRD structural investigation of the neutrons and  $\gamma$ -rays irradiation of the 6H-SiC samples; Raman spectroscopy analysis were used as a complementary technique.

Figure 6.2a Shows spectrum of 6H-SiC sample as function of fast neutron irradiation fluence. Figure 6.2a reveals several phonons Raman lines assigned to different acoustic and optic phonons (longitudinal and transverse) of different symmetries.

6H-SiC has a wurtzite structure with  $C_{6v}$  space group. The Raman active modes are A1, E1 and E2 symmetry. The following modes which characterize the Raman lines are clearly observed in the non-irradiated sample of 6H-SiC. The mode at  $766\text{ cm}^{-1}$  to that of E2 (TO) [2] while, the sharp modes appearing at  $787\text{ cm}^{-1}$  and  $965\text{ cm}^{-1}$  phonon frequencies, can be related to the contribution of E2 (FTO) and A1 (LO), respectively [3]. The identified phonon modes give a signature of all the strong and weak Raman active modes of 6H-SiC.

For the sake of clearness, we have chosen to analyze only two ( $766$  and  $787\text{ cm}^{-1}$ ) of the three characteristic Raman lines in the [1000]-direction ( $765$ ,  $788$ , and  $965\text{ cm}^{-1}$ ) of the sample. The TO phonon line at  $765\text{ cm}^{-1}$  is known to remain in highly damaged samples and it was depicted to quantify the Si-C bond. Figure 6.2b shows the Raman shift at  $787\text{ cm}^{-1}$  for fast neutron irradiated and non-irradiated 6H-SiC samples. We observe a remarkable difference on the  $787\text{ cm}^{-1}$  mode for all the fast neutrons irradiated samples from the non-irradiated sample signature.

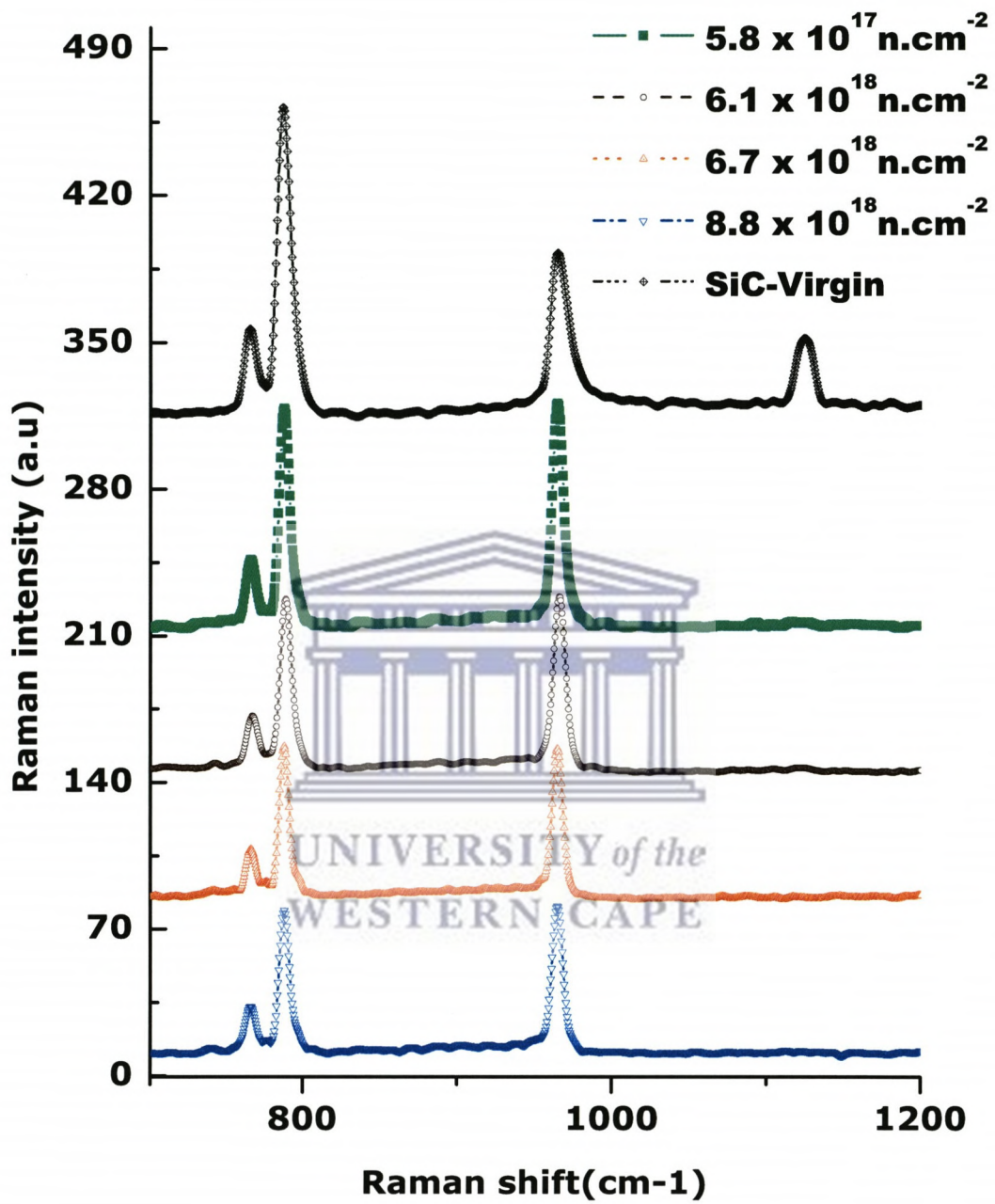


**Figure 6.2a:** Raman spectra from 750 cm<sup>-1</sup> to 1200 cm<sup>-1</sup> for irradiated and non-irradiated samples.

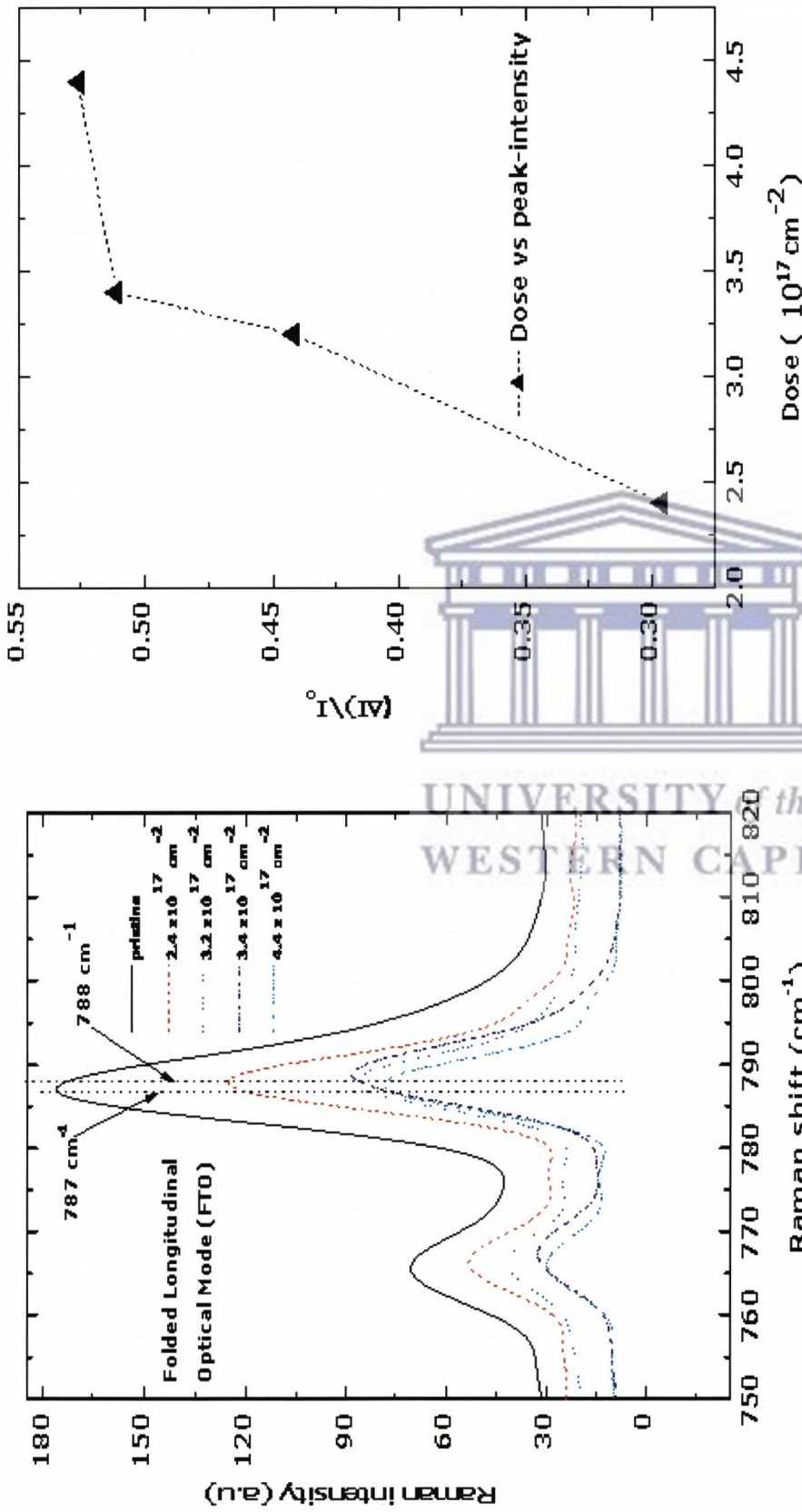


**Figure 6.2b:** Raman spectra from 750 cm<sup>-1</sup> to 820 cm<sup>-1</sup> and non-irradiated samples.

**Figure 6.2c:** The relative Intensity (RI) of the Folded irradiated Transversal Optical (FTO) mode versus irradiation dose.

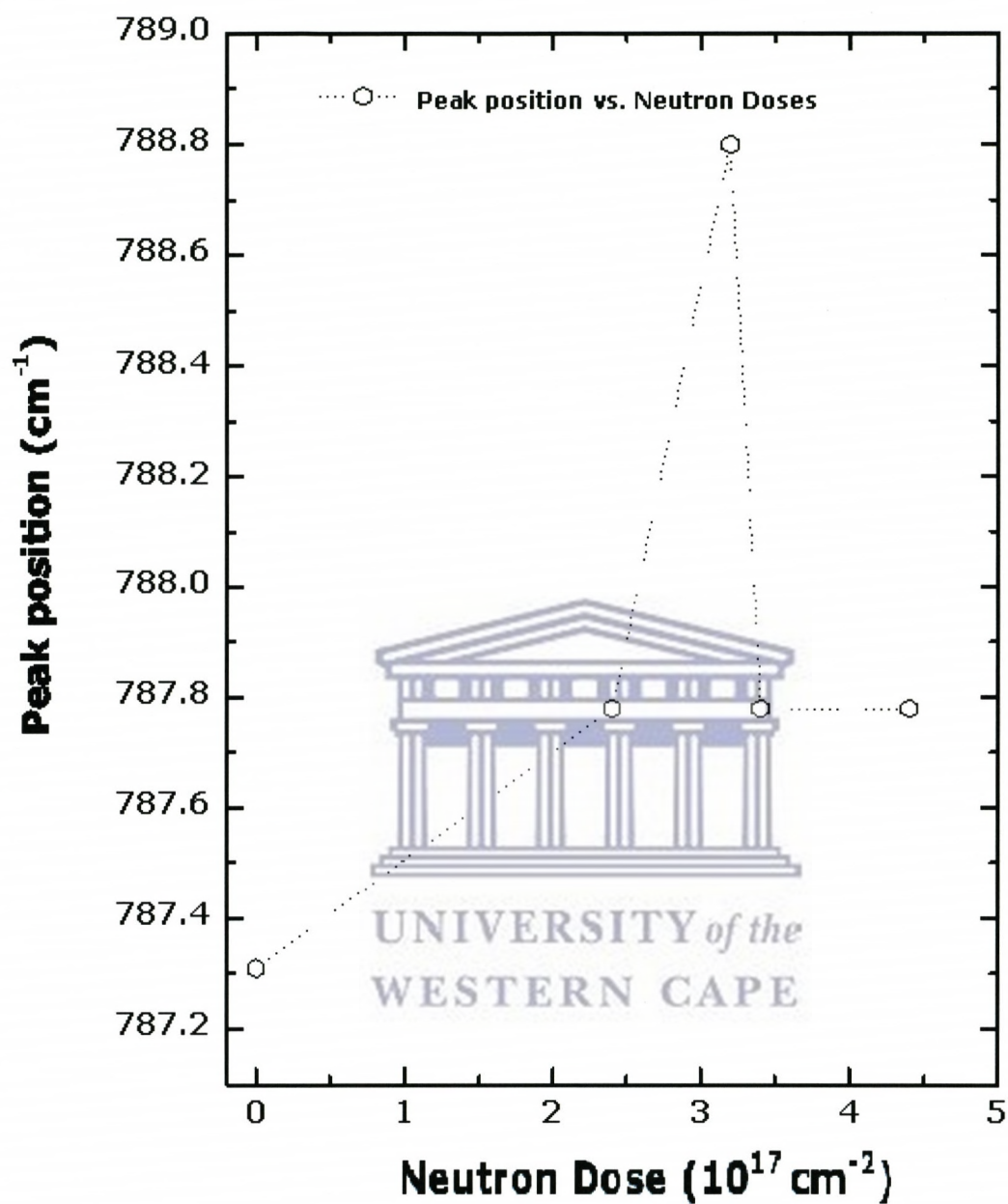
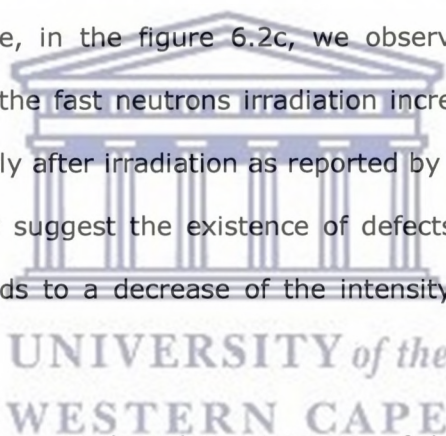


**Figure 6.2d:** Raman peak position for the Folded Transversal Optical (FTO) mode versus irradiation dose on 6h- SiC.

To further probe the accuracy of our conclusive analysis of Figure 6.2b, we have chosen to use Raman E2 (FTO) mode at  $787\text{ cm}^{-1}$  for monitoring and analyzing the fast neutrons radiation effect and to further backup our observation. By doing so, we will be able to extract evidence that will backup our analysis. Figure 6.2c displays the relative intensity variation of the folded transversal optical (FTO) mode at  $787\text{ cm}^{-1}$  given by  $(1-I/I_0)$  vs fast neutrons fluence, where  $I_0$  and  $I$  are the intensities of the peak measured in the non irradiated and irradiated samples, respectively. We have used the described approach above based on the work done by A. Pérez-Rodríguez et al. [4].

In our results as reported in figure 6.2c, one can recognize clearly that the intensity of the Raman lines decreases with the increase in the neutrons fluence, thus indicating a loss of crystalline quality. Clearly here, in the figure 6.2c, we observe the patterns showing a decrease in the intensity with the fast neutrons irradiation increases and the peak around  $1120\text{ cm}^{-1}$  disappears completely after irradiation as reported by figure 6.2a. Such a change in the raman relative intensity suggest the existence of defects or crystal lattice damage [4]. Damage in the lattice leads to a decrease of the intensity of the first order modes, related to atomic disorder.



In addition to the observed change in the relative intensity of the peaks, in figure 6.2d, we observe clearly the shift in Raman frequency in all the irradiated samples to a higher frequency between  $0.8 - 1\text{ cm}^{-1}$ . This change in Raman frequencies is related to the structural stress of the crystal lattice. The samples irradiated with  $3.2 \times 10^{17}\text{ n.cm}^{-2}$  fast neutrons have shown a shift in frequency from its natural position from  $787\text{ cm}^{-1}$  to a higher frequency of  $787.81\text{ cm}^{-1}$ , which means it has shifted by  $\sim 0.8\text{ cm}^{-1}$ . While the sample irradiated at  $2.4 \times 10^{17}\text{ n.cm}^{-2}$  has shown a phonon vibrational frequency shift from  $787\text{ cm}^{-1}$  to  $788.8\text{ cm}^{-1}$  position due to increase in the radiation fluence.



The Raman peak at  $520\text{ cm}^{-1}$  in SiC which is due to the presence of c-Si clusterization was not seen, while the peaks at  $765\text{ cm}^{-1}$ ,  $785\text{ cm}^{-1}$  and  $965\text{ cm}^{-1}$  which are due to 6H-SiC were present. Therefore no Silicon or carbon clusterization was detected in the samples after irradiation.

In figure 6.2e and figure 6.2f the Raman spectra of the different samples irradiated with different  $\gamma$ -rays fluences, are showed where in the figure 6.2f have been limited to the spectral range of  $750\text{ cm}^{-1}$  to  $820\text{ cm}^{-1}$  to evaluate the effect of the irradiation on the transversal optical phonons of the 6H-SiC crystal.

From the spectra showed it is possible to evaluate the carbon clusterization in the samples from the intensity of its Raman peak which usually appears around  $1450\text{ cm}^{-1}$  [5]: in all irradiated samples there is no appearance of such peak, indicating that the carbon clusterization, if present, is now lower than Raman detection limit. The Raman peak at  $520\text{ cm}^{-1}$  that is due to the presence of c-Si clusterization is not also seen in the samples which mean there is no c-Si clusterization.

The frequencies of the folded transversal and longitudinal phonon modes for the acoustic (FTA) and optical (FTO) branches of the dispersion curves of 6H-SiC have been investigated by Nakashima et al. [6]. In contrast with the increase in the irradiation dose, sample irradiated at room temperature, the Raman spectra did not present the strong broadening peaks located near  $500\text{ cm}^{-1}$ ,  $800\text{ cm}^{-1}$  and  $1400\text{ cm}^{-1}$  in their results.

In our data the Raman results demonstrated that there was no amorphous layer in the  $\gamma$ -ray irradiated sample, consistent with the result of XRD. Moreover, three sharp lines were observed at  $767\text{ cm}^{-1}$ ,  $789\text{ cm}^{-1}$  and  $967\text{ cm}^{-1}$  in the wave number range  $650\text{ cm}^{-1}$  to  $1150\text{ cm}^{-1}$ . The  $767\text{ cm}^{-1}$  and  $789\text{ cm}^{-1}$  lines are assigned to E2 (TO) and E2 (FTO) vibration modes, while the  $967\text{ cm}^{-1}$  line is assigned to A1 (LO) vibration mode.

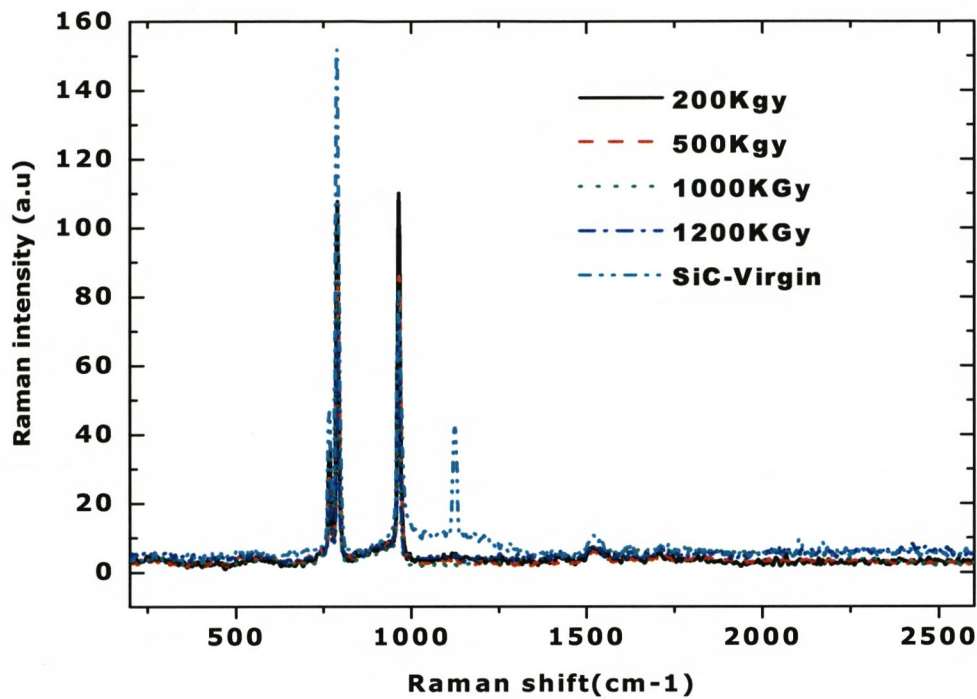


**Figure 6.2e:** Raman spectra from  $100\text{ cm}^{-1}$  to  $2200\text{ cm}^{-1}$  for irradiated and non-irradiated samples of SiC.

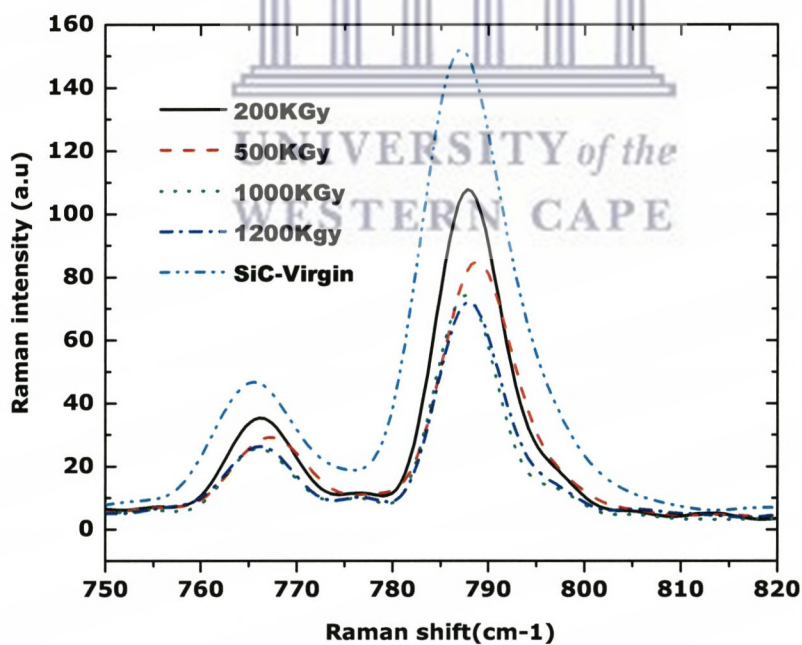


**Figure 6.2f:** Raman spectra from  $750\text{ cm}^{-1}$  to  $820\text{ cm}^{-1}$  for irradiated and non-irradiated samples of SiC.

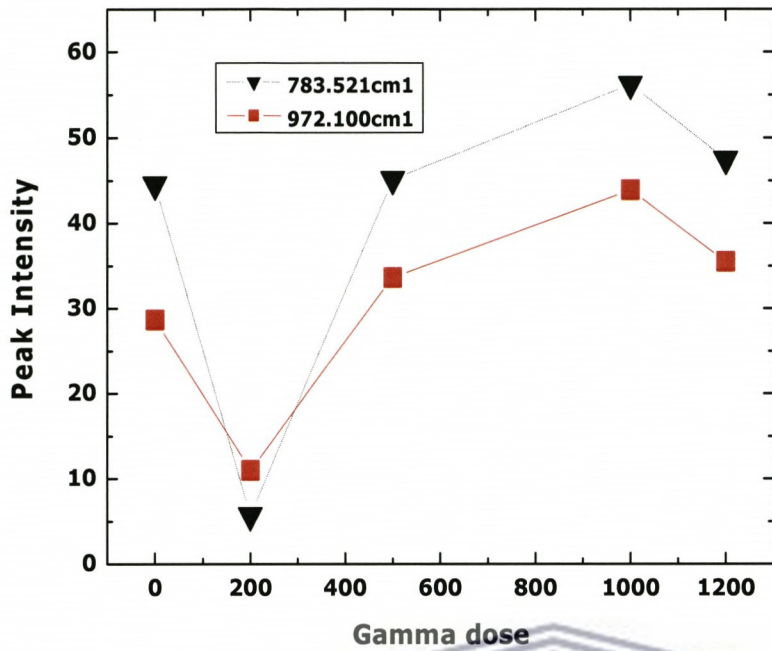


**Figure 6.2g:** The peak position of the Folded Transversal Optical (FTO) mode versus irradiation dose.

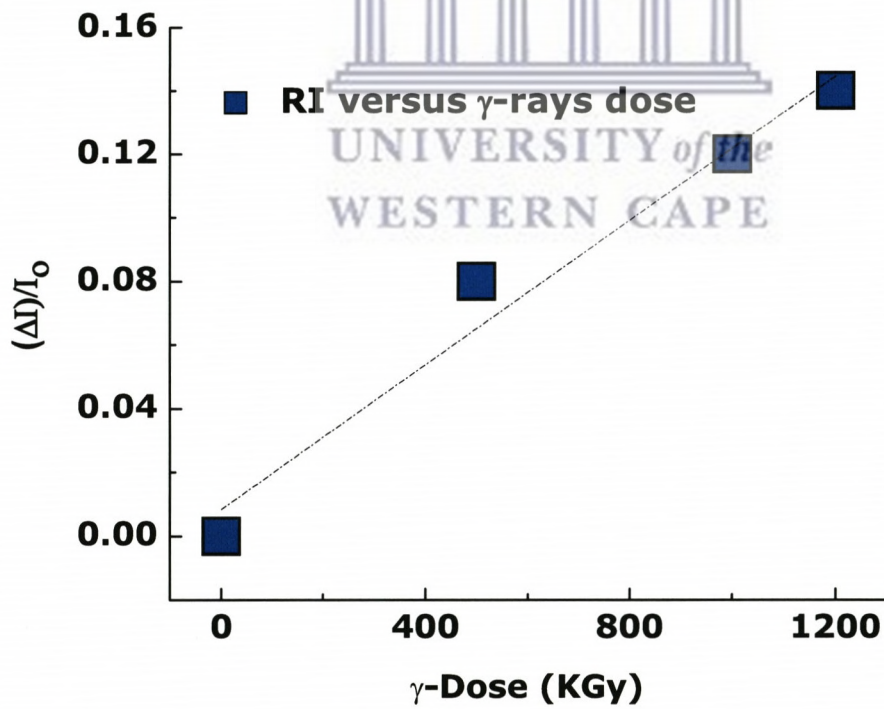


**Figure 6.2h:** The relative Intensity (RI) of the Folded Transversal Optical (FTO) mode versus irradiation dose.

The energy positions of these features in the Raman spectra were obtained by fitting Lorentzian type line profiles to the experimental data. The spectrum of E2 (FTO) phonon at  $789\text{ cm}^{-1}$  monitored the crystalline quality of the sample, as shown in Figure 6.2f. The E2 line width and its intensity as function of the  $\gamma$ -ray irradiated 6H-SiC decreased with increasing dose. The intensity of E2 line of the sample irradiated with 200 Gky was found to be lower than that of the non-irradiated sample which may be due to the large deviation between low energy  $\gamma$ -ray dose and the necessary thermal energy for lattice recovery after irradiation, please refers to fig. 6.2g. The integrated intensity  $I$  of E2 was normalized to the value  $I_0$  of the crystalline material, i.e.,  $I_{\text{norm}} = 1 - I/I_0$  please see fig.6.2h. The value of the relative intensity RI increased linearly with irradiation dose except at 200 Gky as shown in fig. 6.2g. The data were fitted by a function of an Arrhenius-type giving activation energy of  $0.175 \pm 0.003\text{ eV}$ . Raman intensity profiles of the FTA and FTO modes have been calculated for various polytypes based on bond polarizability mode [7]. The Raman intensity decreased with increasing irradiation dose, indicating the increase in defects of  $\gamma$ -ray-irradiation induced lattice damage, disarranging silicon-carbon bonds, etc. The evolution of the profile of Raman scattering spectrum was comparable to that observed for the un-irradiated 6H-SiC, indicating that the  $\gamma$ -rays induced lattice defects evolved into dilute stable defects (Figure 6.2).

We note that all vibration modes show the same behavior for all the samples irradiated. Moreover, no vibration mode assigned to Si-Si and C-C clustering was observed in our samples. Indeed, a peak centered around  $1430\text{ cm}^{-1}$  attributed to C-C bonds is observed in Raman spectrum in the case of SiC irradiated at higher fast neutrons fluence above  $1 \times 10^{20}\text{ n.cm}^{-2}$

Thus according to our data, it is clear that the crystalline structure is progressively destroyed without formation of amorphous state for both neutrons and  $\gamma$ -ray irradiations.

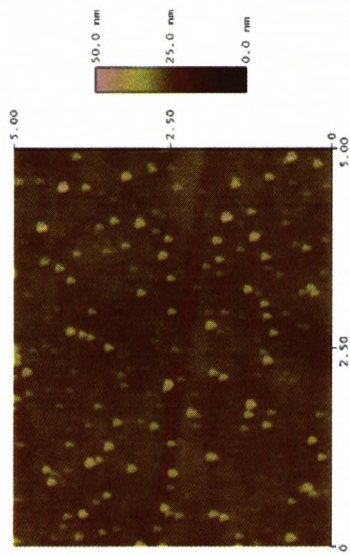
### 6.3.1.3 Morphological properties

Figure 6.3a shows AFM micrographs of non-irradiated and fast neutron-irradiated 6H-SiC samples, respectively, after irradiation at room temperature in air. It seems to be a melting formation for the surface morphology of the neutrons-irradiated 6H-SiC sample. The result shows the radiation damage due to ionizing effects (sputtering). The cluster like behavior may be attributed to the sputtering effect due to neutrons irradiations. The atoms agglomerate and coarsen into bubbles, in the neutrons- irradiated SiC have been extensively investigated and it is well known in the case of hillocks generation, so atoms are released at the surface. Atoms bubbles can deteriorate structural properties by inducing crack, creep therefore modifying the surface morphological properties of the samples.

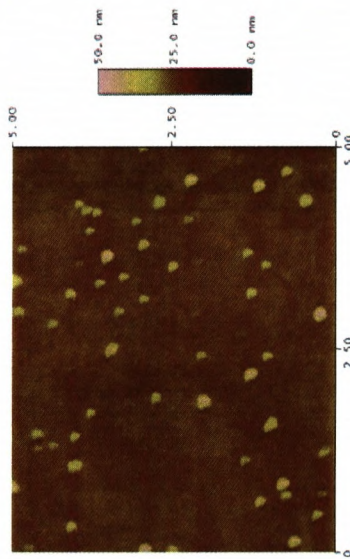
Figure 6.3b shows the surface roughness of the samples which increases with the neutrons irradiation dose. According to earlier findings [8], the surface roughness increases indicate the progressive amorphization of SiC single crystal. The increase in the surface roughness resulting from the surface modification is due to the sputtering effects during irradiation.

Evolution of surface point defects produced by  $\gamma$ -ray with increasing dose is shown in Figure 6.3c. The scattered point defects produced tend to cluster during and form defect-rich areas as we increase the  $\gamma$ -rays dose but less effect is seen compared to the neutrons irradiations.

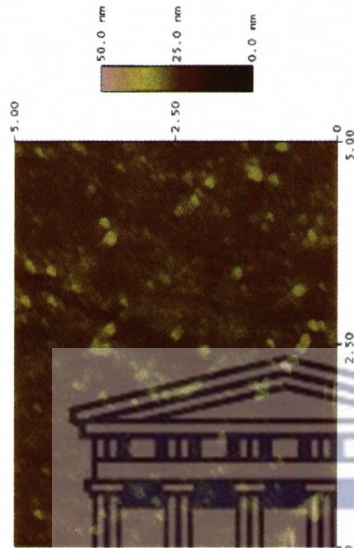
Jiang et al. also observed this phenomenon in experiment [9]. These defect-rich areas grow with irradiation dose and finally fill the whole surface and resulted into the variation of the surface roughness of the irradiated samples as shown in figure 6.3d.



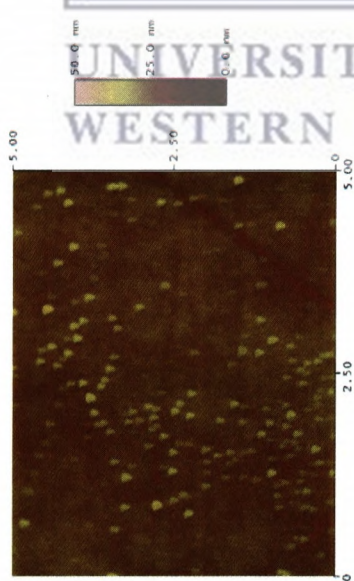
**2.4 x 10<sup>17</sup> n.cm<sup>-2</sup>**



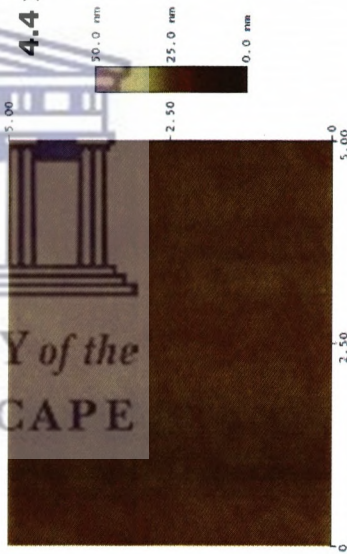
**3.2 x 10<sup>17</sup> n.cm<sup>-2</sup>**



**3.4 x 10<sup>17</sup> n.cm<sup>-2</sup>**



**4.4 x 10<sup>17</sup> n.cm<sup>-2</sup>**



**Virgin**

**Figure 6.3a:** AFM micrographs of non-irradiated and fast neutron-irradiated 6H-SiC samples.

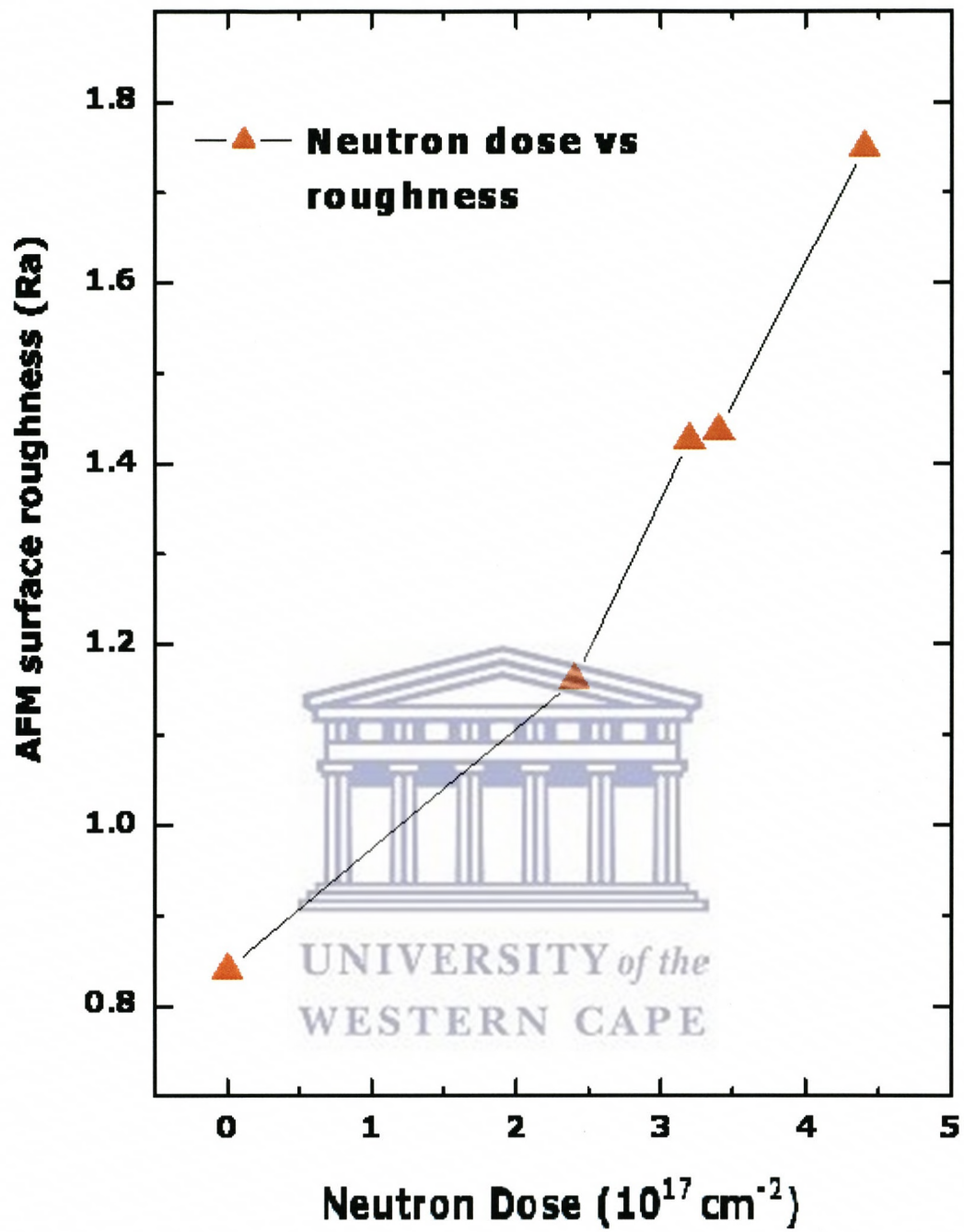


**Figure 6.3b:** Plot of the AFM surface roughness versus fast neutron fluence.

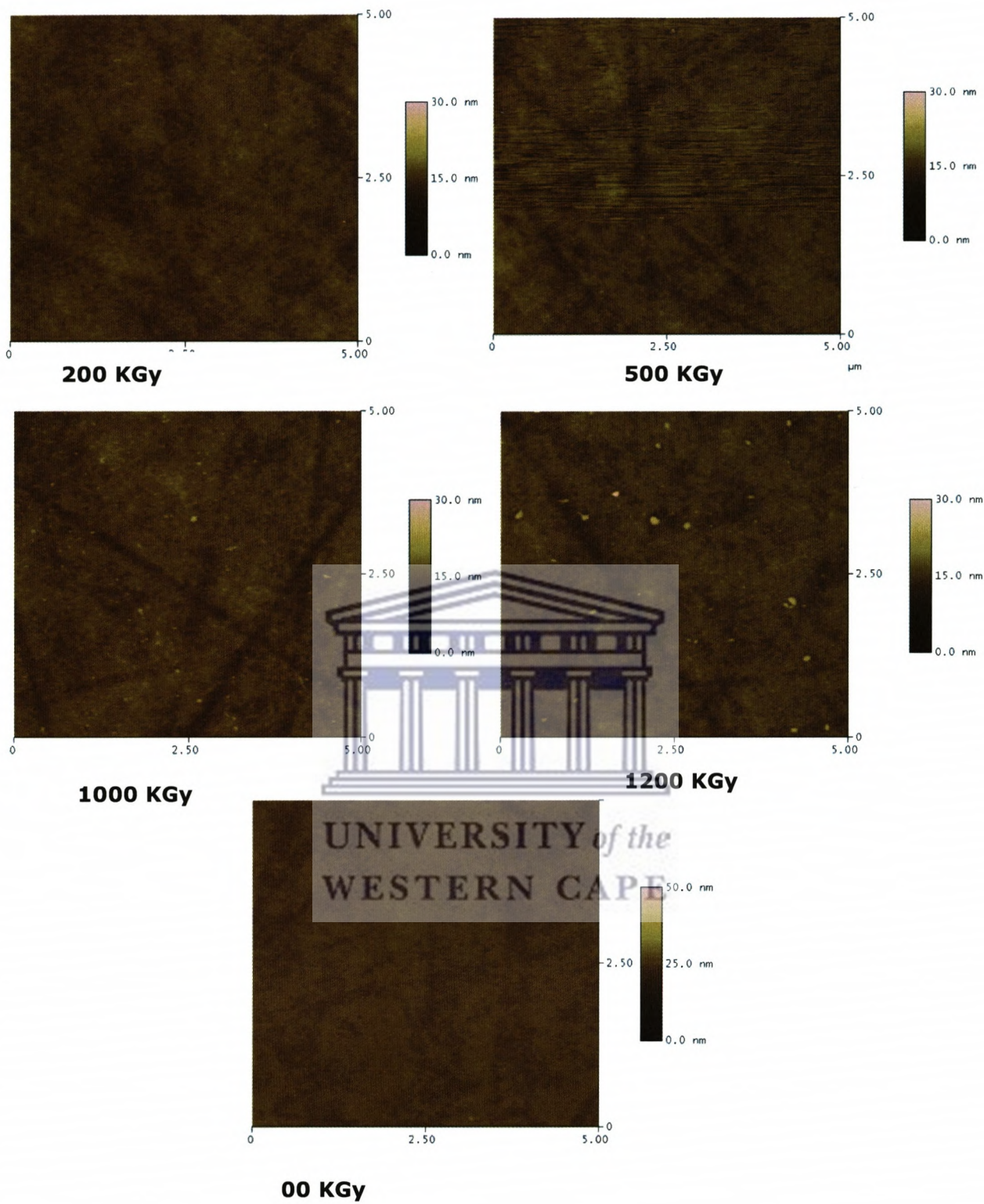


**Figure 6.3c:** AFM micrographs as a function of gamma dose.



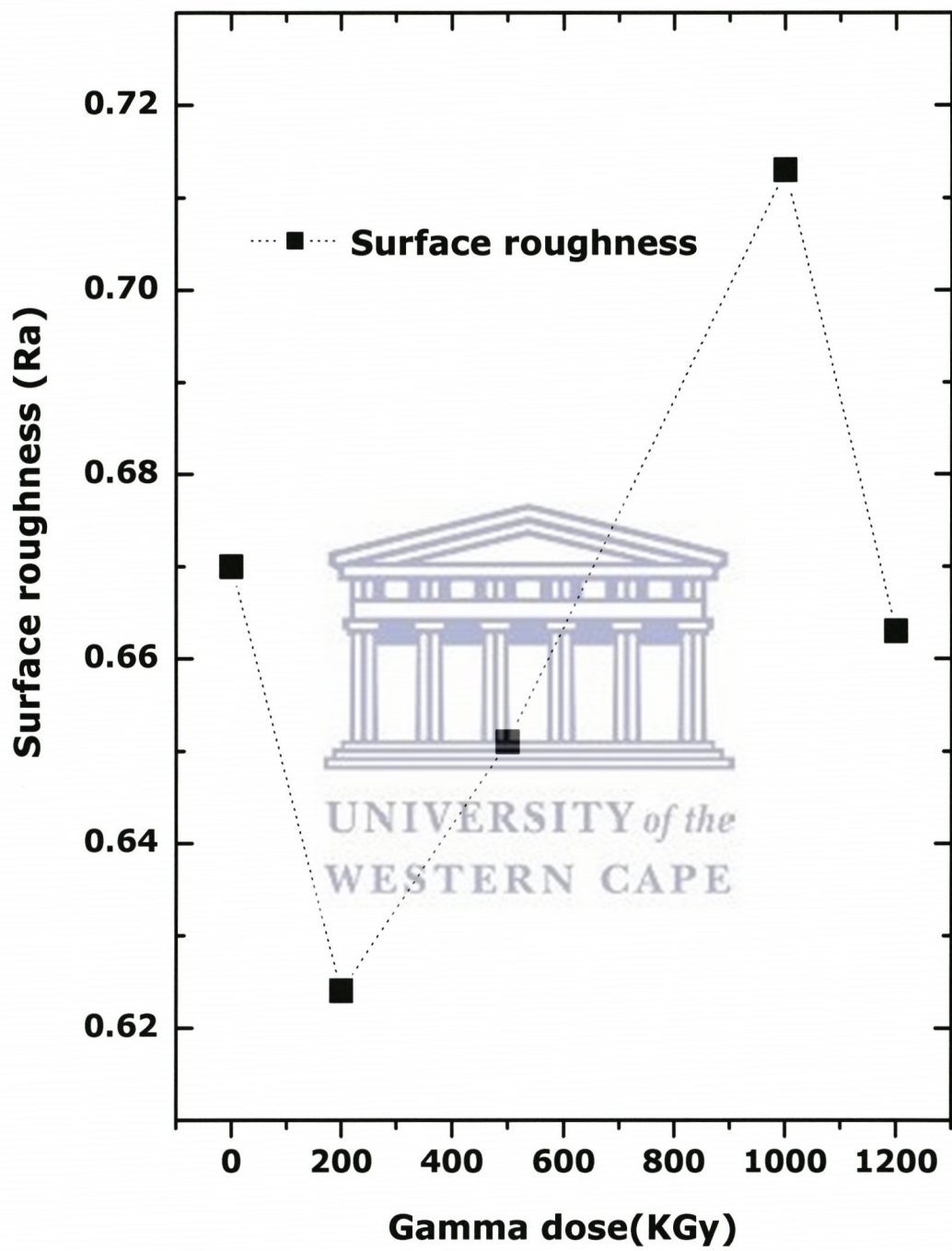


**Figure 6.3d:** AFM surface roughness as a function of gamma dose.

#### 6.3.1.4 Optical properties: Photoluminescence data analysis

Before and after irradiation the samples were analysed with photoluminescence.

The PL spectra of the non-irradiated sample is shown in Fig.6.4a and it is obviously a superposition of strongly overlapping sub-bands and could be decomposed on a set of individual components or fitted and centered into two different regions. One emission band centered at about 420 nm (2.9 eV) and a large emission band extended from 760 nm (1.6 eV). The latter band may be extended up to 1.4 eV.

Approximately the same emission bands are observed on previous work done on the PL investigation of SiC, (see ref. [10] and [11]). The superposition of strongly overlapping sub-bands (Fig. 6.4a) includes defect related PL bands with the peak positions at 1.40, 1.60, 1.82, 1.67, 1.78, 1.96, 2.39, 2.30, 2.86 and 3.27 eV.

Notice that near infrared defects PL bands intensities dominate in the spectrum.

The evolution of these emission bands as a function of the fast neutron fluence is observed in Fig. 6.4b. We can see that the infrared defects PL bands intensities which dominated in the non-irradiated samples decrease with increasing fluence this is in accordance with earlier findings in the case of alpha particle irradiation [12] and reactor neutrons [13]. After irradiation we can notice that the PL spectra of the SiC are dominated by the visible bands with the principle peak at 2.86 eV. We also observe no shift after on the bands positions after irradiation.

Upon  $\gamma$ -ray irradiation, additional photon peaks around 3.01, 2.76, and 2.63 eV, which are characteristic of induced damage centers, may become present once compared to the spectra of the non-irradiated sample and the neutron irradiated samples as shown in figure 6.4c. A comparison of pre-irradiated data with measured data after  $\gamma$ -ray irradiation is made. The optical emission spectrum of 6H-SiC can be very complex due to the existence of inequivalent lattice sites, which result in site-dependent ionization potentials for each impurity [14].

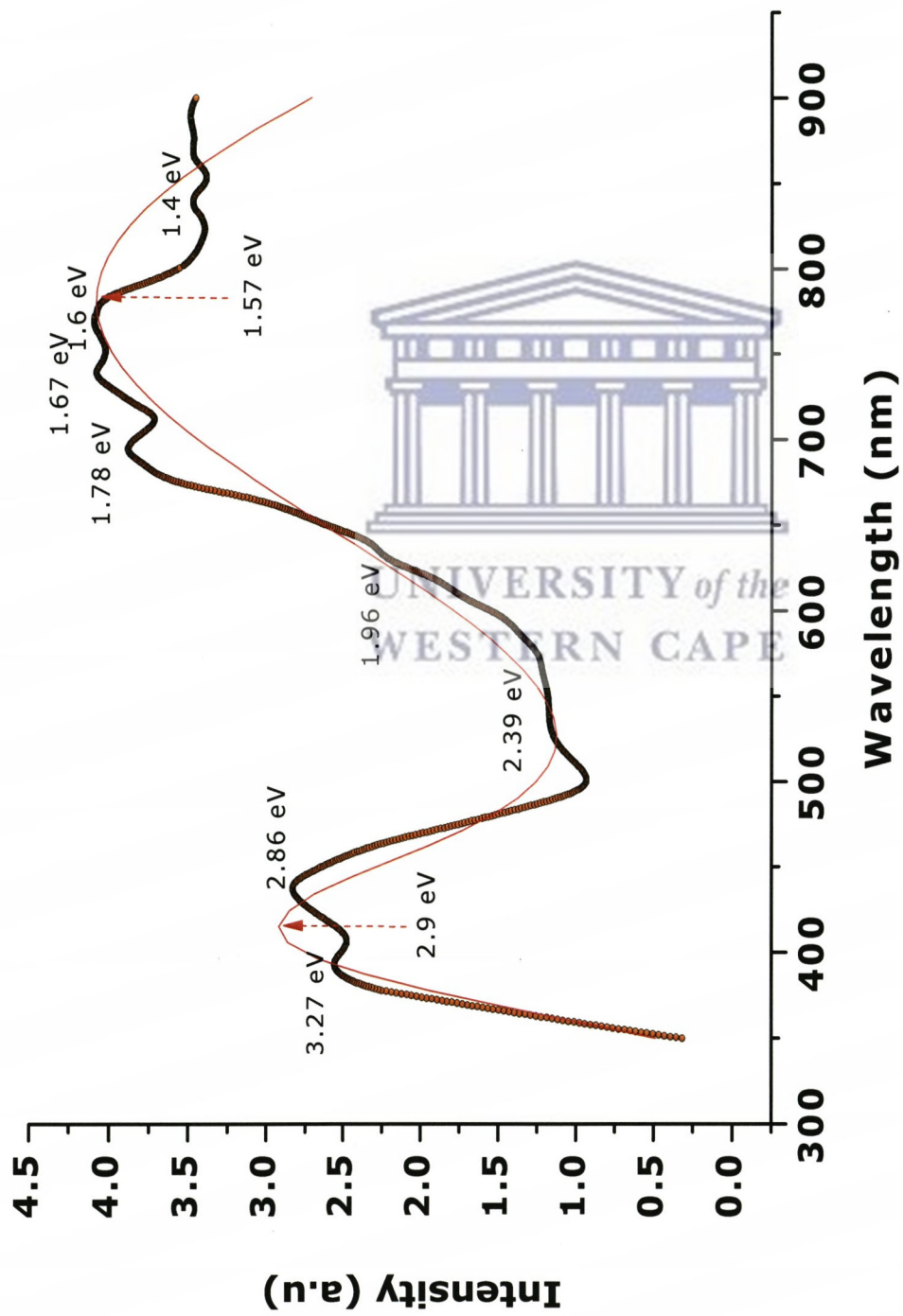


**Figure 6.4a:** Room temperature PL of the non-irradiated sample of 6H-SiC with a Lorentzian fitting.

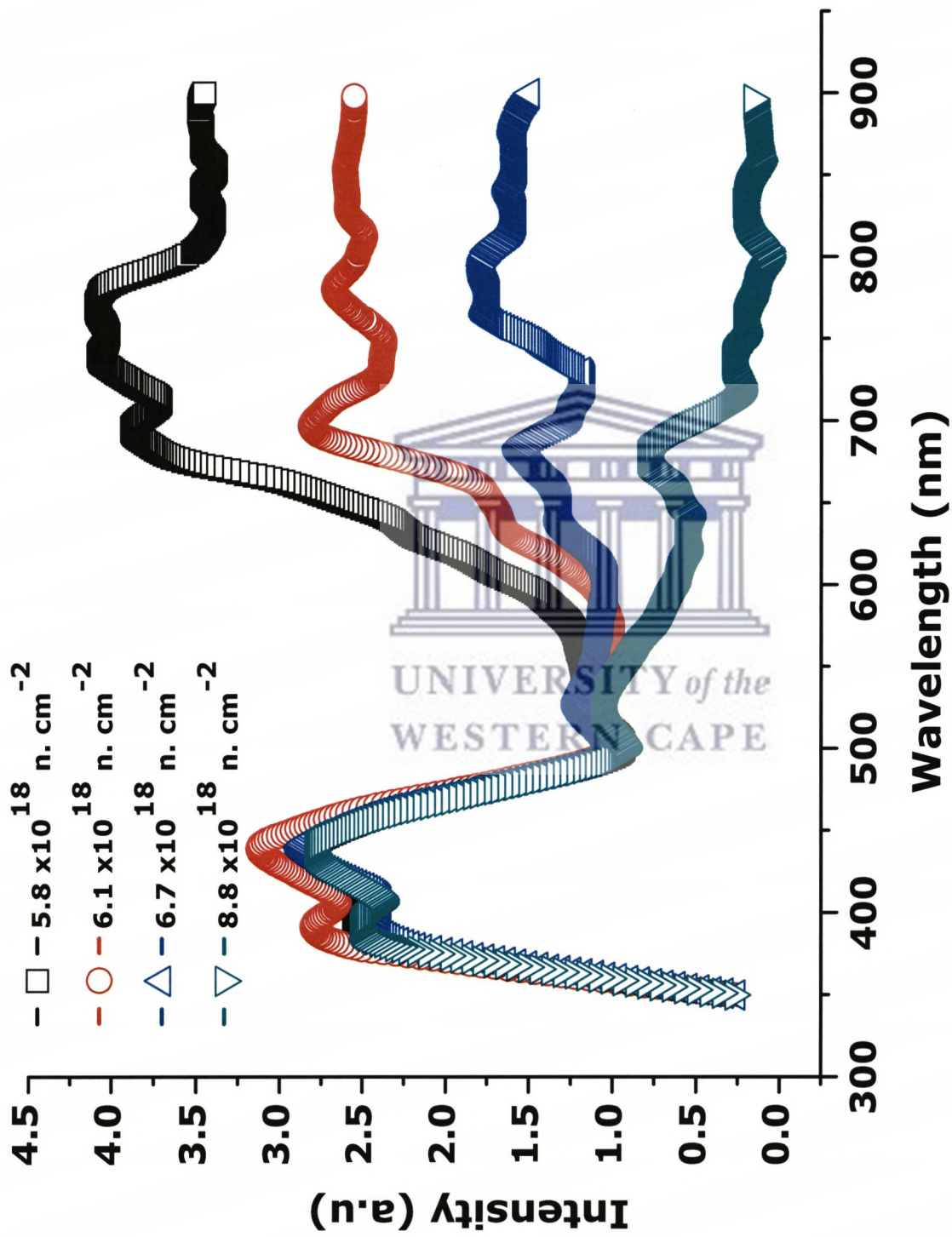


**Figure 6.4b:** Room temperature PL of neutron irradiated samples of 6H-SiC.

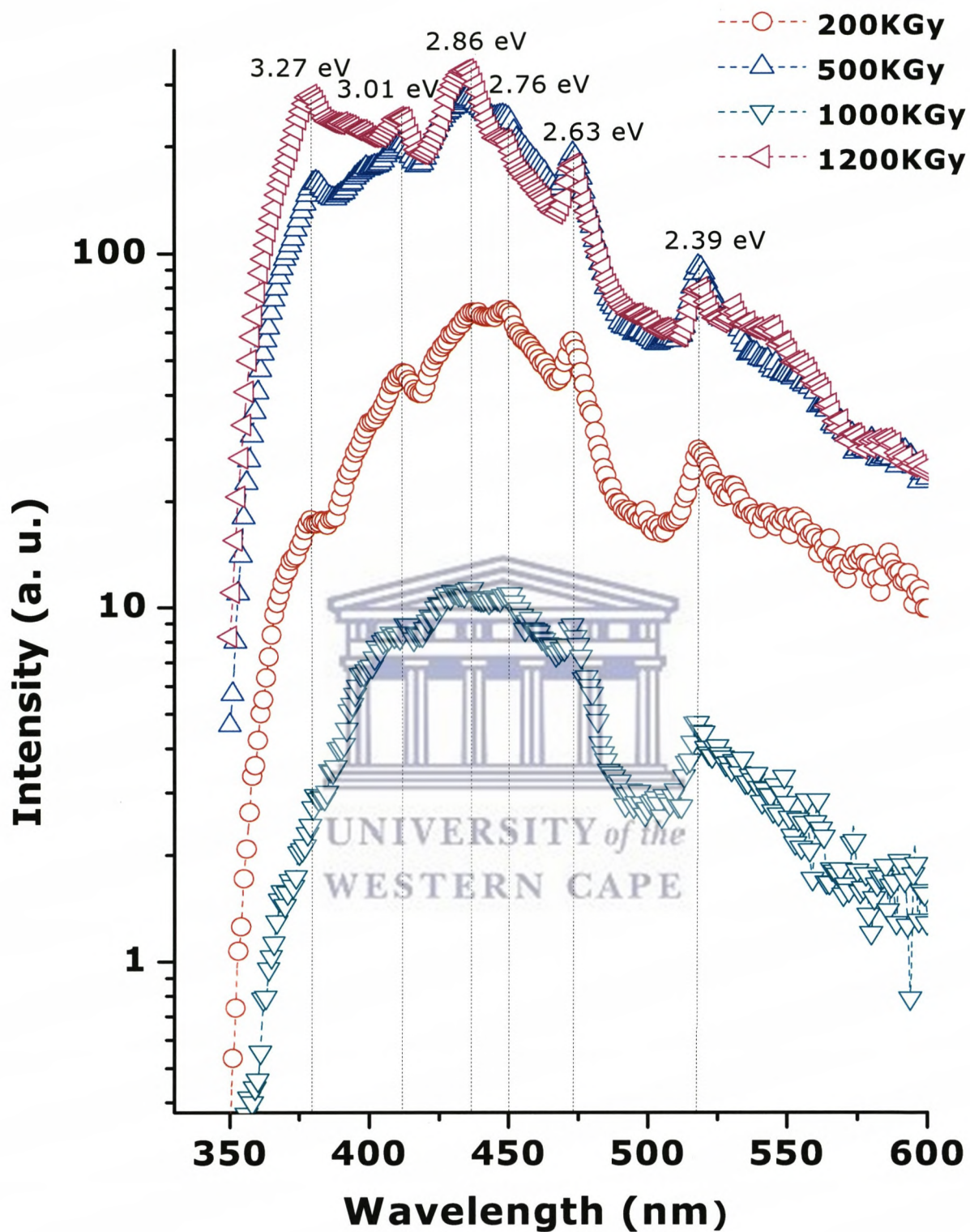


**Figure 6.4c:** Room temperature PL of  $\gamma$ -ray irradiated samples of 6H-SiC.

Hence, multiple radiative transitions are seen for the same impurity atoms with their corresponding phonon replica series.

As the material is irradiated, first, the irradiation may be causing a reduction in the concentration of undamaged sites, thereby altering the signal intensity relative to the noise signal. Another possibility may be that an increase in the probability of photon re-absorption has occurred due to an increase in absorbing defects. One or both of these processes could be taking place, causing the PL spectrum of irradiated SiC to be so complex.

In addition to the additional emissions bands into the visible region, figure 6.4c is limited to the spectral range of 320-600 nm since in the near infrared the spectra of the  $\gamma$ -ray irradiated samples are completely dropping down with a very large noise causing difficulty to identify the near infrared emissions bands.

Increasing the irradiation dose causes a nonlinear change in luminescence in the wavelength region of 350 – 450 nm that is as well seen in the near band edge region ( $\sim 400$  nm). Irradiation-dependent PL measurements of these peaks indicate the existence of two defects, each associated with the hexagonal and cubic equivalent lattice sites. A set of two peaks, 2.63 and 2.86 eV respectively become quenched in the growing green emission band luminescence. Such behavior suggests that shallow damage centers, introduced by the gamma rays irradiation, are beginning to anneal out of the material. The emission PL peak intensities emerge with a strong signal at 2.86 eV along with its associated phonon replicas. The signal is further enhanced as the  $\gamma$ -rays dose is increased to 1200 KGy.

The resultant emission spectrum is dependent on two probability factors. The first of these is the probability that a recombination event will result in a radiative transition (versus de-excitation through non-radiation recombination). The

second deals with the probability that the emitted photon is reabsorbed within the material, preventing it from being detected. This is especially true for the deeper trapping centers, resulting in a decrease in the signal intensity. The complexity of the measured spectrum response to the irradiation increases even more since the concentration of defect centers, in addition to the emission and capture probabilities, change as a function of irradiation dose, and those changes are not necessarily proportional to the change in  $\gamma$ -rays dose, or to one another.

A peak signal at 3.0 eV, which is not enhanced from the non-irradiated material, appears almost enhanced due to irradiation and subsequently grows with irradiation dose. The peak signal at 3.27 eV shows a similar trend as a function of increased irradiation dose. The peak (3.0 eV) represents the defect-exciton transition most likely at the hexagonal site while the peak (2.85 eV) represents the defect-exciton most likely transition at the cubic site.

Therefore we can resume that the near band edge characteristics of 6H-SiC are present in the optical spectrum of the non-irradiated material. The material is altered as a result of  $\gamma$ -rays irradiation and the luminescence of these shallow centers is attenuated almost entirely with the emergence of deeper shallow traps at energies greater than 350 meV below the bandgap. Subsequent increase in the emission spectrum at both the near band edge region ( $E_g \cong 3.27$  eV) and between ( $E_C - E_T$ ) = 2.65 and 2.85 eV.

In the deep trap region below 2.85 eV, activation of trap centers results in a sharp decrease in the signal intensity of an irradiation-induced defect trap (3.0 eV) as well as the associated phonon replicas. Based on previous ion-implantation studies in SiC conducted by Scott, the emergence of the 2.85 eV defect complex

and associated phonon replicas as a result of the  $\gamma$ -rays irradiation may be as a result of the resultant lattice damage.

### 6.3.2 Effect of Protons irradiation

#### 6.3.2.1 Raman Spectroscopy

Fig. 6.5a exhibit first-order Raman spectra (1RAMs) from 6H-SiC Protons irradiated at different doses. All the 1RAMs and folded modes (see Fig. 6.5a) are present. Several modes disappear with protons irradiations on spectra.

Some of the modes could be interpreted as overtones or three phonon processes. The mode at  $532\text{ cm}^{-1}$  which is almost overlapping with the mode at  $520\text{ cm}^{-1}$  could be an overtone of planar an E<sub>2</sub> ( $266\text{ cm}^{-1}$  peak 2) and the mode at  $520$  (peak 3) may be an overtone of the plane E. Some of them could be an instrument feature such as  $195$  and  $200\text{ cm}^{-1}$ .

The non irradiated SiC sample exhibit all Raman Si-Si , C-C active modes with very sharp A<sub>1</sub>(LO), E<sub>2</sub>(TA) and E<sub>2</sub>(TO) peaks confirming the 6H-SiC nature as reported in figure 6.5a. A new protons induced bands around  $2040$  occur on spectra at a dose of  $360\text{ }\mu\text{C}$ .

The intensity of all the Raman Optical & acoustical modes decreases with the H<sup>+</sup> Fluence including the second order Raman bands in the  $500$  and  $1400\text{-}1850\text{ cm}^{-1}$  implying a structural lattice damages of Si-Si, Si-C bonds as and the homonuclear C-C bonds. If one considers the intensity decay of A<sub>1</sub> (LO), E<sub>2</sub> (TA) and E<sub>2</sub> (TO) peaks mainly, the damage threshold is  $F_{\text{Threshold}}^{\text{H}^+} \sim 270\text{ }\mu\text{C}$  see figure 6.5b.



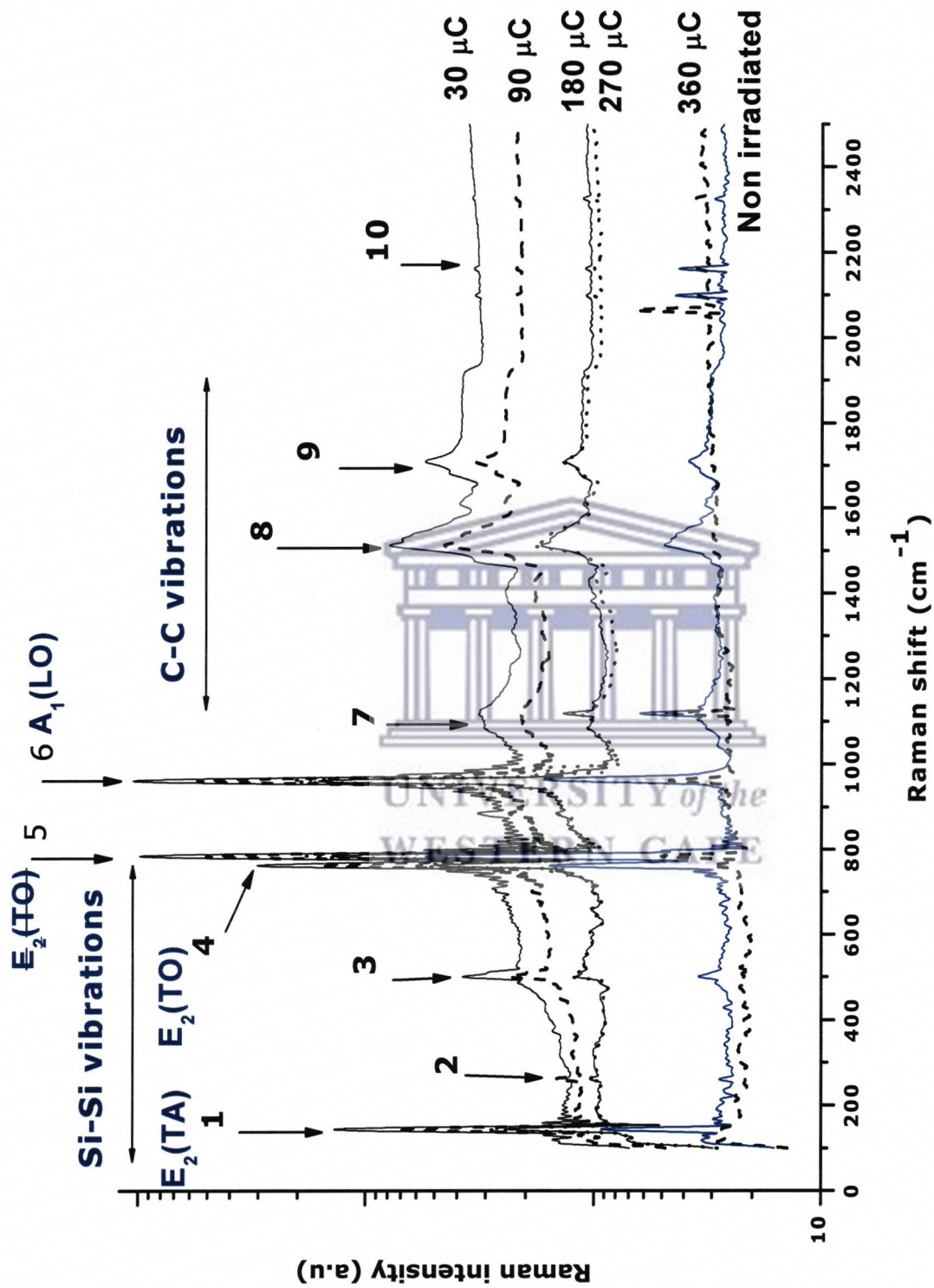


**Figure 6.5a:** Raman spectra from 100  $\text{cm}^{-1}$  to 2500  $\text{cm}^{-1}$  for protons irradiated and non irradiated samples of SiC.

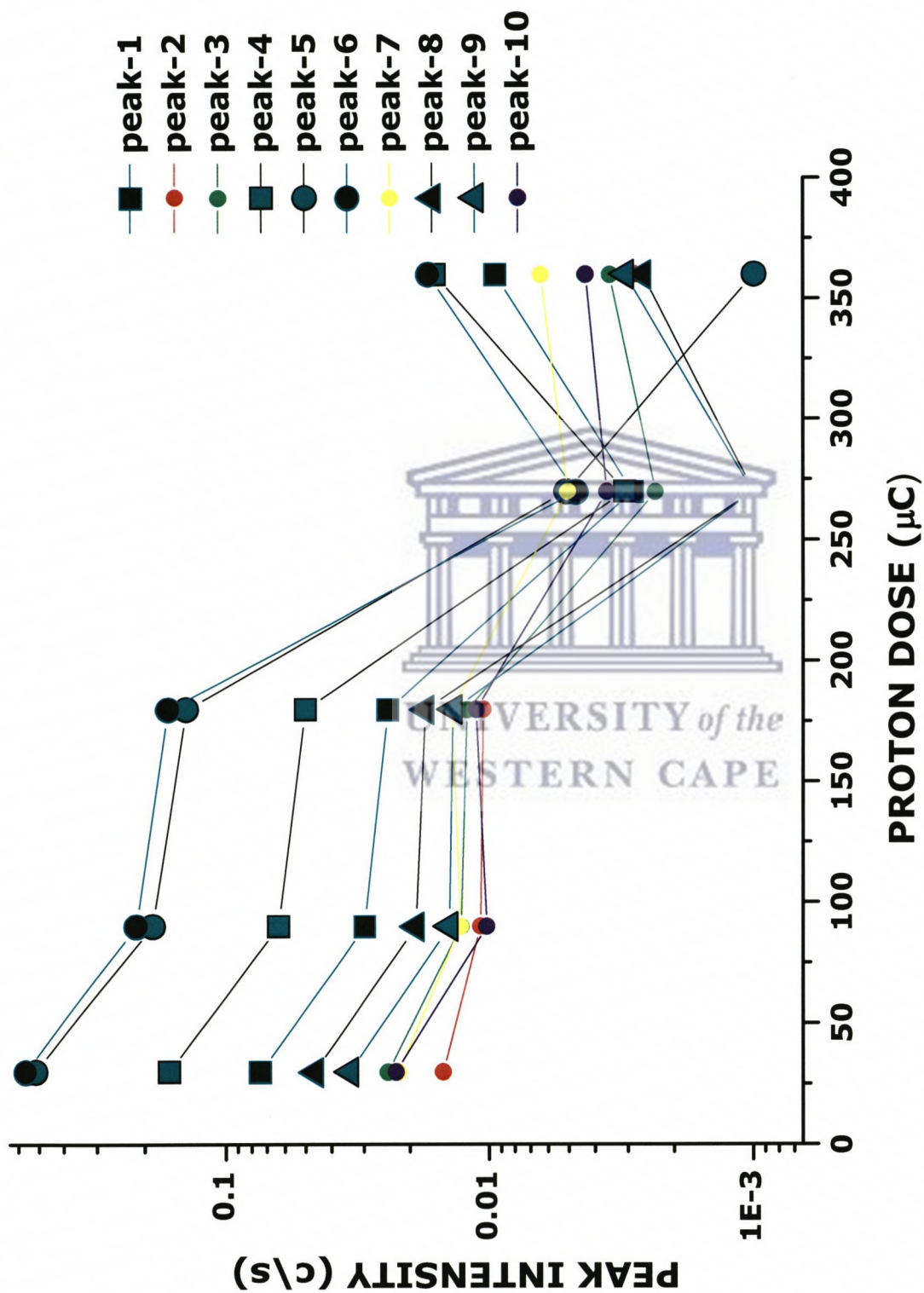


**Figure 6.5b:** The peak intensity evolution of the different observed mode versus protons irradiation dose.

### 6.3.2.2 Atomic Force Microscopy

The 3D images of the protons irradiated and non irradiated SiC samples are shown in figure 6.6a. The H<sup>+</sup> irradiation of the SiC samples induces a marked smoothing of the surface at the nano-scale level. Such a surface trend implies an induced amorphization at least of the surface and the sub-surface layer upon.

This behaviour can be understood in terms of the direct-impact model, where amorphization is described by the accumulation of individual amorphous tracks. At larger fluences, tracks begin to overlap, and the increase/decrease in amorphous/ crystalline fraction becomes sub-linear.

The root mean square  $\langle\sigma_{RMS}\rangle$  as shown in figure 6.6b, decreases with the H<sup>+</sup> Fluence  $F$  from  $\sim 13$  nm to  $\sim 2$  nm in an exponential type variation:

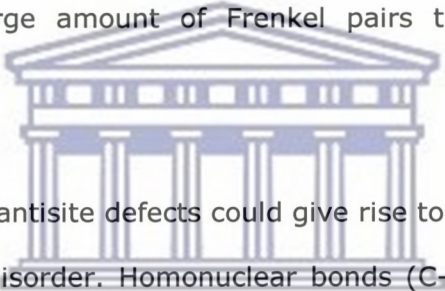
$$\sigma_{RMS} = 10.8 \exp(-F / 68.9) + 1.64$$

Actually, SiC exhibits different amorphization behavior in response to ion beam irradiation depending on the ion energy and ion mass. The irradiation with ions of medium mass (such as C, Si, etc) having energies of a few hundreds keV primarily produce interstitials, vacancies, antisite and small defect cluster [15]. The growth and coalescence of these point defects and small clusters correspond to partial or total amorphization. In contrast, heavy impinging ion (such as Au, etc) creates, within its displacement cascade, an amorphous zone surrounded by a defective crystalline region which in turn becomes amorphous after subsequent ion impacts, either directly by defect accumulation or indirectly by the growing of already existing amorphous zones.

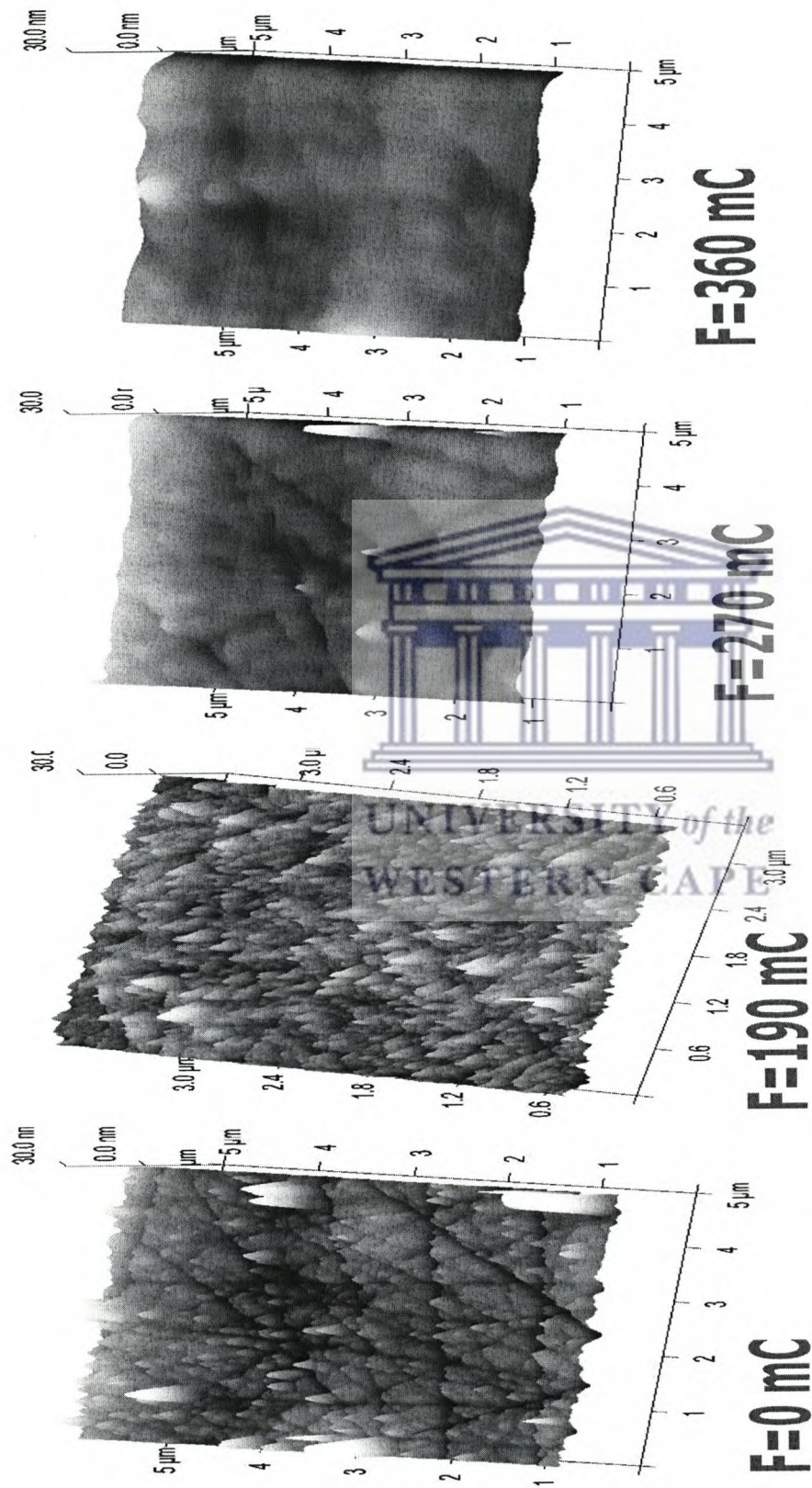
With regard to the characterization of the varying disordered microstructures of SiC, the mechanisms controlling the topological transformation have been of

particular interest. By simulating the accumulation of irradiation damages due to the low energy recoils, Malerba and Perlado [16] argued that both Frenkel pairs and antisite defects play significant roles in the amorphization process and that the coalescence and growth of defect clusters account for the amorphization of SiC.

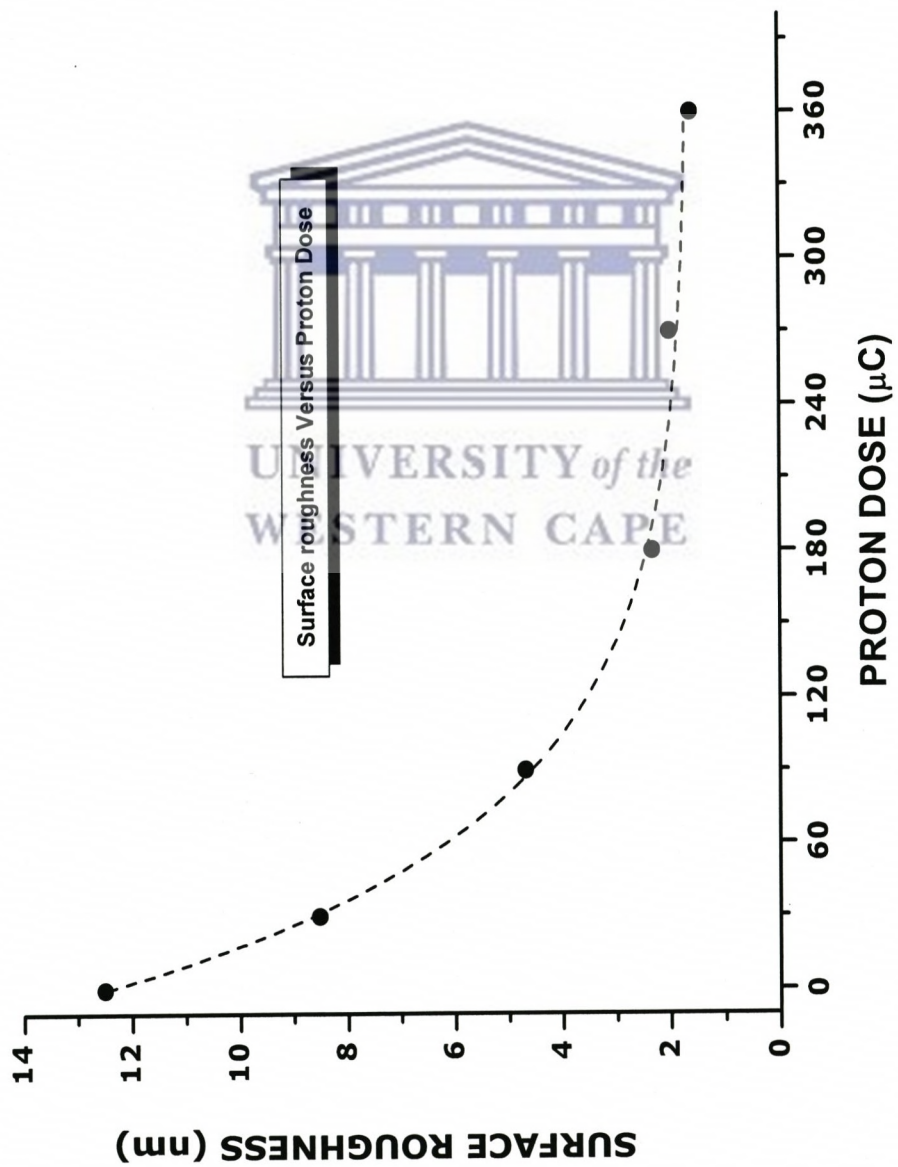
Antisite defects were found to be less numerous than Frenkel defects, whose accumulation has been instead primarily supposed to trigger amorphization. However Frenkel pairs have strong correlation with antisites. The MD simulation of the disordering and amorphization processes in SiC irradiated with ions reveals much higher concentration of antisites in complete amorphous areas where are supposed to comprise large amount of Frenkel pairs than other disordered domains [15].



Basically both Frenkel and antisite defects could give rise to dual disorder, namely topological and chemical disorder. Homonuclear bonds (C-C, Si-Si) are likely to form when antisite or Frenkel defects are introduced, producing a certain degree of chemical disorder. The homonuclear bond ratio ( $R_{hb}$ ), defined for SiC as the ratio of number of homonuclear bonds to twice the number of heteronuclear bonds, provides a full homonuclear bond analysis. Chemical disorder ( $\chi$ ) [17], defined as the ratio of C-C bonds to C-Si bonds, ( $N_{C-C}/N_{Si-C}$ ), is not a full homonuclear bond analysis and is specified only for C atoms.



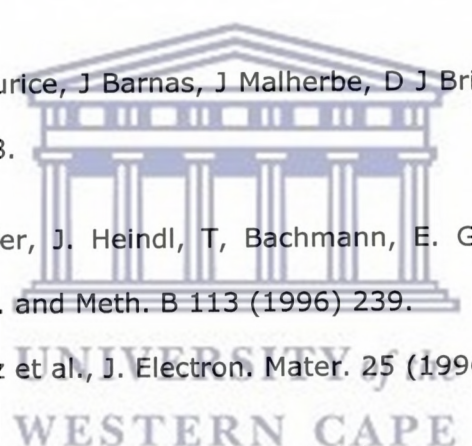
**Figure 6.6a:** AFM micrographs of non-irradiated and protons-irradiated 6H-SiC samples.



**Figure 6.6b:** AFM surface roughness as a function of protons dose.

Because Frenkel pairs and antisites have overlapping effects on the amorphization of SiC, and exclusively focusing on the formal Frenkel pairs and antisite configuration themselves has ignored the multiplier effects on the immediate coordination of a much larger number of atoms. The current experimental observation could just support the existence of C-C and Si-Si homonuclear bonds, rather than provide the accurate degree of chemical disorder as reported by the Raman spectroscopy results.

#### 6.4 References:

- 
- [1] L.L. Snead, S.J. Zinkle, J.C. Hay, M.C. Osborne., J. Nucl. Mater. 141 (2009) 123-132.
- [2] H W Kunert, T Maurice, J Barnas, J Malherbe, D J Brink, L Prinsloo, vacuum 78 (2005) 503-508.
- [3] A. Heft, E. Wendler, J. Heindl, T. Bachmann, E. Glaser, H.P. Struck, W. Wesch, Nucl. Instr. and Meth. B 113 (1996) 239.
- [4] A. Pérez-Rodríguez et al., J. Electron. Mater. 25 (1996) 541
- [5] P.F. Wang, L. Huang, W. Zhu, Y.F. Ruan, Solid State Communications Volume 152, Issue 10, May 2012, Pages 887-890
- [6] Nakashima S, Tahara K. Phys. Status. Solidi A 162(1997) 39
- [7] A. Prez-Rodroquez, Y. Pacaud, L. Calvo-Barrio, C. Serre, W. Skorupa, J.R. Morante, J. Electron. Mater. 25 (1996) 541
- [8] Khalil, A, Chadderton, L, Didyk, A et al 2008, 'Surface Modifications by Swift Heavy-Ion Irradiation of Indium Phosphide', Physics of Particles and Nuclei, vol. 5, no. 5, pp. 481-487.
- [9] Jiang W, Weber WJ, Thevuthasan S, McCready DE, Nucl. Instrum. Meth. B 143 (1998) 333-41
- [10] Sangsig Kim et al., Jpn. J. Appl. Phys. Vol 39 (2000) pp. 5875-5878
- [11] E Viswanathan et al., Nucl. Instr. Meth. B 269 (2011) 1103-1107

- [12] T.V. Torchynska, A. Di z Cano, S. Jimenez Sandoval, M. Dybic, S. Ostapenko, M. Mynbaeva, *Microelectronics Journal* 36 (2005) 536–538
- [13] F Nava, G Bertuccio, A Cavallini and E Vittone *Meas. Sci. Technol.* 19 (2008) 102001 (25pp)
- [14] Scott, M.B., "Electrical and Optical Characterization of Intrinsic and Ion-Implantation Induced Defects in 6H- and 4H-SiC", PhD Dissertation, AFIT/DS/ENP/99-04, Department of the Air Force, Air University, Air Force Institute of Technology. November (1999) AD-A371042.
- [15] F. Gao, W. J. Weber, and R. Devanathan, *Nucl. Instrum. Methods Phys. Res. B* 180, 177 (2001)
- [16] L. Malerba and J. M. Perlado, *J. Nucl. Mater.* 289, 57 (2001)
- [17] J Tersoff *Physical Review B* 49(23), 16349--16352, APS, 1994



UNIVERSITY *of the*  
WESTERN CAPE



## CHAPTER 7

### Summary and conclusion

---

Our primary objective has been to investigate the effects of various radiation types to 6H-SiC with a description of the beds and the importance of the stability of the SiC-C interface upon the effects of radiations ( $\gamma$ -rays, hot neutrons, protons). In this study we have investigated the effects of radiation induced damages to 6H-SiC, using various analytical techniques, namely: XRD, Raman Spectroscopy, AFM, and Photoluminescence.

Our XRD structural investigation, by monitoring the XRD patterns, showed a constant change in the d-spacing and such is related to the structural stress of the crystal lattice induced by the irradiation due to the presence of points defects. All samples were characterized, to search for the presence of C or Si clusterization in the samples after irradiation and by means of XRD for evaluating the presence of different SiC polytypes. The Raman peak at  $520\text{ cm}^{-1}$  in SiC which is due to the presence of c-Si clusterization was not seen, while the peaks at  $765\text{ cm}^{-1}$ ,  $785\text{ cm}^{-1}$  and  $965\text{ cm}^{-1}$  which are due to 6H-SiC were present. Therefore no Silicon or carbon clusterization was detected in the samples after irradiation and also the XRD analysis reveals no presence of others SiC polytypes but just stress which is confirmed by the Raman analysis.

The samples irradiated with gamma rays, Raman intensity decreased with increasing irradiation dose, indicating the increase in defects of  $\gamma$ -ray-irradiation induced lattice damage, disarranging silicon-carbon bonds, the evolution of the profile of Raman scattering spectrum was comparable to that observed for the

un-irradiated 6H-SiC, indicating that the  $\gamma$ -rays induced lattice defects evolved into dilute stable defects.

In the SiC samples irradiated with protons, the intensity of all the Raman Optical & acoustical modes decreases with the  $H^+$  Fluence including the second order Raman bands in the 500 and 1400-1850  $cm^{-1}$  implying a structural lattice damages of Si-Si, Si-C bonds as and the homonuclear C-C bonds. The AFM shows that the  $H^+$  irradiation of the SiC samples induces a marked smoothing of the surface at the nano-scale level. Such a surface trend implies an induced amorphization at least of the surface and the sub-surface layer upon.

In conclusion, in all cases of neutron, protons and gamma rays irradiated, 6H-SiC revealed the presence of defects. With the techniques used, we were unable to determine the nature of the defects and this study will be conducted further to determine their nature. The properties of radiation defects in SiC are shown that at room temperature the type is almost independent of the type of ionizing radiation (protons, gamma rays and neutrons). In addition irradiation mainly brings about an increase in the concentration of deep-level centres that already exist in the material and the above-mentioned increase is more remarkable with gamma rays and most of all with neutron irradiation.